universität wien

DISSERTATION / DOCTORAL THESIS

Titel der Dissertation /Title of the Doctoral Thesis

„Bulk Nanocrystalline Soft Magnetic Fe-Si-X Alloys Achieved Through Severe Plastic Deformation“

verfasst von / submitted by

Sheraz Khakwani

angestrebter akademischer Grad / in partial fulfilment of the requirements for the degree of

Doktor der Naturwissenschaften (Dr. rer. nat)

Wien, 2019 / Vienna, 2019

Studienkennzahl lt. Studienblatt / degree programme code as it appears on the student record sheet:	A 796 605 411
Dissertationsgebiet lt. Studienblatt / field of study as it appears on the student record sheet:	Physik
Betreut von / Supervisor:	Ao.Univ.Prof.Dr.i.R. Michael Zehetbauer

Abstract

The magnetic properties of soft magnetic materials such as Fe-Si-X alloys can be strongly improved by nanocrystallization, if the grain size is smaller than the magnetic moment exchange length. So far only small-scaled nanocrystalline samples could be produced by bottom-up techniques which strongly restricted the application cases of soft magnetic materials. However, recent top-down techniques known as those of Severe Plastic Deformation (SPD) allow for the production of bulk nanocrystalline soft magnetic materials. These methods achieve very large strains under elevated hydrostatic pressure thus keeping the full materials' density. With pressures of up to 10 GPa, the method of High-Pressure Torsion (HPT) reaches grain and/or subgrain sizes well below 100-10 nm, thus arriving below the size of magnetic domains, i.e., the exchange length of magnetic moments. This leads to a significant decrease of coercive force (H_c) and finally of the hysteresis losses (P/f with f as the frequency) being an inherent goal of soft magnetic materials research. However, since HPT is a method of plastic deformation, internal stresses including high densities of dislocations are generated which themselves increase H_c. It was a main goal of this thesis to find a way to remove those defects without increasing the grain and/or subgrain size. A second goal was to show whether subgrains with low misorientation can play a similar role as highly misoriented grains with regard to the magnetic moment exchange length.

Samples from cast and powder Fe, Fe-3wt%Si and Fe-6.5wt%Si materials were HPT-processed at RT and liquid N2 temperature, and then characterized by their nanostructures, as well as by the magnetic properties such as coercivity (H_c), permeability (μ), and the magnetic losses (P/f), with f being the frequency. Comparing investigations have been done after a gentle heat treatment at 200 ^{o}C of the HPT processed samples for the sake of decreasing H_c by removing the internal stresses and/or the dislocations. The main method used for structural characterization was the X-ray Line Profile Analysis which was capable of measuring the subgrain (=crystallite) size (D), the dislocation density (N), as well as the dislocation arrangement α. Although the hysteresis loops of all materials were measured in the frequency range from 5 Hz to 200 Hz at room temperature on ring-shaped samples, this thesis focused on the understanding of the

static magnetic properties. Changes of H_c and P/f were found to be in parallel but not with those of permeability (μ); they could be related to the changes of most important parameters such as the subgrain size (D), the dislocation density (N), and the change of dislocation arrangement α: only decreases of D or N and/or α led to decreases of H_c. Since continued HPT-processing can only achieve decreases of D and concomitant increases of N and/or α, thermal treatments were applied after HPT-processing, in order to decrease N (or at least α) while keeping D unchanged. It turned out that a maximum decrease of H_c could only be reached when a strong increase of D, N or α during HPT-processing or during thermal treatment could be avoided. Other conditions are that the HPT-induced strain applied is not too large and the processing temperature is not too low; otherwise nanostructures become resistant to the thermal treatment. When D increased at constant N or α, then also H_c increased which confirms that H_c is dominated by exchange coupling within the magnetic domains, their size exceeding that of the subgrains. Herzer's theory which predicts a change of the $H_c \sim D^6$ law for large-angle misoriented grains, to a law with distinctly lower exponent $H_c \sim D^n$ with $n \leq 3$ in the case of small-angle misoriented subgrains, was confirmed by the experiments of this thesis.

Motivated by recent literature, an alternative path to reach nanocrystalline structures was attempted, too, by applying HPT to originally amorphous materials out of the same elements like the crystalline samples, e.g. commercial Fe-Si-B, and by thermally treating the samples like in the case of crystalline samples. However, it was not possible to achieve crack-free samples by means of HPT so that for this processing path more experiments are necessary in the future.

Kurzfassung

Die magnetischen Eigenschaften weichmagnetischer Materialien wie die Fe-Si-X Legierungen können durch Nanokristallisation stark verbessert werden, wenn die Korngröße kleiner ist als die Länge der Austauschwechselwirkung der magnetischen Momente. Bisher konnten bei nanokristallinen Materialien nur relativ kleine Proben realisiert werden mittels bottom-up Techniken, was die Anwendungen für weichmagnetische Materialien stark einschränkte. Jedoch sind neue top-down Techniken - bekannt als die der "Starken Plastischen Verformung" (Severe Plastic Deformation, SPD), - in der Lage, massive nanokristalline weichmagnetische Materialien herzustellen. Diese Methoden erlauben die Realisierung von sehr hohe plastische Verformungen bei gleichbleibender Materialdichte, indem der hydrostatische Druck während der Verformung erhöht wird. Wenn dabei Drucke bis zu 10 GPa angewandt werden können, kann man mit der Methode der "Hochdrucktorsion" (High-Pressure Torsion, HPT) Korn- bzw. Subkorngrößen von deutlich kleiner als 100-10 nm erreichen und somit die typische Größe der magnetischen Domänen, dh. die Länge der Austauschwechselwirkung der magnetischen Momente unterschreiten. Damit werden auch die Koerzitivkraft (H_c) und schliesslich die Hystereseverluste (P/f, f ist die Frequenz) signifikant reduziert, was ein inhärentes Ziel der Forschung zur Verbesserung weichmagnetischer Werkstoffe darstellt. Jedoch werden bei HPT wie bei allen Methoden der plastischen Verformung innere Spannungen und hohe Dichten von Versetzungen generiert, welche ihrerseits H_c erhöhen. Es war ein Hauptziel der vorliegenden Doktorarbeit, einen Weg zu finden, diese Defekte zu entfernen, ohne dabei die Korn/Subkorngröße zu verändern. Ein zweites Hauptziel bestand darin zu zeigen, ob die Subkörner mit kleiner Missorientierung eine ähnliche Rolle wie die Körner mit großer Missorientierung spielen können in Bezug auf die Austauschlänge der magnetischen Momente.

Massive und pulverförmige Materialien Fe, Fe-3wt%Si and Fe-6.5wt%Si wurden bei RT und Flüssig-Stickstoff-Temperatur HPT-prozessiert, sowie hinsichtlich ihrer Nanostruktur als auch ihrer magnetischen Eigenschaften wie Koerzivität (H_c), Permeabilität (μ) und magnetische Verluste (P/f mit f als Frequenz) charakterisiert. Vergleichende Untersuchungen wurden an zusätzlich bei 200°C getemperten Proben durchgeführt, um

eine Abnahme von H_c durch Reduktion der inneren Spannungen bzw. der Versetzungsdichte zu erreichen. Die zur strukturellen Charakterisierung wichtigste angewandte Methode war die Röntgen-Linienprofil-Analyse (XLPA), welche nicht nur die Subkorn- (=Kristallit-)größe (D), sondern auch die Versetzungsdichte (N) sowie das Versetzungsarrangement (α) erfassen. Obwohl die magnetischen Hysteresen aller untersuchten Materialien im Frequenzbereich 5-200 bei RT an ringförmigen Proben gemessen wurden, befaßte sich die vorliegende Dissertation vorwiegend mit den statischen magnetischen Eigenschaften. H_c und P/f zeigten eine parallele Charakteristik, was aber nicht für die Permeabilität (μ) gilt. Die Änderungen können weitgehend auf die wichtigsten Parameter Subkorngröße (D) und Versetzungsdichte (N) bzw. Versetzungsarrangement (α) zurückgeführt werden: nur Abnahmen von D oder N bzw. α führten jeweils zu Abnahmen von H_c. Weil die HPT-Prozessierung prinzipiell Abnahmen von D, aber Zunahmen von N und α zur Folge hat, wurden nach der HPT-Prozessierung Wärmebehandlungen angewandt, um N zu verringern ohne dabei D zu ändern. Dabei zeigte es sich, dass eine maximale Reduzierung von H_c nur möglich war, wenn eine starke Zunahme von D, N oder α während der HPT-Prozessierung vermieden werden konnte. Eine andere Voraussetzung dafür ist, dass die HPT-induzierte plastische Verformung nicht zu groß und die Verformungstemperatur nicht zu gering ist, andernfalls die entstehenden Nanostrukturen resistent gegen die thermische Behandlung werden. Wenn D zunahm bei konstantem N oder α, nahm auch H_c zu, was bestätigt, dass H_c von der Austauschkopplung innerhalb der magnetischen Domänen dominiert wird, indem deren Größe die Subkorngröße D übersteigt. Herzers Theorie, welche eine Änderung des $H_c \sim D^n$ mit $n \leq 3$ voraussagt im Fall von wenig mißorientierten Subkörnern, wurde von den Experimenten dieser Arbeit bestätigt.

Motiviert durch die neueste Literatur wurde in dieser Arbeit auch eine alternative Route zur Realisierung von nanokristallinen Strukturen versucht, indem HPT auf amorphe Materialien mit den gleichen Bestandteilen wie die kristallinen Proben, wie z.B. kommerzielles Fe-Si-B, angewandt wurde inkl. anschliessender thermischer Behandlung. Jedoch war es nicht möglich, rißfreie Proben trotz Anwendung von HPT zu realisieren, was für die Zukunft zahlreiche weitere Experimente erforderlich macht.

Acknowledgments

I would like to express my deepest gratitude to Professor Michael Zehetbauer for giving me the opportunity to join his research group (Physics of Nanostructured Materials) and work with him. I am grateful for his guidance and support, both work-related and otherwise, throughout my stay. Extensive discussions with him on the project were a great source of knowledge for me.

I am also deeply grateful to Professor Roland Groessinger† (TU Wien) for his guidance, inspiration and support until the very end. He was a thorough gentleman, a soft-spoken, kind person and a dedicated researcher.

I would like to thank Professor Erhard Schafler for his help with HPT and XRD equipment. I would like to thank Monika Antoni (Erich Schmid Institute of Materials Science, Austrian Academy of Sciences, Leoben) and Alexander Rabensteiner (TU Wien) for their help with the magnetic measurements. My gratitude also goes to Dr. Michael Kerber and Dr. Daria Setman for their help with the HPT equipment. General thanks are also due to the whole workshop staff of the Faculty of Physics, University of Vienna, Austria for their cooperation.

Finally, I would like to thank my parents for supporting my studies, and lots of love and appreciation are for my wife and my children for their patience.

Table of Contents

Chapter 1: Introduction & Aims of Thesis

Magnetically speaking Iron is the most important element in the entire periodic table. Iron and its alloys have always held a special place in the magnetic and electronics world. Iron alloys show the widest range of magnetic materials in existence; from Nd-Fe-B (very hard magnetic material) to $Fe_{73.5}Cu_1Nb3Si_{13.5}B_7$ (very soft magnetic material) and everything in between. Silicon steel (Fe3wt%Si) or electrical steel has been the workhorse of the electrical industry for about a century and is still widely used. A combination of low cost and good magnetic properties still makes it a very attractive material for general use. For special uses amorphous VITROPERM ($Fe_{73.5}Cu_1Nb3Si_{13.5}B_7$) is heat treated in a controlled manner to grow a nanocrystalline phase within the amorphous matrix. The gives a very low coercivity along with very low losses at some loss of saturation flux density.

In recent years the research in the field of nanostructured materials processed by severe plastic deformation (SPD) has gained momentum because of their distinct physical and functional properties. An exceptional grain refinement and a high density of defects obtained through SPD can impart great strength to the metals and alloys which is generally not present in their coarse-grained counterparts. SPD processing can alter the stability of the phases and can create metastable phases which possess very unique properties. Grain size below 100 nm which is easily achievable through SPD techniques can have a profound effect on the magnetic properties. For example, magnetic properties of pure iron are improved when due to high density of defects the resistivity of iron increases which reduces the eddy current losses. At grain sizes below about 50 nm exchange interaction is a possibility which strongly improves the soft magnetic properties of the materials.

This research starts with a wide range of Fe-Si-based alloys, both amorphous and crystalline, to be processed through an SPD technique, namely High-Pressure Torsion (HPT), to study the effect on magnetic properties of these materials. These materials include pure iron, Fe-3wt%Si (bulk and powder), Fe-6.5wt%Si (bulk and powder),

amorphous VITROPERM foils and nanocrystalline VITROPERM foils. For iron, Fe-3wt%Si and Fe-6.5wt%Si the goal is to reduce the grain size to a point where exchange interaction becomes operative. For VITROPERM materials the aim is to achieve the best possible HPT-processed samples from thin foils of VITROPERM that will be magnetically tested later in future by another researcher.

SPD-processing induces a high density of defects that are detrimental to the soft magnetic properties of the materials as they restrict the movement of magnetic domain walls. So another aim of this research is to reduce these stresses and HPT-induced defects without increasing the grain size in order to improve the magnetic properties. Differential Scanning Calorimetry (DSC) is used to determine appropriate temperatures for these heat treatments. The effects of these heat treatments are characterized through nanoindentation hardness testing, X-ray line profile (XLPA) analysis, optical and transmission electron microscopy of selected samples. Finally, the Fe-Si samples are magnetically tested with a hysteresisgraph to determine whether HPT processing and heat treatments have any effect on the magnetic properties of the materials under study.

Chapter 2: Literature Survey/State of the Art

2.1 Severe Plastic Deformation

Severe plastic deformation (SPD) is a general term describing a group of metal-working techniques achieving large strains under extended hydrostatic pressure, resulting in a nanocrystalline structure (grain sizes d < 100 nm) and a very high density of dislocation density of lattice defects [1-7]. As it is a top-down method, it can achieve bulk nanocrystalline materials while keeping 100% density.

Severe plastic deformation has become a well-recognized and widely used technique for the fabrication of ultrafine grained (UFG) materials to attain unique mechanical, electrical, magnetic and other physical properties. The techniques that come under the umbrella of SPD are capable of producing nanocrystalline (< 100 nm) structures and in some cases even down to amorphous structure [4, 8]. Conversely it is also possible to grow nanocrystals within the amorphous structure [9-11], also by means of SPD.

There are many techniques that come under the umbrella of Severe Plastic Deformation (SPD). Some of these techniques are distinct while others are only variations or combinations of these techniques. Reference [6] lists about nineteen of these techniques. The most important of these techniques comprise of Equal-channel angular processing (ECAP) [12], High-pressure torsion (HPT) [13], Accumulative roll binding (ARB) [7], Multi-axial forging [7], Twist extrusion [14], Repeated corrugation & straightening (RCS) [7], Con-shearing [7], High-energy ball milling [15].

The biggest advantage of these techniques is that an ultra-fine grained or nanocrystalline structure can be achieved in almost all materials. This is not possible with most of the conventional techniques especially with brittle materials: this is mainly because of the absence of the extended hydrostatic pressure which is the most important feature of SPD, as it keeps the sample from cracking. It is well known that nanostructured materials offer several benefits over their coarse-grained counterparts. Using SPD techniques it becomes easier to transform various materials into nanostructured materials and get the

benefits afforded by nanocrystalline materials with ease of processing. Some of the advantages and shortcomings of the SPD are discussed below:

- Superplasticity is the ability to achieve very high elongations (400% - 1000%) before failure. Using SPD techniques it is possible to induce superplasticity in various materials [16]. Superplasticity needs a grain size of the order of a few microns at high deformation temperatures and low strain rates. The lower the temperature and/or higher the strain rates, however, the smaller must be the grain size to still achieve superplasticity [17]. As SPD techniques can produce very small grain sizes therefore they are ideal methods to induce superplasticity in many different kind of materials, e.g., [18] lists many Al, Mg, Fe, Ti and Ni-based alloys as well as several ceramics such as Alumina and Zirconia that exhibit superplasticity and can benefit from SPD techniques.
- Nanocrystalline metals have been known to exhibit improved fatigue resistance [19].
- SPD makes it possible for brittle materials (e.g., WO_3, B_2O_3 glasses etc.) to be processed without failure [6].
- It is well-known that nanocrystalline imparts superior strength to the materials owing to the Hall-Petch relation. SPD techniques have the ability to impart strength even beyond the Hall-Petch relation [20-26].
- In some cases, SPD processes induce brittleness in materials [7].
- Typically there is a size limitation on the material that can be processed using SPD techniques.
- SPD processed materials may have poor thermal stability. For example, SPD-processed very pure copper starts to recover immediately even at room temperature [6].

2.1.1 Mechanisms operative during Severe Plastic Deformation

There are five stages of plastic deformation which are distinguished by the work hardening parameter $\Theta = d\tau/d\gamma$ where τ is the shear stress and γ is the shear strain. Strain values till $\gamma \approx 1 - 2$ corresponds to stages II and III of work hardening. Constant work

hardening decreases in the stage III, remains constant or increases a bit in stage IV, and finally starts to decrease and becomes equal to zero in stage V. From stage IV to stage V, a decrease in sub(grain) size occurs, while the misorientation between the neighboring grains increases [1, 27].

Like in standard plastic deformation, during SPD processing some mechanical energy is introduced into the solid. After the elastic dissipation of energy, the plastic flow is the next dissipation channel for the deformative energy. As the deformation progresses new channels of energy dissipation become active. These are dynamic recrystallization, phase transformations and the thermal energy. Mechanical fracture, both at local level and at the macro level, is another energy dissipative route. However, the benefit of SPD techniques, especially HPT, is that the solid is forced to deform without fracture at the macro level. In pure metals low-temperature dynamic recrystallization occurs after the fragmentation. This dynamic recrystallization suppresses the defects and plastic flow starts again in the new grains. Eventually an equilibrium is established and further fragmentation is prevented. In case of solid solutions or intermetallic compounds the mobility of plastic deformation carriers is low. In this case phase transition acts as an energy dissipative channel. This phase transition could be from one crystal structure to another or from crystalline to the amorphous state [28].

TEM investigations show that like in traditional plastic deformation, a low-angle cell structure is formed at the initial stage of the SPD process in pure metals which then transforms into a mixture of cell and grain structures in the intermediate stage. A uniform equiaxed grain structure of about 100-200 nm is formed in the final stage of SPD (at least at $T = 0.25\ T_m$, for details see 2.12). During this development the structure changes from the one with low-angle grain boundaries to the one with high-angle grain boundaries [29].

Final grain size depends upon the processing temperature, the strain imposed on the material and the addition of alloying elements. The steady-state size of the structural elements increases markedly with increasing processing temperature. In many materials, an equivalent strain between 10-50 results in a saturation in the grain size refinement. Finally, alloying elements have a profound effect on the grain size refinement. Usually for

pure metals the approximate grain size is between 200 – 150 nm while with alloying additions the grain size can be reduced to between 70 – 30 nm [30].

2.1.2 High-Pressure Torsion

High-pressure torsion (HPT) represents a processing technique in which material is subjected to large torsional straining under high hydrostatic pressure, typically between 1 to 10 GPa [4, 8, 13]. The large hydrostatic pressure prevents the material from cracking thus providing grain refinement until grain size reduces to a nanometer range and, in some cases, even to amorphous state [4, 8]. The final grain size depends on the material that is being processed. For pure metals the mean grain size resulting from HPT processing at room temperature is around 100 - 200 nm while for alloys and intermetallics it is generally in the range of 50 – 100 nm [20, 31-33].

HPT is a top-down approach which means it starts with a bulk solid with a coarse grain size and reduce it down to a sub-micron or nanometer range. This has the advantage of eliminating porosity and contamination [8]. A schematic diagram of a typical HPT setup is shown in Fig. 2.1. In this case one anvil (usually upper) is fixed (immovable) while the other anvil rotates at a fixed speed. The sample material is placed in between the two anvils. While the anvil rotates the material is under a tremendous pressure – anywhere from 1 GPa to 10 GPa.

There are three ways [8, 34] in which an HPT experiment can be actualized depending upon the method of preparation of the anvils used during the process:

(i) Unconstrained HPT (Fig. 2.1a)

(ii) Fully constrained HPT (Fig. 2.1b)

(iii) Quasi-constrained or semi-constrained HPT (Fig. 2.1c)

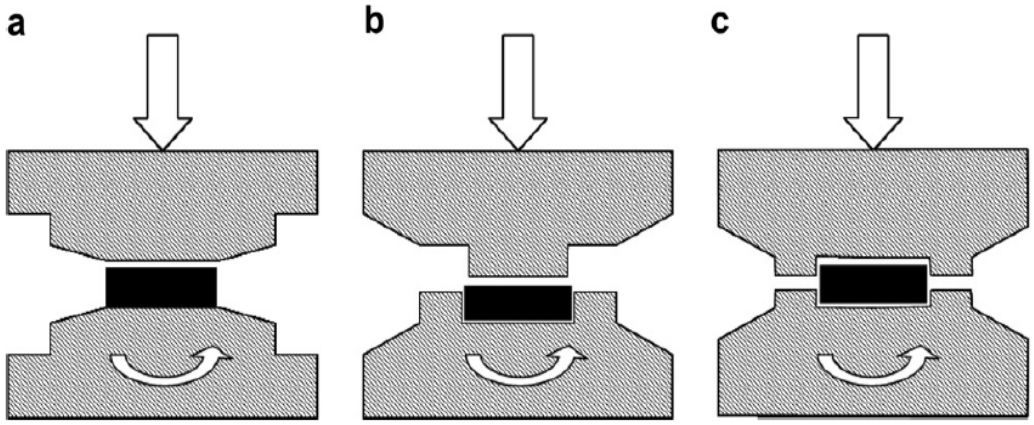

Figure 2.1: Schematic illustration of High-Pressure Torsion experiment (a) Unconstrained HPT (b) Fully constrained HPT (c) Semi-constrained HPT [8].

In unconstrained HPT the material is placed on the lower anvil and the pressure is applied along with the torsional straining. There is some back pressure because of the frictional force between the sample and the anvils. Due to this little back pressure the grain refinement is usually limited.

In fully constrained HPT there is a cavity machined into the lower anvil in which the material is placed. The upper anvil is machined such that it fits the cavity of the lower anvil perfectly. Ideally there should be no outflow of the material during processing. This variation of HPT, however, is almost never used because of difficulty of making perfectly fitting anvils. Also, after the experiment it is difficult to get the material out of the cavity without damaging it.

Quasi-constrained or semi-constrained HPT is the most used variation of this technique. In this method both anvils have cavities of identical dimensions machined into them. Some material flows out of the cavities during processing that creates a significant back pressure on the rest of the material. This results in a substantial grain refinement of the material under processing.

Extremely large strains can be achieved using HPT [35] which are usually not possible with other methods. Relatively brittle or high-strength materials can be processed at low temperature. Processing can be done at different temperatures – from liquid nitrogen to about 700 ^{o}C. HPT can also result in superplasticity in the processed material [17]

Using HPT it is also possible to induce phase transformation through pressure [35-41]. For example, Edalati found that after HPT under 4 GPa pure zirconium showed an α to ω transformation [41].

The formulae for the shear strain ($\gamma = 2\pi Nr/h$ or $\gamma = 4\pi Nr/3h$ for ring-shaped samples) indicate that the value of shear strain changes with the radius of the disk. This means that there will be an inherent inhomogeneity in grain refinement from the center of the disk to the edge. In reality, after a certain number of rotations the sample achieves more or less complete homogeneity. Zhilyaev [8] indicated that in pure Ni for a pressure of 6 GPa and a torsional straining through more than five turns at room temperature, the sample achieved complete homogeneity, because of having reached the deformation stage V in all areas of the sample. In any case the central region (~ r = 0) is much less or not refined as much as the outer regions (as is also indicated by the formula for shear strain given at the beginning of this paragraph) [42]. These variations in homogeneity are assessed through microhardness testing or through SEM/TEM.

HPT-processed samples are always in the form of a disk (or a ring in special cases). The sample size is usually small – of the order of 10 mm. currently it is possible to make a sample as large as 100 mm. However it requires a large and powerful HPT equipment (i.e., a press with approx. 10,000 N capacity). The sample thickness is usually around 1 mm. It can vary a bit but if the sample is too thick then it creates an inhomogeneity across the depth of the sample.

HPT, in conjunction with other techniques, has been used to create amorphous phase in crystalline materials. This is usually easier in complex alloys. However, in general, a very small portion of the sample is converted to amorphous state. Conversely, if an amorphous material is processed through HPT it is possible to induce nanocrystallization in the amorphous phase [8, 43-45].

Edalati [46] performed HPT on many pure elements and found that the steady-state grain size decreases by atomic bond energy and related parameters such as specific heat capacity, activation energy for self-diffusion and homologous temperature. Stacking fault energy was not found to be a dominant factor in these cases. The steady-state level is found to be a characteristic of each metal and is mostly the same irrespective of the initial

state of the metal before processing and the processing parameters such as pressure, provided no phase transformation occurs. For pure elements the grain refinement is controlled by the type of atomic bonds (metallic or covalent) as well as the atomic bond energy ΔH.

Edalati [47] measured the temperature of the sample during the HPT deformation for many metals and found that temperature increases in the disc samples during HPT. The temperature increases at the early stages of straining but saturates to steady state at large strains. The increase in temperature is higher for harder materials, for higher pressure and for higher rotation speed. The temperature increases from the center towards the edge of the sample.

Scheriau [36] processed 316L stainless steel through HPT within temperatures T_{def} -196 ^{o}C and 720 ^{o}C temperatures and found that different processing temperatures activated different deformation mechanisms:

At T_{def} > 450 ^{o}C the dominant deformation mechanism is diffusion glide.

450 ^{o}C > T_{def} > 20 ^{o}C mechanical twinning is observed.

20 ^{o}C > T_{def} > -196 ^{o}C mechanical twinning is replaced by the deformation induced martensitic transformation ($\gamma_{fcc} \rightarrow \varepsilon_{hcp}$).

The stacking fault energy (SFE) of the material under processing has a significant effect on the final grain size achievable after HPT. In materials with lower SFE it becomes difficult for the dislocations to recombine and cross-slip which impedes the recovery process resulting in a lower value for minimum diameter. A lower SFE also results in a higher density of twins in the material. These twins are necessary for grain refinement in most materials that are processed through HPT [8, 48]. Edalati, on the other hand, found that steady-state grain sizes are generally independent of SFE in pure metals [46].

HPT, in conjunction with other techniques, has been used to create amorphous phase in crystalline materials. This is usually easier in complex alloys. However, in general, only a very small portion of the sample is converted to amorphous phase. Conversely, if an amorphous material is processed through HPT it is possible to induce nanocrystallization in the amorphous phase [8, 43-45].

Depending upon the composition of the amorphous materials, during HPT, small deformation-induced crystallites are produced in the material. If the material is then annealed at a low temperature, these small crystallites act as nuclei and result in nanocrystallization of the material [8]. This is an important benefit of HPT because these deformation-induced crystallites can induce a very uniform nanocrystallization with a controlled size at a lower annealing temperature. Straumal found that SPD/HPT-treatment at room temperature is frequently equivalent to the heat treatment at higher temperatures. This means that sometimes we see the same phases after HPT-processing at room temperature that we see after a heat treatment at a much higher temperature [49].

Sundeev [43] tried to find out whether amorphization through melt-quenching is the same as that obtained from SPD/HPT. It was concluded that the abilities to thermally-induced and deformation-induced amorphization differs entirely. For example, $Ti_{50}Ni_{25}Cu_{25}$ alloy has a low ability to amorphize upon melt-quenching but a high ability to amorphize under SPD. This behavior is opposite in case of $Zr_{50}Ni_{18}Ti_{17}Cu_{15}$. Thermally-induced amorphization is determined by high temperature parameters (ductility, diffusion mobility and thermodynamic stability of the crystalline phase) while deformation-induced amorphization depends on low-temperature physical parameters that affect the mechanical, thermodynamic and concentration factors of the crystalline to amorphous state transition.

HPT machines can usually be operated in both directions. This has important impact on the microstructure and mechanical properties of the material under processing. Glezer processed commercially pure iron in HPT and found that reversing the direction of torsion stimulates dynamic recrystallization and considerably reduces the level of internal stresses. Hardness and mechanical durability is reduced with this cyclic deformation [28].

Dynamic recrystallization occurs at room temperature during HPT which leads to the formation of ultra-fine grains with high angle of misorientation. Edalati found that the temperature rise during HPT is of minor importance in initiating this dynamic recrystallization. The formation of high-angle grain boundaries through dynamic recrystallization is due to the presence of large volumes of lattice defects [50]. The initiation of high-angle grain boundaries in the deformed structure is associated with low-

temperature dynamic recrystallization and not just the deformation fragmentation process [51].

2.2 Magnetism

"Magnetism is the phenomenon by which materials exert an attractive or repulsive force on other materials"[52].

In general, all materials are affected by magnetism in one way or another. Iron, some steels, cobalt and nickel are famous ferromagnets while superconductors are perfect diamagnets.

2.2.1 Ferromagnetism

Iron (Fe), Nickel (Ni) and Cobalt (Co) are well-known ferromagnets that exhibit a permanent magnetization at room temperature (and above) even when the external magnetic field ceases to exist. Other elements like Gadolinium (Gd), Terbium (Tb), Dysprosium (Dy), and Ruthenium (Ru) are ferromagnetic below the room temperature. Apart from the many compounds of iron, nickel and cobalt there are compounds of non-ferromagnetic elements that show ferromagnetism such as Fe_2O_3, MnSb, CrO_2 etc. All ferromagnetic materials become paramagnetic above Curie temperature (T_c) and their susceptibilities follow Curie law or Curie-Weiss law after that.

These ferromagnetic materials have an internal molecular field that is very strong (~ 10^8 A/m) and it can magnetize the material to its saturation even without the help of an external field. However this means that all ferromagnetic materials should exist only in magnetized state. This is in fact rarely seen. Weiss tackled this problem by introducing the concept of magnetic domains. The material is divided into several small regions called domains. Each domain is completely saturated to its maximum value M_s but overall the orientation of magnetization of these domains is such that the material has no net magnetization. This is illustrated in Fig. 2.2. The boundary between two dissimilar domains is called a domain wall. The domain walls can be Bloch walls or Néel walls or

mixed. Different energies competing with one another contribute to the formation of these walls and determine their sizes. These energies include magnetoelastic energy, anisotropy energy, magnetostatic energy etc. When an external field is applied then the magnetic moments that are at a favorable angle to the direction of applied magnetic field start to align themselves with the field. This favorable domain grows at the expense of unfavorable domain and eventually the unfavorable domain disappears. When every single magnetic moment is aligned in the material the material is said to be magnetically saturated. The strength of the external field at which this saturation M_s is achieved is a structure-sensitive property, however, the magnitude of M_s is a material property. True theoretical magnetic saturation (in which all spins are parallel) can only be achieved at 0K. At T > 0K the thermal agitation forces some spins to be antiparallel. Ferromagnetism in transition metals is almost entirely due to electronic spin with almost no contribution from the orbital motion of the electrons. In ferromagnets the valence electrons that part in magnetism have the ability to exert a special quantum-mechanical force on to other electrons in order to align their spins in parallel. This phenomenon is called the Exchange Interaction and it is represented by exchange integral J_{ex}. Exchange interaction will be briefly discussed in Section 2.5.

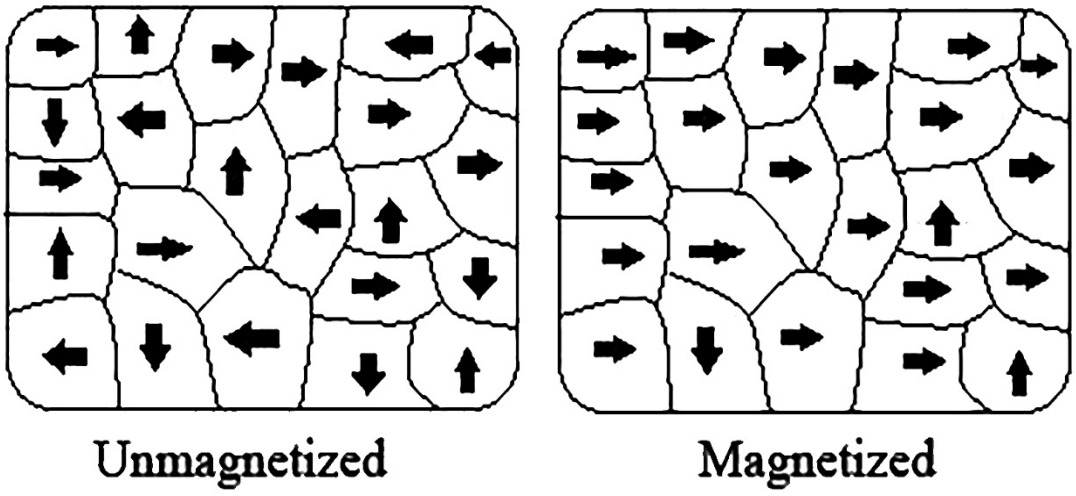

Figure 2.2: Magnetic domains in unmagnetized and magnetized states.
(http://science4fun.info/magnetism/)

Fig. 2.3 shows a generalized hysteresis curve typical for a ferromagnetic material. The hysteresis curve is the most important tool to characterize any magnetic material showing the quantities such as the coercivity, remanence, and magnetic saturation.

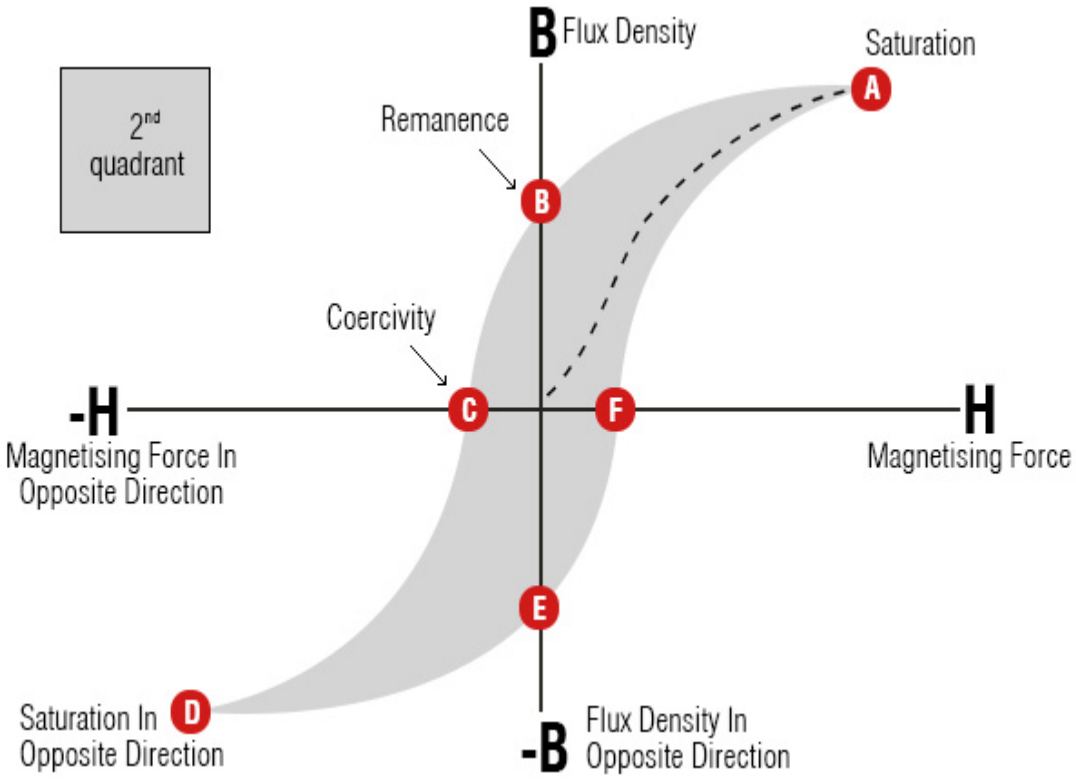

Figure 2.3: Generalized hysteresis graph of a ferromagnetic material showing important magnetic quantities such as coercivity, remanence, and magnetic saturation. The shaded area of the hysteresis curve represents the total losses. (http://www.first4magnets.com/assets/images/techCENTRE/TechCentre_Hysteresis-Loop-Diagram.jpg)

2.2.2 Hard Magnetic Materials

From a practical application point of view, magnetic materials are divided into two groups, namely hard magnetic materials (permanent magnets) and soft magnetic materials. This classification is made on the basis of coercivity values that these materials possess. Hysteresis curves of both type of materials are shown in Fig.2.4.

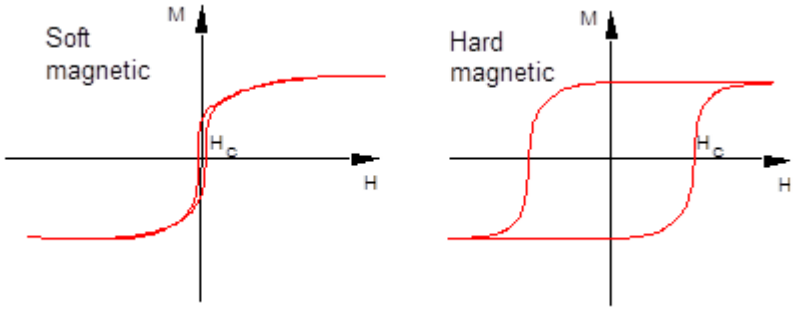

Figure 2.4: Comparison of the hysteresis loops of a soft and a hard magnetic material.

Materials with a high coercivity value (H_c > 10 kA/m) are called hard magnetic materials. A strong external magnetic field is required to magnetize these materials from their demagnetized state. Once these materials are magnetized they retain their magnetization even after the external magnetic field is removed. This property of the hard magnetic materials is called Remanence or Residual Magnetism. These magnets can generate strong static field up to about 1T. Examples of such materials are Fe-C steels, Alnico (alloy of Al, Ni and Co), and intermetallics like Sm-Co and Nd-Fe-B. Permanent magnets with large coercivity and large remanence are used in loudspeakers, small motors, generators and sensors, while permanent magnets with medium coercivity and medium remanence are used to make video and audio tapes, hard disks and floppy disks etc.

2.2.3 Soft Magnetic Materials

Those magnetic materials which have coercivity less than 1 kA/m are considered as magnetically soft, that is, these can be easily magnetized and demagnetized. Those hysteresis curves show the magnetization M as a function of magnetic field H, with the coercivity H_c as the characteristic section in H, the permeability dB/dH with B as the magnetic field or magnetic induction, as well as the losses per frequency represented by the area under the hysteresis curve. Permeability is the property of magnetic materials that describe the ease with which a magnetic material can be magnetized. The magnetizing and demagnetizing processes exhibit a strong frequency dependence [53, 54]. A good soft magnetic material is characterized by low coercivity, low losses, high

induction, high magnetic flux and high permeability. Soft magnetic materials are mainly used in magnetic cores of transformers, generators, motors, inductors, stress/strain gauges, and in field sensors etc. Most of the electrical and electronics systems such as computers, recording systems, grid systems etc. also use soft magnets. The hysteresis loop of soft magnetic materials depends on the microstructure. Particularly when the grain size becomes comparable to the exchange length, exchange coupling occurs which results in a drastic reduction of the coercivity [55]. Examples of soft magnetic materials are Fe-Si alloys, Fe-Ni alloys (Permalloy), Fe-Al alloys (Sendust), Fe-Co alloys, soft ferrites (ceramic materials) and amorphous materials (e.g., FINEMET/VITROPERM, NANOPERM etc.).

2.3 Magnetic Properties of Nanostructured Materials

Magnetic nanomaterials with grain sizes below 100 nm are shown to exhibit enhanced magnetic properties provided the exchange length between the magnetic moments becomes larger than the average grain size of the material. This mechanism is displayed by nanocrystalline FINEMET (VITROPERM) where the average grain size is between 10 – 20 nm. This FINEMET material is produced through melt quenching to an amorphous state and then heat treated to produce a nanosized Fe3Si phase within the amorphous matrix. Vorhauer et. al. [56] reproduced the same effect with Fe-17Co steel (P800) by reducing the size from 300 nm to 30 nm using the HPT technique. This effect is shown in Fig. 2.5 [5].

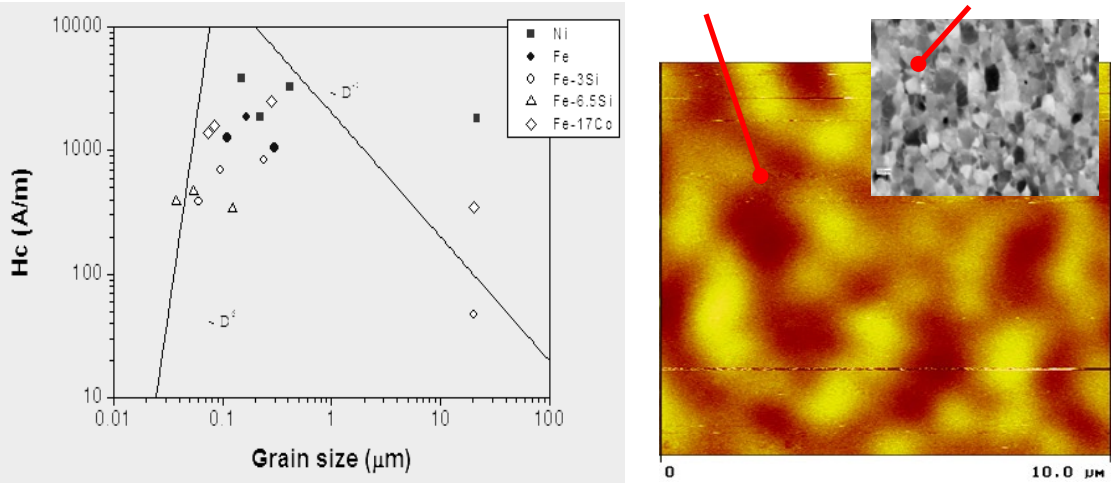

Figure 2.5: Left side: coercivity H_c as a function of grain size, in HPT-processed materials as indicated. When H_c decreases with smaller grain size, exchange coupling is suspected to occur. Right side: Magnetic force microscopy image from HPT-processed steel P800 showing about 1µm large magnetic domains distinctly exceeding the grain size being much below 100 nm in average (see black-white inset), indicating exchange coupling (from [5]). The length of image base line represents 10 µm.

Leslie-Pelecky et. al. [57] presents an excellent review of the magnetic properties of nanostructured materials. It classifies the magnetic nanostructures into four classes where type A systems consist of isolated particles with no interaction between the individual particles (e.g., ferrofluids), while type D systems are those where up to 50% volume of the sample is composed of grain boundaries and interfaces and there is a strong interaction between the particles. Types B & C are in between those of A and D, with varying degrees of strength of interaction.

Changes in magnetization of these materials occur through activation over the energy barrier that is present between the neighboring particles. These energy barriers have associated lengths, e.g., crystalline anisotropy length L_k, the applied field length L_H, and the magnetostatic length L_s. Equations for these lengths are given below:

$$L_k = \sqrt{J/K} \qquad \text{Eq. 2.1}$$

$$L_H = \sqrt{2J/HM_s} \qquad \text{Eq. 2.2}$$

$$L_s = \sqrt{J/2\pi M_s^2} \qquad \text{Eq. 2.3}$$

where:

J is the exchange within a grain

K is the anisotropy constant of the bulk material due to the dominant anisotropy

M_s is the saturation magnetization

H is the magnetic field strength

This reference [57] summarizes the Holz and Scherer theory for nanostructure materials. This theory describes the behavior of type D nanostructure materials. It assumes that the crystallographic correlations within the nanocrystals are of the order of nanocrystallite size d. If $L_k >> d >> L_s$ then crystalline anisotropy reduces to a point where it has no effect on the magnetic properties. The magnetic properties are then mainly dominated by the magnetostatic and exchange energies. If the ratio L_k/L_s is large then this theory provides good agreement with the experimental results.

2.4 Exchange Interaction

Exchange interaction is a quantum-mechanical effect that takes place between identical particles (such as electron-electron). This effect has no analogy in the classical mechanics. Exchange interaction projects itself as a force but it is not a true force because it lacks a force carrier (“Exchange Interaction”, Wikipedia, n.d).

Quantum-mechanical particles can either be bosons (integer spin) or fermions (spin-half). Many bosons can occupy the same quantum state but no two fermions can occupy the same quantum state according to Pauli’s exclusion principle. Since electrons are fermions therefore when two electrons come closer (and their electron cloud overlap) the overall wavefunction must be antisymmetric to comply with the Pauli’s exclusion principle.

In magnetism only outermost electrons are relevant, inner shell electrons do not participate in magnetism. Consider two atoms with one proton and one electron on each atom. When these atoms are far away, their respective electrons are localized. However, when the two atoms come closer to each other then the wavefunctions of the electrons interact and exert certain influence on each other. By Heitler-London approximation the

orbital wave function of two electrons can be approximated by a linear combination of the atomic orbital wavefunctions of two electrons localized on the two atoms. The solution of the total energy equation without considering the spins of the electrons is then given by:

$$\boldsymbol{E} = \boldsymbol{E_a} + \boldsymbol{E_b} + \left(\frac{\mathbf{1}}{\mathbf{1} \pm \boldsymbol{\alpha^2}}\right)(\boldsymbol{Q} \pm \boldsymbol{J}) \qquad \text{Eq. 2.4}$$

where:

E = Total energy of the system

E_a = Energy of electron a when it belongs to atom a

E_b = Energy of electron b when it belongs to atom b

$1/(1\pm\alpha^2)$ = Normalizing constant

Q = Coulomb electrostatic energy

J = Energy that arises from exchange of the electrons

When spins are considered then we get Heisenberg exchange Hamiltonian:

$$\mathbf{H_{ex}} = -\sum_{i<j} \mathbf{2}\boldsymbol{J_{ij}}\, \mathbf{S}_i . \mathbf{S}_j \qquad \text{Eq. 2.5}$$

where the summation extends over all nearest-neighbor spins (since spins beyond nearest-neighbors are hardly affected).

If J_{ij} is positive, then the exchange energy favors electrons with parallel spins and gives rise to ferromagnetism. If J_{ij} is negative, then the exchange energy favors electrons with antiparallel spins and gives rise to antiferromagnetism. The strength of exchange interaction was estimated to be 10^9 A/m or around B = 10^3 T [58]. Exchange interaction is particularly strong in 3d metals because the 3d-electron charge cloud is comparatively large. In the rare-earth metals the 4f electrons are highly localized so that there is no significant overlap and therefore no direct exchange mechanism of Heisenberg type can occur. However, exchange through intermediary atoms, called Superexchange, can occur.

2.5 Energies and Anisotropies in Magnetic Materials

As mentioned earlier domains are regions in ferromagnetic materials where the magnetic dipole moments are parallel in alignment. Wherever this alignment changes a domain wall is formed. In a demagnetized ferromagnetic material these domains are aligned in such a way that the vector sum of all the domains is equal to zero. If exchange interaction was the only phenomenon in play then all the moments would be spontaneously aligned in parallel. The domain structure that evolves in a ferromagnetic material is due to the interplay of various energy contributions and anisotropies in the present. These energies and anisotropies are briefly discussed below:

Magnetostatic Energy

If a ferromagnetic material is made up of a single domain, it acts as a block magnet. The potential energy generated by the magnetic material when it is placed in a magnetic field (or even its own internal magnetic field if it is a strong magnetic) creates a demagnetizing field around the block. This field opposes the external (or internal) magnetic field according to the Lenz's law. Associated with this demagnetizing field is a magnetostatic energy that depends on the shape of the sample. In order to minimize the total magnetic energy of the magnetic body the magnetostatic energy must be minimized. This can be achieved by reducing the demagnetizing energy by dividing the magnetic body into several domains. This is illustrated in Fig. 2.6. Adding extra domains reduces the magnetostatic energy but simultaneously it increases the exchange energy which is minimum when all the moments are aligned parallel. However, magnetostatic energy is a more dominant effect here than the exchange interaction. Magnetostatic energy gives rise to shape anisotropy in the material.

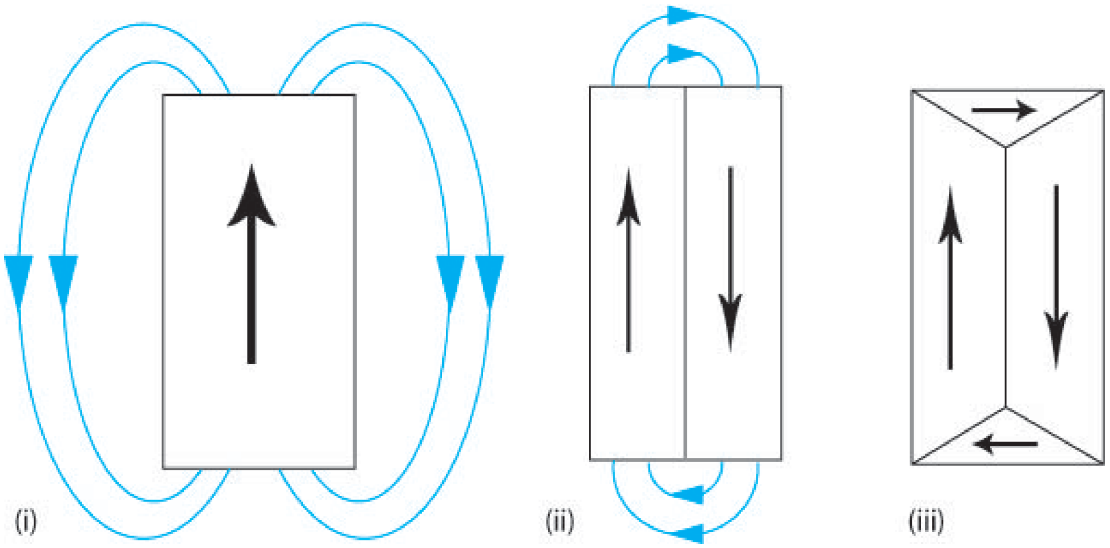

Figure 2.6: Schematic showing the demagnetizing field and the effect of domain formation on the electrostatic energy.
(https://www.doitpoms.ac.uk/tlplib/ferromagnetic/domains.php)

Magnetocrystalline Energy

When magnetic moments are inside an atomic structure lattice then they are influenced by the lattice. The dominant mechanism that gives rise to magnetocrystalline anisotropy is the spin-orbit coupling. This coupling ties electronic orbitals to the electronic spins and due to this, electronic orbitals follow the spins when the magnetization changes orientation in space. In short, the electronic orbitals are coupled to the lattice on one hand and to the spins on the other hand. In a ferromagnetic material this coupling results in certain crystallographic directions where it is easier for the magnetization vector to point (known as easy axis); and there are other crystallographic directions where it is hard for the magnetization vector to point (known as hard axis). There is an energy difference associated with magnetization along the two axis which is given by the difference in areas under the M-H curves as shown in Fig. 2.7. This energy is known as the magnetocrystalline energy. This energy is minimized if the domains formed have their magnetization vectors point along the easy crystallographic directions. In the domain walls there must be a change in the direction of magnetization and therefore, it cannot be aligned along easy axes. Therefore large domains with fewer domain walls would minimize the magnetocrystalline energy. As magnetocrystalline energy is direction-dependent therefore it gives rise to magnetocrystalline anisotropy. According to Livingston [59]

crystal anisotropy is the most effective way to impede magnetization reversal by rotation processes. Crystalline anisotropy provides an energy barrier that restricts the departure from the easy direction of magnetization. Thus increasing crystalline anisotropy would benefit hard magnetic materials while reducing it would benefit soft magnetic materials.

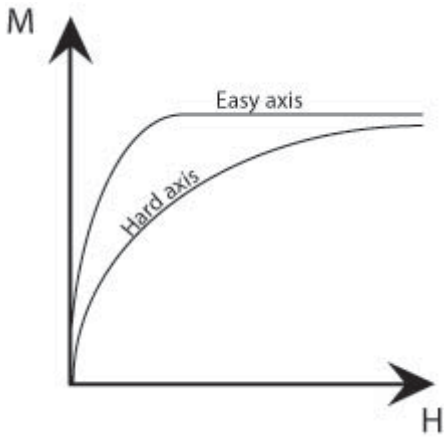

Figure 2.7: The effect of easy and hard magnetic axes on the magnetocrystalline energy. (https://www.doitpoms.ac.uk/tlplib/ferromagnetic/domains.php)

Magnetostrictive Energy

When a ferromagnetic material is magnetized it changes its shape. This is called magnetostriction. Magnetostriction can be positive or negative. If the length increases along the direction of magnetization then this is positive magnetostriction (e.g. in Fe), and if the length decreases then this is negative magnetostriction (e.g. in Ni). These length changes are of the order of parts per million. The change in length forces the horizontal domains of closure to elongate horizontally and the vertical domains of closure to elongate vertically. Both of these elongations cannot occur simultaneously and therefore the elastic strain energy in the material increases. The elastic strain energy is proportional to the volume of the domains of closure and therefore magnetostrictive energy can be reduced by decreasing the size of these domains. This in turn necessitate the reduction in size of primary domains which, consequently, increases their number. This results in new domain walls and an increase in magnetocrystalline and exchange energy of the system. In materials with large magnetostriction this becomes an important parameter. Magnetostrictive energy gives rise to stress anisotropy in the material.

2.6 The Random Anisotropy Model

The Random Anisotropy Model was originally developed by Alben et. al. [60] for amorphous magnetic materials based on the earlier model by [61]. Herzer [62-64] then further extended this model to include nanocrystalline materials. Amorphous FINEMET was heat treated between 500 ^{o}C and 900 ^{o}C which produced a grain size range from 10 nm to 300 nm. It was found that with increasing grain size D, from 10 nm to 50 nm, coercivity followed a D^6-power law. Coercivity then decreases for grain sizes above 150 nm following the 1/D-law for polycrystalline materials [63]. This is shown in Fig. 2.8.

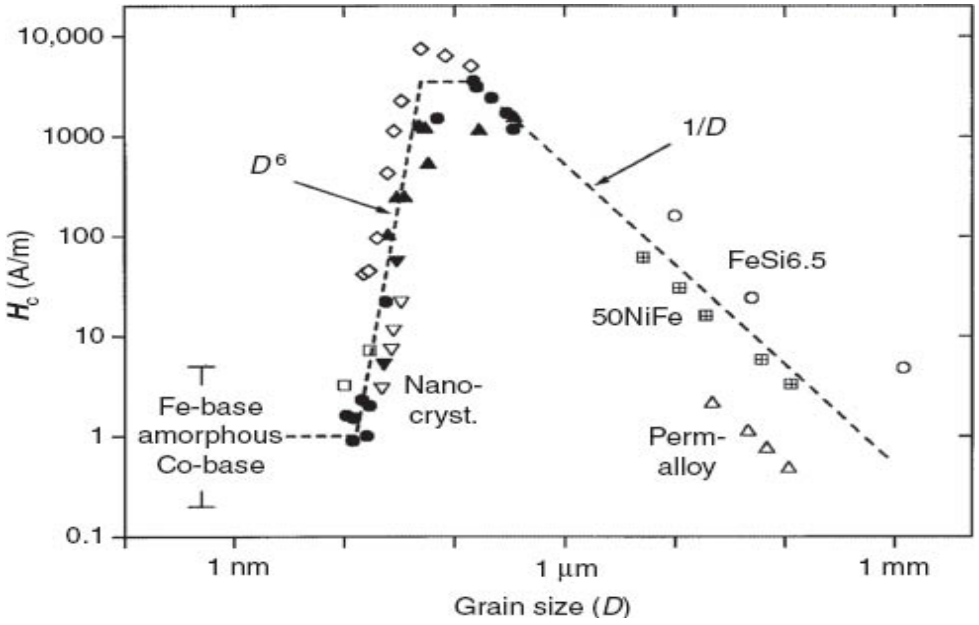

Figure 2.8 : Coercivity H_c vs. grain size D for various soft magnetic metallic alloys [55].

The magnetic properties of the ferromagnetic materials are related to their crystal structure in that the magnetization tries to follow the easy axis of the crystal structure. As discussed above this effect is incorporated in the magnetocrystalline anisotropy energy. The microstructure leads to a distribution of magnetic easy axis where magnetic moments vary their direction over the scale of the structural correlation length. This structural correlation length is given by the grain size D of the material. In polycrystalline materials with large grain sizes, the magnetization follows the individual easy magnetic directions of the structural units. In this case the magnetization is governed by the local magnetocrystalline anisotropy constant K_1 of the grains.

However, when the grain size falls below a certain value, it equals (or gets smaller than) the length of ferromagnetic exchange interaction. This causes a struggle between the exchange energy and the magnetocrystalline anisotropy energy. As a result the effective anisotropy for the magnetic behavior will be an average over several grains and therefore be reduced in magnitude. The critical scale where the exchange energy starts to balance the magnetocrystalline anisotropy energy is given by the ferromagnetic exchange length:

$$\boldsymbol{L_{ex} = \sqrt{A}/K_1} \qquad \text{Eq. 2.6}$$

where:

A is the exchange stiffness

K_1 is the magnetocrystalline anisotropy

L_{ex} is a measure of the minimum length scale over which the direction of the magnetic moments can vary significantly [65]. For Fe-20at%Si this value is calculated to be about 35 nm [63]. Below this value it is expected this alloy will show a sharp decrease in coercivity value and a corresponding increase in permeability value.

For a material with finite dimensions and N number of grains, there will always be some grains that are aligned favorably to the easy axis of magnetism. The resulting anisotropy density <K> is then the mean fluctuation amplitude of the anisotropy energy of the N grains:

$$< K > \approx \frac{K_1}{\sqrt{N}} = K_1(\frac{D}{L_{ex}})^{3/2} \qquad \text{Eq. 2.7}$$

Combining Eq. 2.6and 2.7 gives:

$$< K > \approx \left(\frac{K_1^4}{A^3}\right).D^6 \qquad \text{Eq. 2.8}$$

Eq. 2.8 is valid as long as the grain size D is smaller than the exchange length.

$$H_c = p_c \,.\, K_1^4 \,.\, D^6/(J_s.A^3) \qquad \text{Eq. 2.9}$$

$$\mu_i = p_\mu.J_s.A^3/(\mu_o.K_1^4.D^6) \qquad \text{Eq. 2.10}$$

where:

p_c and p_μ are dimensionless pre-factors (fitting parameters) close to unity

J_s is saturation polarization.

Eq. 2.9 and 2.10 show that coercivity H_c and permeability μ very strongly depend on the grain size D (as long as the grain size is not too large with respect to the exchange length; otherwise 1/D law applies). This is represented by the left-hand branch of Fig. 2.8. The grain size dependence gives a powerful tool to manipulate soft magnetic properties of a ferromagnetic material. If by using SPD techniques the grain size of conventional magnetic materials can be reduced to the order of few tens of micron then a massive improvement in magnetic properties such as coercivity and permeability can be achieved.

Apart from D^6-dependence a D^3-dependence of H_c was found by Suzuki et. al. [66, 67] for some nanocrystalline alloys with uniaxial anisotropies larger than the random magnetocrystalline anisotropy $\langle K_1 \rangle$. Their research shows that H_c of Fe-Zr-B-(Cu) and Fe-P-C-Ge-Si-Cu alloys follow a D^3 power law, while FINEMET-type compositions follow the D^6 power law as shown in Fig. 2.9.

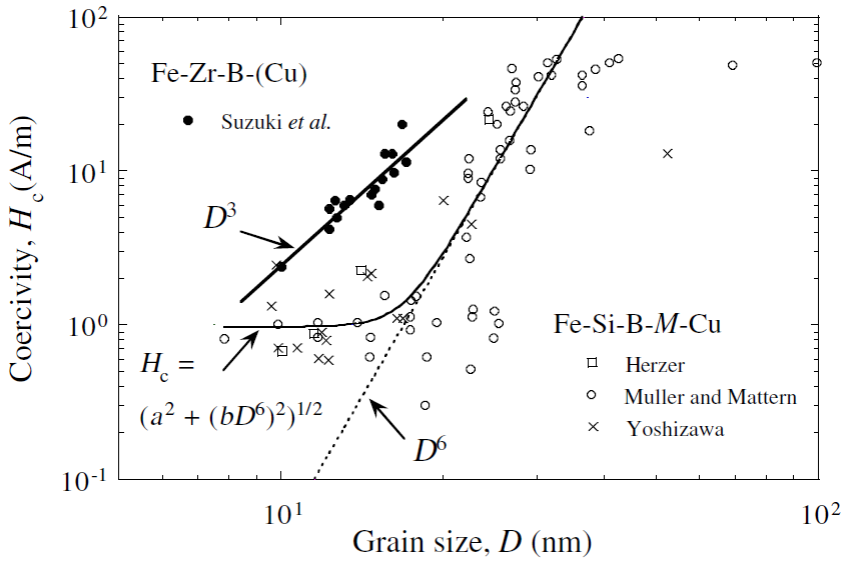

Figure 2.9: Coercivity H_c vs. grain size D for Fe-Si-B-M-Cu alloys (showing D^6 dependence) and Fe-Zr-B-(Cu) alloys (showing D^3 dependence).

As the grain size decreases, the effect of <K1> decreases; however, $\langle K_1 \rangle$ remains a factor. At lower grain sizes (< 20 nm) coherent field-induced anisotropy or long-range uniaxial

anisotropy (K_u) starts to become a major factor in determining the exchange length Lex. If $K_u >> <K_1>$ then:

$$< \boldsymbol{K} > \approx \boldsymbol{K_u} + \frac{\boldsymbol{1}}{\boldsymbol{2}}\sqrt{\boldsymbol{K_u}}\,\boldsymbol{K_1^2 D^3 / A^{3/2}} \qquad \text{Eq. 2.11}$$

This relation gives the D^3-dependence of total average anisotropy which in turn determines the exchange length L_{ex}:

$$\boldsymbol{L_{ex}} = \frac{\sqrt{\boldsymbol{A}}}{\sqrt{< \boldsymbol{K} >}} \qquad \text{Eq. 2.12}$$

Suzuki et. al. [67] found that the D-dependence changes from D^6 to D^3 when ratio of K_1 to K_u is approximately 1 to 2. The D^3 dependence is present, e.g., in bcc-Fe-based alloys where $K_u \approx 100$ J/m^3 but absent in DO_3-Fe(Si)-based alloys where $K_u \approx 10$ J/m^3. At small grain sizes where the random anisotropies are mostly suppressed, the soft magnetic properties are governed by uniaxial anisotropies K_u which are uniform on a scale much larger than the exchange length. In alloys where K_u is a major factor (such as Fe-Zr-B-(Cu) or bcc-Fe-based alloys that show D^3 dependence) the soft magnetic properties can be improved by suppressing K_u. Since K_u results from directional atomic ordering directed by the spontaneous magnetization, it can be suppressed by changing the magnetization direction continually during annealing [67]. This can be achieved by annealing the alloy in a rotating magnetic field.

2.7 Magnetic Losses and Frequency Dependence of Losses

The losses in the magnetic materials are a direct result of irreversible energies utilized during the magnetization and demagnetization processes during hysteresis measurements. These losses are much more important in soft magnetic materials compared to hard magnetic materials because soft magnetic materials work under a frequency-dependent environment. The total loss is given by the area of the hysteresis curve. Total core losses in a soft magnetic material are further divided into:

- Hysteresis losses
- Classical eddy current losses
- Excess eddy current losses

Hysteresis (or static) losses are because of the motion of the magnetic domain walls and Barkhausen noise under externally applied magnetic field. Small sections of the domain walls make localized jumps that results in localized Eddy currents around the jumping wall segments [58]. These losses are directly affected by the microstructure of the material. Apart from the chemical composition, reducing the grain size, reducing mechanical stresses/strains, reducing the number of defects can result in the lowering of these losses.

The classical losses are due to Eddy currents that are produced due to an alternating magnetic field produced by an excitation current in the primary windings according to the Lenz's law. The magnetic flux generated by the induced current opposes the flux changes produced by the excitation current in the core. This opposing force prevents the flux from penetrating the core. The eddy currents result in the heating of the material and are, therefore, undesirable. Eddy currents are higher for materials that have higher conductivity, therefore they can be reduced by increasing the resistivity of the material. The addition of silicon in iron increases its resistivity and therefore helps in reducing the eddy current losses. Eddy current losses also increase with the frequency as they are directly proportional to the rate of change of induction (dB/dt). Eddy currents and, in turn, classical losses are strongly dependent on the sample geometry.

The excess or anomalous losses are due to the local damping of the movement of the domain walls. They also depend on the frequency and are higher for higher frequencies.

Bertotti developed a model to quantify these losses [58]. To use this model one has to first obtain several hysteresis curves at different frequencies. The area of the hysteresis curve gives (Eq. 2.13):

$$\frac{P}{f} = \int H \, dB \qquad \text{Eq. 2.13}$$

where:

P is the power loss

P/f is the loss per cycle

This power loss per cycle (P/f) is then plotted against the frequency and then fitted with the formula:

$$\frac{P}{f} = C_o + C_1 . f + C_2 . f^{1/2} \qquad \text{Eq. 2.14}$$

where:

C_o represents hysteresis or static losses, P_{hys}

C_1 represents the classical eddy current losses, P_{cl}

C_2 represents the excess losses, P_{exc}

The separation of these losses in non-oriented silicon steel is shown in Fig. 2.10.

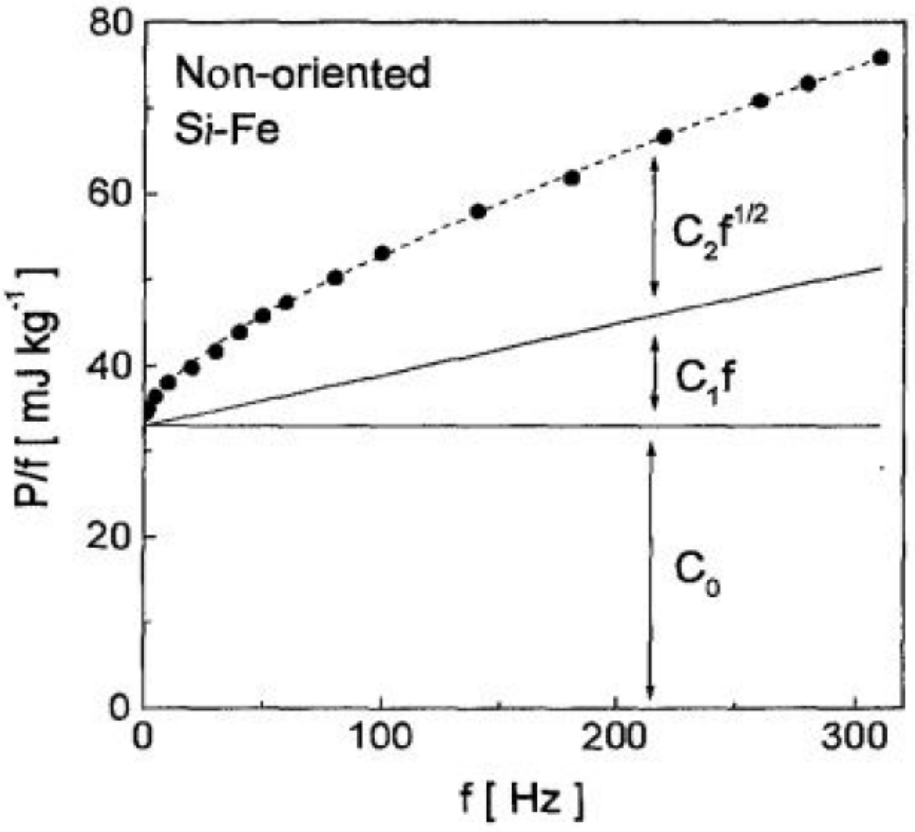

Figure 2.10: Separation of losses in non-oriented silicon steel according to [58].

Eq. 2.14 can be used to get a remarkable insight in the loss behavior of the material under investigation. However not all values obtained through this method are reliable or usable. If the error in the value (C_o, C_1, C_2) is of the same order of magnitude as the value itself or the value is negative then these are not suitable results to draw a conclusion from.

2.8 Magnetic Materials under study and their Properties

2.8.1 Fe-Si Alloys

Fe-Si alloys [68-77] are one of the most widely used soft magnetic materials in electrical industry. The phase diagram is shown in Fig. 2.11. Generally, they are used in transformers, generators, motors, and relays. Fe-Si alloys provide high permeability, low losses and high induction at a low price. Fe-3wt%Si alloy in oriented and non-oriented forms makes up a large part of the electrical industry. Its coercivity is about 40 A/m and its saturation magnetization is about 2T. Because of the low core losses grain-oriented Fe-Si alloys are mostly used for high energy transformers. Pure iron is a good soft magnetic material with a saturation magnetization of 2.15T at room temperature, however it exhibits high eddy current losses due to its high conductivity. Addition of silicon increases the resistivity of iron which reduces eddy current losses. The electrical resistance increases by 10 – 12 $\mu\Omega/cm^3$ for each percent of Si added. Iron also exhibits high magnetostrictions, whereas the magnetostriction decreases with silicon content [78-80] and at 6.5wt% Si magnetostriction is nearly zero [81]. Magnetostriction causes mechanical noise in transformers and is therefore not a desirable property in transformers. From a magnetic point of view, Fe-6wt%Si is the best composition which reduces both the magnetocrystalline anisotropy and the magnetostriction. This material has the highest permeability and the lowest coercivity among all Fe-Si alloys [82] but with some loss of saturation magnetization. However, with this composition, the alloy is very difficult to process because it is too brittle for conventional deformation processing routes like rolling etc.; HPT processing from as-cast materials or from powders before or after ball milling could be a solution in this respect. Addition of silicon in iron also has some shortcomings; namely, it reduces the saturation magnetization and deteriorates the mechanical workability. In short, going from Fe to Fe-3wt%Si to Fe-6.5wt%Si, specific

electrical resistivity increases, the core losses, coercivity, magnetostriction and anisotropy decreases. The saturation magnetization also decreases which is a negative point with Si addition.

It was proposed that Si improves the magnetic properties by precipitating the carbon present in iron in the form of graphite. Carbon in alloyed form is detrimental to the magnetic properties. When it is precipitated in the form of graphite due to Si then the magnetic properties are improved [68].

Several studies have been conducted on the high temperature phase equilibria of Fe-Si system [83-89]. It was found that above 10 GPa BCC phase turns into a mixture of BCC+HCP phase. The complete transition to HCP phase occurs close to 22 GPa at room temperature. In the present study the pressure was at or below 10 GPa and no phase other than the BCC phase was observed.

A similar work was done by [90] with Fe, Fe3wt%Si and Fe6.5wt%Si bulk materials among other materials. All of these samples were HPT-deformed at 8 GPa (40 tons) and 3 rotations at three different temperatures; 77K, room temperature and 723K (450 ^{o}C). This work substantiated the profound effect of stresses due to severe plastic deformation on the soft magnetic properties of the materials. This study managed to reduce the grain size below 100 nm and saw its effect on the coercivity, permeability and other such magnetic properties. The results showed that the coercivity increased substantially in all cases after HPT deformation. The coercivity of the samples deformed at 450 ^{o}C was higher than the samples deformed at room temperature or 77K. this was generally attributed to the large grain size which is expected at this temperature. The coercivity at 0 Hz, which is obtained by linearly extrapolating the coercivity data for f = 0 Hz, was plotted against the grain size. This plot showed significant deviations from the D^6 power law proposed by Herzer [55, 91]. These deviations were attributed to the stresses caused by HPT deformation. However the results overall showed that the exchange coupling is still a factor when the grain size is significantly below 100 nm. Also, there is a significant room for improvement if deformation-induced stresses are relieved without affecting the grain size obtained after HPT deformation. No heat treatments were conducted after HPT deformation in this study, however, magnetic measurements were conducted dynamically, i.e., the samples were heated in an oven from room temperature to 220 ^{o}C

and measurements were done at various temperatures. The results showed that, in general, the coercivity decreased with increasing temperature which could be attributed to a reduction in internal stresses. However, since the time of heating was very short, a substantial decrease in stresses does not seem likely.

This study was the basis for the present study. First of all, it was decided to use a higher number of rotations to see if a higher shear strain causes any further reduction in grain size. Secondly, apart from bulk Fe-3wt%Si and Fe-6.5wt%Si, powder versions of the same materials were also HPT-deformed under the same conditions to see if there is a difference in the behavior of two states of the material. Thirdly, heat treatments were devised based on DSC measurements to reduce internal stresses caused by HPT deformation without significantly increasing the grain size of the materials under investigation.

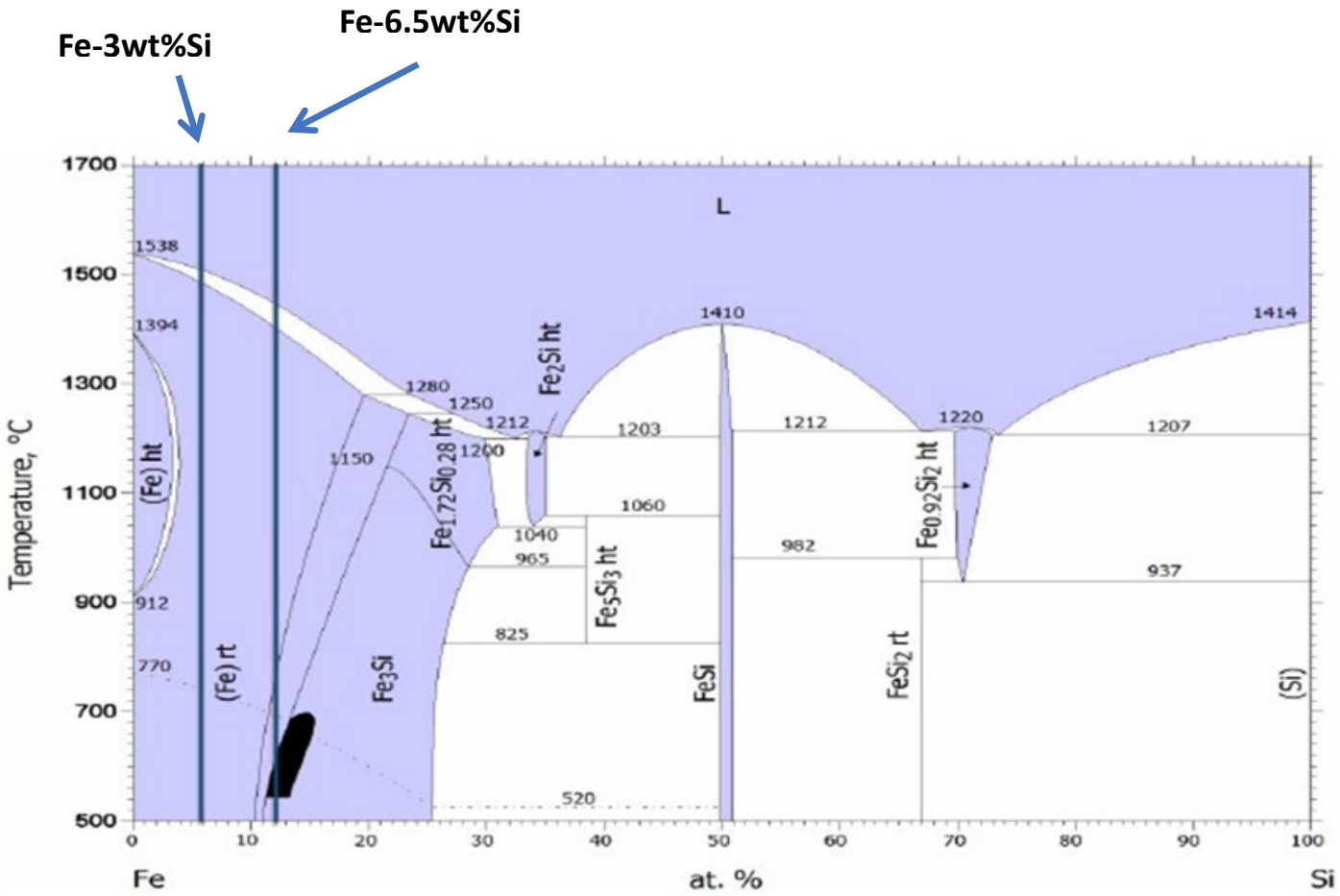

Figure 2.11: Binary phase diagram of Iron-Silicon system [92]. The arrows indicate the alloys with 3 wt% and 6.5 wt% Si are far in the solid solution area.

2.8.2 FINEMET-type Alloys

Since its invention in 1988 [93], FINEMET and its variations are among the most researched amorphous alloys to date [94-117]. Consequently, this invention sparked interest in magnetic amorphous alloys and a whole class of new soft magnetic materials was born. Apart from FINEMET, NANOMET (FeSiCuBP) [118-125] and HITPERM (Fe-Co-M-B-Cu (M=Zr, Hf, Nb)) [126-129] etc. are famous for their good soft magnetic properties. FINEMET has better coercivity but saturation magnetization is low (~ 1.2 T) which leads to size increase of the magnetic devices. NANOMET and other alloys try to improve saturation magnetization while sacrificing to some extent other soft magnetic properties. Some of the magnetic properties of these alloys are given in table. In general, the magnetic properties of these alloys in their amorphous states are nothing exceptional. However, when these alloys are heat treated in a controlled manner such that a nanocrystalline phase is produced within the amorphous phase, then these alloys show extraordinary magnetic properties. These properties depend upon the crystallite size, the volume fraction and the composition of the nanocrystalline phase.

FINEMET is an alloy of Fe-Si-Nb-Cu-B with a general composition of $Fe_{74-x}Cu_xNb_3Si_{13.5}B_9$. FINEMET owes its excellent soft magnetic properties to α-FeSi phase that is created within the amorphous matrix when the amorphous FINEMET is heat treated. The ideal heat treatment range is 520 ^oC – 580 ^oC for 1 hour [93]. Samples annealed at 460 ^oC showed relative magnetic hardening [98]. This temperature range changes slightly with the composition of the FINEMET. Annealing the amorphous alloy results in the nucleation of nanocrystals of α-FeSi phase which has a metastable DO3 structure. Fe diffusion in DO3-type Fe_3Si is extraordinarily fast due to high concentration of thermal vacancies [130]. The average grain size is between 10 and 15 nm. The Si content in the α-Fe is around 23 at%. A Cu-rich phase is also present with about 60 at% Cu and less than 5 at% of each Nb, B and Si. Fe concentration is less than 30 at% in this phase. Once α-FeSi is nucleated, Nb and B are rejected to the amorphous phase. The concentration of Nb and B in the remaining amorphous phase increases as the α-FeSi phase grows [94].

FINEMET-type alloys are usually produced through single-roller melt-spinning techniques. In this technique a stream of melted alloy composition is dropped on a water-

cooled rapidly rotating copper wheel. This created amorphous ribbons of FINEMET with a thickness of around 20 µm. A twin-roller melt-spinning technique was used that was able to induce nanocrystallization during the quenching process of the melted alloy [131]. However, the magnetic properties were not as good as the one obtained from annealing the amorphous ribbon after its production. The reason is that inducing nanocrystallization on the wheel results in large internal stresses in the ribbon which deteriorate magnetic properties.

Annealed samples show decreased coercivity because of exchange interaction (discussed in Section 2.4) that averages out locally fluctuating anisotropies due to high density of nanocrystals [98] as described by the Random Anisotropy Model (discussed in Section 2.6). It was found that if magnetic anisotropy is induced during the crystallization process (one-step annealing) it is up to ten times stronger than when the anisotropy is induced by post-annealing of the crystallized samples in a magnetic field (two-step annealing) [130].

Role of Cu & Nb in FINEMET Alloys

The high nucleation rate of α-Fe_3Si nanocrystals along with their small size (~ 10-15 nm) is attributed to the simultaneous presence of Cu and Nb in the alloy composition. There are different theories/models that describe how the synergistic effect of Cu and Nb achieves a high nucleation rate and a low growth rate of the nanocrystalline phase. These are briefly described below:

- Prodell [132] suggested that the crystallization in the FINEMET alloy proceeds very fast during annealing but the last stages are diffusion-limited.
- Yavari [133] suggested that the accumulation of large Nb atoms at the interface of the nanocrystals resulted in a diffusion layer that inhibited the growth.
- Ayers [134] suggested that Cu clusters with near-FCC structure present at the very start of crystallization process provided a low energy interface for the growth of DO3 crystallites.
- Hono [135] studied the effect of Cu addition on many amorphous alloys and concluded that Cu clusters formed in the quenched alloy served as the nucleation sites.

- Blázquez [136] suggested that soft impingement of overlapping diffusion fields hindered the nanocrystal growth.
- Zhang [100] suggested that there is a repulsion between Cu and Nb as dictated by the Cu-Nb phase diagram. This repulsion results in the formation of Cu and Nb clusters which serve as heterogeneous nucleation sites. As the repulsive interaction grows, phase separation in stable amorphous state increases. Due to this repulsion the alloy is divided into Cu-rich and Nb-rich regions. Therefore, during annealing Cu and Nb can serve as nucleation sites for the formation of α-Fe_3Si nanocrystalline phase. In the region where there is low crystal density, the Nb clusters act as nucleation sites due to the strong interaction between Si and Nb atoms and negative enthalpy of mixing of Fe and Nb atoms. Due to the repulsion between Cu and Nb atoms, Cu is rejected by the formation of Nb clusters. Thus the concentration of Cu is higher at the interface of nanocrystals. This increases in Cu concentration can increase the diffusive interactions between Si, B, Nb and Cu atoms thus reducing the growth rate [137]. In the region where the crystal density is high, Cu concentration is much higher in the center of the crystal than the outside (thus confirming Ayers theory that Cu clusters provide interface for the Fe_3Si crystals to grow on them). This indicates that Cu clusters initially form in the amorphous phase, followed by the nucleation and growth of the Fe_3Si phase on the clusters. A higher number of Nb atoms are observed in between the nanocrystals which verifies the soft impingement model of Blázquez. This impingement restricts the crystal growth. Indeed Shivaee et. al. [138] showed that reducing Cu & Nb in the composition resulted in a larger grain size at the same temperature.

The presence of Cu & Nb on one hand helps achieve low coercivity but on the other hand it severely reduces the saturation magnetization of the alloy. It would be highly desirable to get the same volume fraction and the same size of α-Fe_3Si nanocrystals without the presence of Nb & Cu. Therefore the research is ongoing where amorphous Fe-B and Fe-Si-B alloys are processed through SPD/HPT in order to get nanocrystalline phase with comparable soft magnetic properties [9, 139].

Fujii et. al. [101] annealed FINEMET between the Curie temperature of amorphous phase (586 K) and that of the crystalline phase (920 K) in the presence of magnetic field (0 – 6T). XRD shows that magnetic field caused preferential formation of {110}-oriented nuclei. Applied field enhanced crystallization kinetics particularly the nucleation rate. Saturation magnetization (measured through VSM) was increased by the application of the magnetic field up to 4T during nanocrystallization. The average grain size was unaffected by the magnetic field.

FINEMET in its amorphous state is very ductile and easy to work with. However, its magnetic properties are not as good as its crystalline form. Apart from annealing, partial or full crystallization can be induced through intensive plastic deformation. Severe plastic deformation localized into adiabatic shear bands results in very high temperature in the bands that results in structural changes in the amorphous alloy. These changes result in the embrittlement of the sample [11]. These deformations, however, deteriorate the magnetic properties.

Gavrilovic et. al. [140] studied the structural transformation of FINEMET under isothermal and non-isothermal conditions. Heating rates were kept low to induce stepwise structural transformations. XRD showed that primary crystallization started with the formation of an FCC Fe_3Si phase within the amorphous matrix. Between 780 and 920 K, volume fraction of Fe_3Si became constant at 85 wt% while $FeCu_4$, $Fe_{16}Nb_6Si_{17}$ and Fe_2B phases were formed. Above 923 K Si migrated from Fe-Si phase to the Nb-rich grain boundaries. Two new phases, Fe_5Si and Nb_5Si_3 were formed at this stage at around 973 K. Below 923 K the crystallite size of Fe_3Si was around 10 nm, while above 1123 K it was around 500 nm. A comprehensive list of the phases formed, their wt% and average grain/crystallite size are given in [140].

Han et. al. employed a two-step annealing process. Samples were first heat treated at 400 ^oC for 1 hour and then nanocrystallized at 560 ^oC for 1 hour. This treatment resulted in better soft magnetic properties with higher initial permeability μ_o of 9.16 x 10^4 and lower core losses [141]. Lashgari et. al. found that a stress-relaxation treatment at $T<<T_g$ slightly improved magnetic texture by 6% but treatment at $T=T_g$ deteriorated magnetic texture [113]. For NANOMET alloys, Makino et. al. showed that flash annealing (heating rate of 400 ^oC/min) resulted in the formation of nuclei which resulted in achieving a

combination of uniform and refined grain size (d < 20 nm) and good soft magnetic properties [142, 143]. It should also be noted that heating during the service (thermal aging) of the crystalline FINEMET degrades all of its magnetic properties [110].

Several different alloying additions has been done in the FINEMET composition to further improve the magnetic properties of the alloy. Some of these are described below:

- **Mo addition:** Mushnikov et. al. found that Mo addition reduced the temperature of the onset of crystallization, decreased the phase separation and decreased the recrystallization [144]. Jiang et. al. found that complete substitution of Nb with Mo deteriorated soft magnetic properties. Mo substitution reduced crystallization temperature to 15 minutes [145]. Wan et. al. found that Mo addition improved saturation magnetization up to 1.72 T while coercivity was deteriorated (~ 10.8 A/m) [146].
- **Co addition:** Co addition improved the Curie temperature of the FINEMET [147].
- **Ni addition:** Kataev et. al. found that Ni addition of up to 3 at% increases Curie temperature and magnetization of the alloy. Addition of more than 6 at% deteriorated the properties [148].
- **V addition:** Partial substitution of Nb with V results in a larger grain size at the same temperature. The magnetic properties are comparable to that of original FINEMET alloy [149].
- **Ti addition:** Replacing Nb with Ti reduces the onset primary crystallization temperature from 803 K to 758 K. Ti is not an effective grain growth retarder. Soft magnetic properties deteriorated with Ti addition [150].

2.9 Goals of the Present Work

- Using HPT processing to improve the soft magnetic properties of Fe, Fe-3%wtSi and Fe-6wt%Si alloys by reducing the grain/subgrain size to a magnitude where the exchange coupling effect becomes operative.
- To find out whether there is any difference between the HPT-processing and magnetic properties of bulk and powder Fe-3wt%Si and Fe-6wt%Si.

- Using the HPT technique for getting bulk nanocrystalline materials out of amorphous or nanocrystalline FINEMET-type foils.
- Applying careful heat treatment to reduce stresses and HPT-induced defects without increasing the grain/subgrain size in order to improve the magnetic properties.
- To determine how grain/subgrain size and dislocations affect the soft magnetic properties such as coercivity, magnetic losses, permeability etc.
- To determine if D^6 or D^3 power laws proposed by Herzer are applicable to the systems under study or if there is a new power law that can more accurately describe the magnetic properties, namely the coercivity, of these materials.

2.10 Tasks of the Present Work

The emphasis of the current PhD thesis will be given to the following research tasks:

For crystalline Fe-Si alloys:

- Reduction of grain/subgrain size of powder Fe-3wt%Si and Fe-6.5wt%Si alloys down to a diameter of less than 50 nm using the HPT technique. Most important here is that grains sizes are achieved which are small enough to achieve exchange coupling. Low temperature processing as well as sophisticated ways of thermal treatment may be necessary to reach this goal.
- Reduction of grain/subgrain size of bulk Fe, Fe-3wt%Si and Fe-6.5wt%Si alloys down to a diameter of less than 50 nm using the HPT technique.
- Performing heat treatment to reduce the extent of internal stresses and/or density of lattice defects in the samples. DSC (Differential Scanning Calorimetry) may help to identify the defects according to their annealing characteristics.
- Determination of crystallite/subgrain size through X-ray Line Profile Analysis (XLPA), and of grain size by Transmission Electron Microscopy (TEM).
- Preparation of ring-shaped samples using spark erosion.
- Measurement of magnetic properties, such as coercivity, saturation magnetization, frequency dependence of losses, permeability etc., using a

hysteresisgraph. And finally, finding out whether crystallite (subgrain) size or grain size governs the magnetic properties.

- Derive a power law that describes the coercivity vs the subgrain size of the materials under study.

For FINEMET amorphous and nanocrystalline alloys:

- Production of bulk FINEMET-type alloys using high-pressure torsion technique.

Chapter 3: Experimental

3.1 Materials Used

This research focuses on two different systems:

3.1.1 Fe-Si Alloys

First system consists of Fe, Fe-3wt%Si and Fe-6.5wt%Si alloys. Iron samples were in the bulk form while Fe-3wt%Si and Fe-6.5wt%Si were in both bulk and powder form. The phase diagram of Fe-Si system is shown in Fig. 2.11. The initial particle size of Fe-3wt%Si is 150µm and that of Fe-6.5wt%Si is 180µm. The powders were obtained from Höganäs Belgium SA. These Fe-Si alloys are already being used for soft magnetic application for a very long time. However, as mentioned earlier, reducing the grain size down to nanometer level will have a dramatic effect on the soft-magnetic properties.

The bulk Fe-3wt%Si and Fe-6.5wt%Si were prepared at the Technical University of Vienna (Technische Universität Wien) by melting appropriate amounts of iron and silicon in an arc melting furnace.

3.1.2 FINEMET-type Alloys

The second system consists of FINEMET-type alloy composition based on Fe-Si-B-Nb-Cu system. This material is known as VITROPERM and is procured from VACUUMSCHMELZE GmbH & Co. KG, Hanau, Germany. The exact chemical composition is $Fe_{73.5}Cu_1Nb_3Si_{15.6}B_{6.6}$ (at%). There are two variations of this material: VITROPERM which is amorphous, and VITROPERM VP 800 which is annealed at about 550 ^oC to produce a two-phase amorphous & nanocrystalline grain structure (mean grain diameter 10-20 nm). The density of amorphous VITROPERM is 7.07 g/cm^3 while that of nanocrystalline VITROPERM is 7.35 g/cm^3.

3.2 Materials Preparation

3.2.1 High-Pressure Torsion (HPT)

The primary technique used for the preparation of samples in this research is the high-pressure torsion (HPT) technique. A photograph of HPT equipment used is shown in Fig. 3.1 and its schematic sketch is shown in Fig. 3.2. This HPT equipment can apply up to 10 GPa of pressure and a temperature between 77 K and 773 K. Moreover, at high temperature the equipment is shielded from the atmosphere and the chamber is flushed with Argon throughout the experiment to avoid any oxidation. The speed of rotation (rpm) can be set according to the requirements of the material under processing.

The type of HPT used is known as quasi-constrained HPT. In this type of HPT both anvils have depressions and material is placed in between these depressions. This allows for a limited outward lateral flow during processing.

Figure 3.1: Photograph of High-Pressure Torsion (HPT) equipment available with the Research Group Physics of Nanostructured Materials at the Faculty of Physics, University of Vienna.

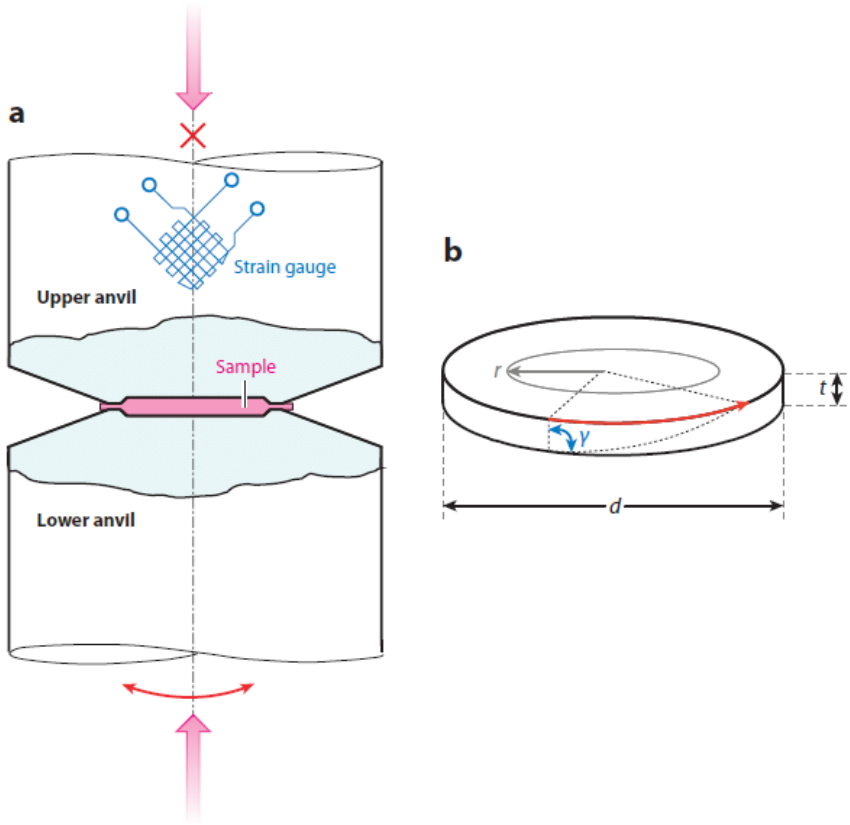

Figure 3.2: Schematic illustration of (a) HPT deformation, (b) the torsional deformation of the sample [151].

Fe, Fe-3wt%Si and Fe-6.5wt%Si Bulk & Powder Samples

For bulk Iron, Fe3wt%Si and Fe6.5wt%Si round disks were cut from the bulk material using spark erosion machine. For powder Fe3wt%Si and Fe6.5wt%Si samples one gram of powder was placed on the lower cavity. The parameters used for HPT processing are as follows:

8 mm samples were cut out of the 9 mm samples that came out after HPT processing. This was done to remove any extraneous material and any cracks that usually occurred at the edge of the sample.

Table 3.1: HPT processing parameters for bulk and powder Fe, Fe-3wt%Si and Fe-6.5wt%Si samples.

HPT Parameters	Bulk Samples	Powder Samples
Diameter of disk	10 mm	5 g powder
Thickness of disk	0.8 mm	-
Depth of anvil cavity	0.1 mm	0.1 mm
Diameter of anvil cavity	9 mm	9 mm
Pressure	8 GPa	8 GPa
Temperature	77 K and 300 K	77 K and 300 K
Number of rotations	20	20
Speed of rotation	0.3 rpm	0.3 rpm

With regards to material processing, powder Fe-3wt%Si samples were much more prone to cracking than their bulk counterparts especially under liquid nitrogen. It should be noted that this was not microcracking on the surface of the sample that is visible under a microscope, rather it was a large crack on the edge of the sample that goes across the sample due to sudden unloading at the end of the experiment. All samples were prone to this cracking but the powder samples were especially vulnerable. These samples were unfit for magnetic testing so several attempts were made to get good crack-free samples for magnetic testing. The shear strain Y and true accumulated strain Ɛ of the powder samples is also larger than their bulk counterparts.

With regards to HPT processing, powder Fe-6.5wt%Si samples were the hardest to process. Almost all samples cracked during unloading, and after making dozens of samples only a few samples were obtained for magnetic testing. Bulk samples also cracked but the ratio of successful samples was a little better.

FINEMET Amorphous & Nanocrystalline Materials

Amorphous FINEMET material was in the form of 20 µm thick, 12 mm wide and several meters long strip. The strips were punched with a punching tool according to the dimensions of the anvil depression. The circular pieces were then layered on top of each

other and tied with a thread as shown in Fig. 3.3. The thread breaks as soon as the two anvils press with each other and does not become a part of the final sample. The sample does not form without holding the pieces down with the thread.

Figure 3.3: Sample preparation of FINEMET Amorphous material.

Nanocrystallized FINEMET material was in the form of 20 μm thick, 12 mm wide and several meters long strip. This material is as brittle as a thin sheet of glass therefore it cannot be punched with a punching tool. Small pieces roughly the size of the anvil depression were cut and placed on the anvil and held down with threads. The thread breaks as soon as the two anvils press with each other and does not become a part of the final sample. The sample does not form without holding the pieces down with the thread.

Table 3.2.: HPT processing parameters for amorphous and nanocrystalline FINEMET samples

HPT Parameters	Amorphous FINEMET	Nanocrystalline FINEMET
Number of layers	60	60
Depth of anvil cavity	0.25 mm	0.25 mm
Diameter of anvil cavity	7 mm	7 mm
Pressure	10 GPa	10 GPa
Temperature	300 K, 473 K, 573 K, 673 K	300 K
Number of rotations	20	20
Speed of rotation	0.1 rpm	0.2 rpm

6 mm samples were cut out of the 7 mm samples that came out after HPT processing. This was done to remove any extraneous material and any cracks that usually occurred at the edge of the sample.

3.2.2 Production of Ring Samples through Spark Erosion

To precisely cut the ring samples for magnetic measurements spark erosion machine was used. The steps from rough HPT-processed sample to the final ring sample are shown in Fig. 3.4.

- For the purposes of this thesis a ting with outer diameter of 8 mm and an inner diameter of 6 mm was prepared.
- The HPT-processed sample is first glued to a metallic stub (Fig. 3.4a).
- First a circular tool made of copper or brass with a diameter of 8 mm is used to remove the extraneous material (Fig. 3.4b).
- Without moving the stub from the machine, the tool is changed with a 6 mm circular tool. It is difficult to cut a precise ring just by visual means. To get a good ring sample the spark erosion machine is turned on for 15 to 30 seconds such that the 6 mm tool makes just a light impression on the sample (Fig. 3.4c). This impression gives a very good indication of whether the final ring will be concentric

or not. If the ring does not look concentric, very gently move the X and Y axes of the machine to further place the cutting tool more accurately.

- Finally we get a ring sample that is acceptable for magnetic measurements (Fig. 3.4d).

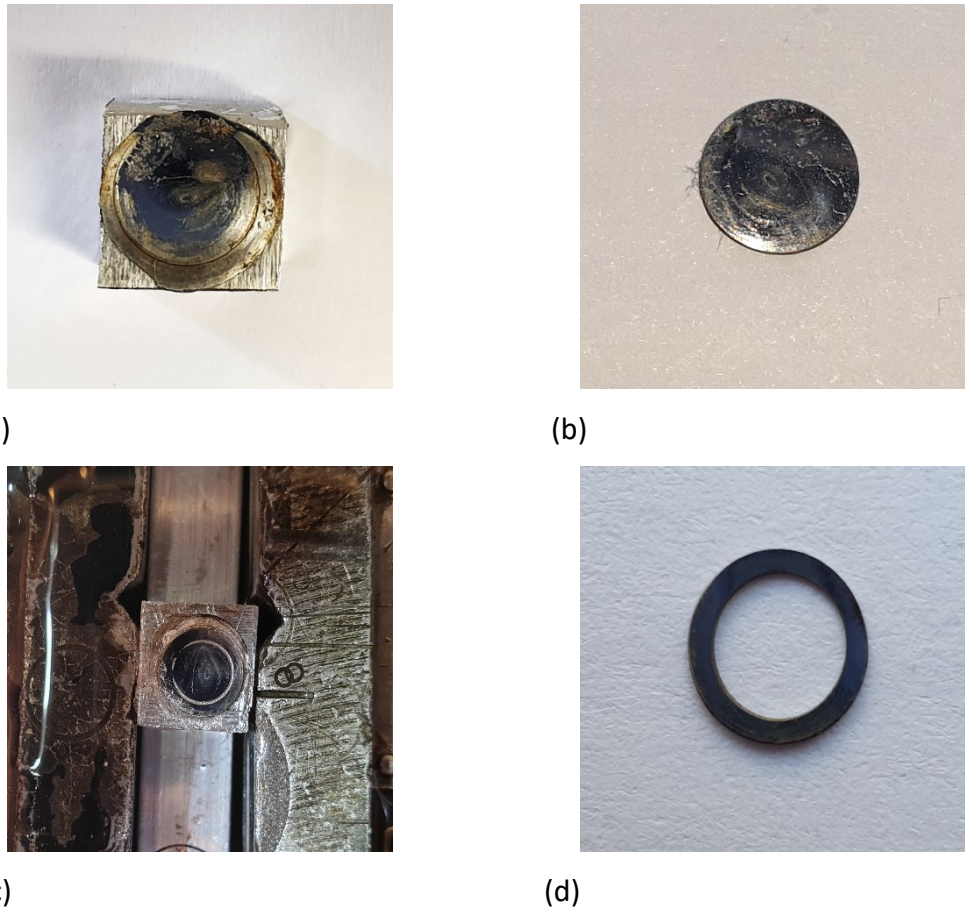

(a) (b)

(c) (d)

Figure 3.4: Various steps in the formation of ring samples for magnetic measurements through spark erosion machine.

3.2.3 Nanoindentation

To gauge the effect of heat treatment on the mechanical properties of Fe-Si-X alloys, hardness was checked through nanoindentation. Nanoindentation [152, 153] is a very useful technique to measure the hardness H and elastic modulus E of the materials. Hardness and elastic modulus then, in turn, provide great insight into other mechanical properties of the material under investigation without going through cumbersome sample preparation steps. Additionally, it can measure hardness of individual grains or

individual phases in multiphase materials. This technique is equally applicable to metals, polymers and ceramic materials. Both hardness and elastic modulus are determined from a single nanoindentation load-displacement measurement without the need of imaging the indent's impression. A typical load-displacement curve is shown in Fig. 3.5.

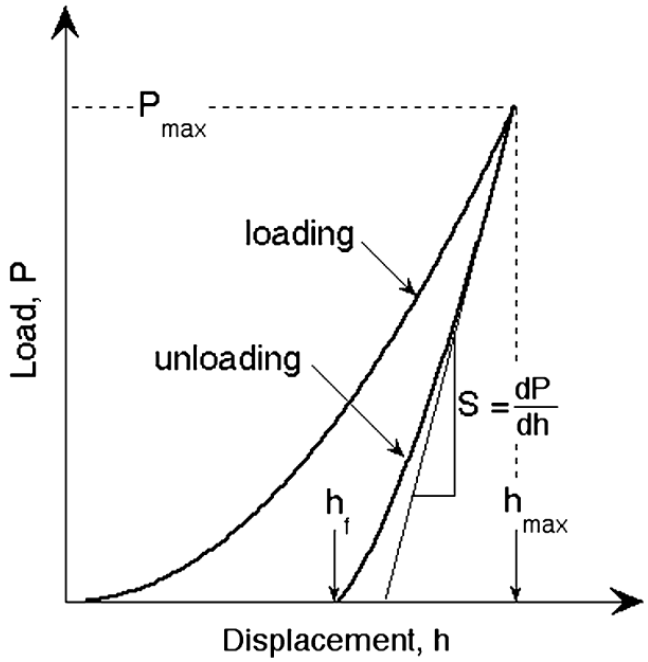

Figure 3.5: Load-displacement curve during one cycle of loading and unloading [153]. h_{max} is the total displacement of the indent at maximum load P_{max} and h_f is the net plastic deformation after recovery of the elastic part during unloading [154].

A known load (usually of the order of mN) is applied to the indenter in contact with the specimen. The depth of penetration of the indenter in the sample is measured with a high accuracy. When the load reaches its maximum point, the area of contact is calculated by the depth of the impression and the already known angle of the indenter. Hardness H would then be the ratio of maximum load P_{max} and the area of contact A as shown in Eq. 3.1. Elastic modulus E is measured from the shape of the unloading curve. Schematic of unloading process of the indentation is shown in Fig. 3.6.

$$\boldsymbol{H = P_{max}/A_c} \qquad \text{Eq. 3.1}$$

where:

P_{max} is maximum load

A_c is the contact area of indenter

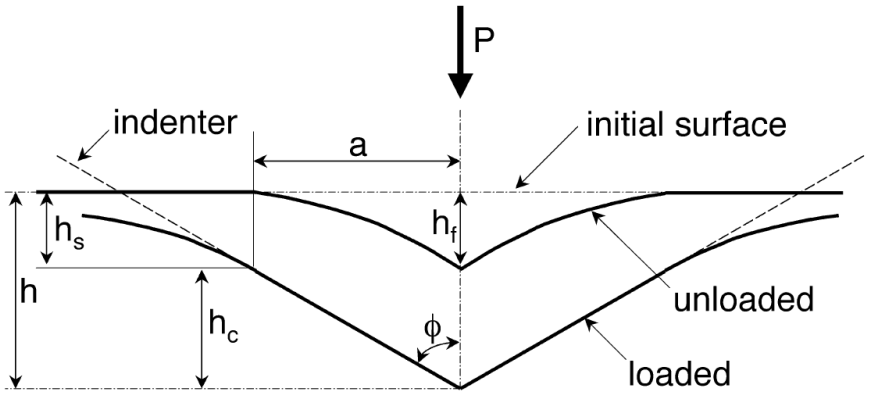

Figure 3.6: Loading and unloading process of the indentation [153].

Nanoindentation analysis is based on the behavior of the unloading curve. This curve is non-linear and it is modelled using a power-law relation:

$$\boldsymbol{P = \alpha(h - h_f)^m} \qquad \text{Eq. 3.2}$$

where:

α and m are power-law fitting parameters.

Assuming there is no pile-up of the material we can find the sink-in height h_s for the Vicker's indenter by using the equation:

$$\boldsymbol{h_s = \varepsilon P_{max}/S} \qquad \text{Eq. 3.3}$$

where:

ε is the indenter shape factor

The contact depth h_c along which the contact is made between the material and the indenter is given by the relation:

$$\boldsymbol{h_c = h_{max} - \varepsilon P_{max}/S} \qquad \text{Eq. 3.4}$$

The contact area A_c in Eq. is a function of the contact depth h_c and it is estimated by the equation:

$$\boldsymbol{A_c = f(h_c) = \sum_{n=0}^{8} C_n (h_c)^{2-n}} \qquad \text{Eq. 3.5}$$

The samples were first grinded by 600 and 1200 grit paper, then polished to a mirror finish by 1 µm and 0.3 µm Alumina paste. The hardness measuring cycle is shown in Fig. 3.7. The load used was 100 mN using a Vicker's indenter in UNAT equipment from ASMEC laboratories. The hardness standard followed during the nanoindentation testing was ISO14577. A total of 72 indents were applied on each sample. As discussed above the samples were in the form of ring samples with outer diameter of 8 mm and an inner diameter of 6 mm. This gives a ring width of 1.5 mm. The indents were placed and the hardness was measured in the center of these rings. The Poisson's ratio was assumed to be 0.30 for Fe and Fe-Si samples and 0.33 for amorphous FINEMET sample. The nanoindentation machine makes adjustments for thermal drift etc.

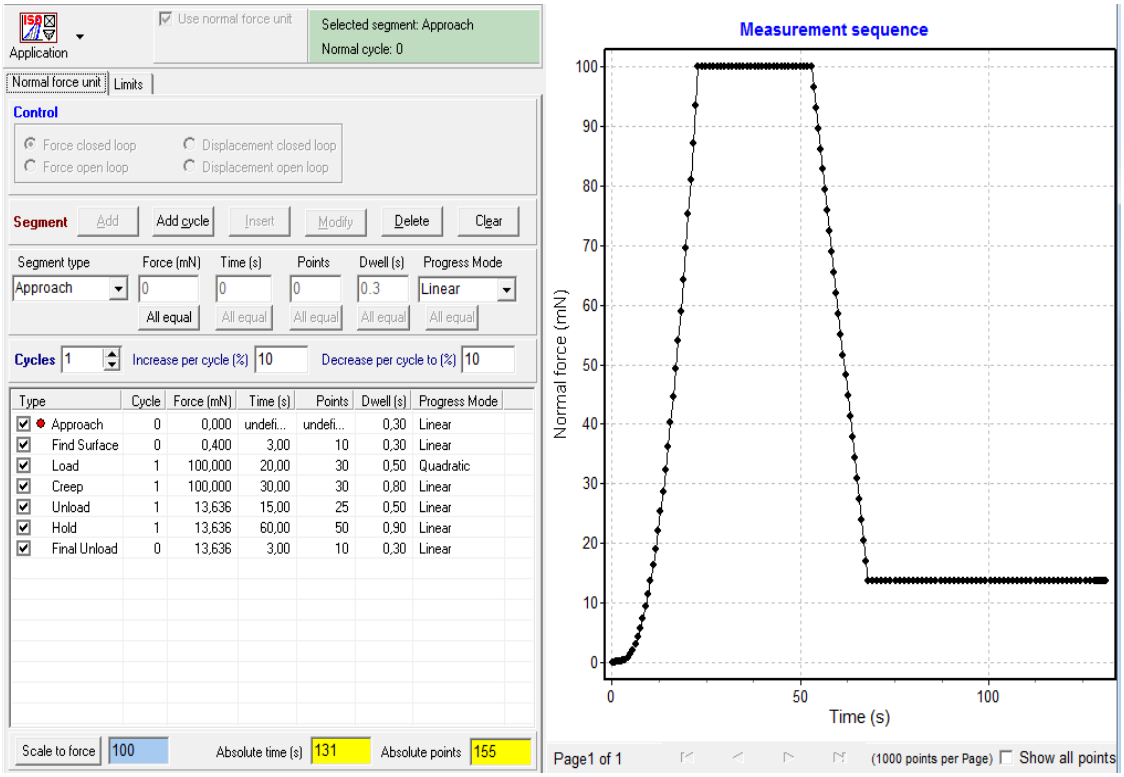

Figure 3.7: The hardness measuring cycle for the ISO14577 nanoindentation tests (from the software).

3.2.4 X-ray Line Profile Analysis (XLPA)

X-ray line profile analysis (XLPA) [155-159] is a very useful and powerful tool to get an insight into the material using X-ray diffraction. Severe plastic deformation induces a large number of defects and stresses in the material under processing. These stresses and defects change the peak profile of the XRD pattern. The width of the peak, its shape

and position on the 2θ scale can be used to determine the coherently scattering domain size (CSD) and dislocation density of the material among other things. The deviation from an ideal narrow diffraction pattern reveals several aspects of the microstructure under examination. For example:

- The peak broadening indicates the size of the crystallite and the presence of microstresses/microstrains, stress/strain gradients and chemical heterogeneities preferably in connection with lattice defects e.g., dislocations.
- The peak shift indicates internal stresses or planar faults.
- The anisotropic peak broadening indicates the presence of an anisotropic crystallite shape or anisotropic strain.
- The peak asymmetries indicate long-range internal stresses/strains, planar faults or chemical heterogeneities.

To find out the crystallite or coherently scattering domain (CSD) size and the dislocation density of the samples, a profile fitting procedure known as Convolution Multiple Whole Profile (CMWP) [160, 161] was used. It is based on a model that utilizes Fourier transforms for size broadening and strain broadening of the XRD peaks. This procedure assumes spherical crystallites that follow a log-normal size distribution. The strain in this case is assumed to be associated with the dislocations. In the CMWP procedure the diffraction pattern (Intensity I vs. 2θ profile) of the sample is described by the convolution of crystallite size (S) and defect distortion (D) intensity profiles as described by the equation:

$$\boldsymbol{I^{Net} = I^{S} * I^{D} + I^{BG}} \qquad \text{Eq. 3.6}$$

where:

I^{BG} is the background intensity.

The intensity profile I^{Net} can be expressed as cosine Fourier function $F_c(S)$ as:

$$\boldsymbol{F_c(S) = 2\int_0^{\infty} A(L)Cos(2\pi LS)dL} \qquad \text{Eq. 3.7}$$

where:

L is the Fourier length

The Fourier coefficient of the peak profile A(L) is given by:

$$\boldsymbol{A(L) = A^s(L) * A^D(L)} \quad \text{Eq. 3.8}$$

where:

$A^S(L)$ is the size Fourier coefficient

$A^D(L)$ is the distortion Fourier coefficient

$A^S(L)$ coefficient is a function of the median m and variance σ of the log-normal distribution. Assuming the strain is only due to dislocations, $A^D(L)$ can be expressed as:

$$\boldsymbol{A^D(L) = exp(-2\pi^2 g^2 L^2 < \varepsilon_{g,L} >^2} \quad \text{Eq. 3.9}$$

where:

g is the absolute value of the diffraction vector

$<\varepsilon_{g,L}>^2$ is the mean square strain caused by the dislocations.

$<\varepsilon_{g,L}>^2$ is estimated using the Wilkens' dislocation model [162] which is represented by the equation:

$$\boldsymbol{\varepsilon_{g,L} = \left(\frac{b}{2\pi}\right)^2 \pi \rho C f\left(\frac{L}{R_e^*}\right)} \quad \text{Eq. 3.10}$$

where:

L is the Fourier length

b is the Burgers vector

ρ is the dislocation density (represented by N in Chapter 5)

C is the contrast factor of the dislocations. Its value depends on the relative orientations of the line, Burgers and diffraction vectors.

R_e^* is the effective outer cut-off radius of a dislocation

g and L need to be small for this model to be valid.

If all the possible slip systems in a crystal are equally populated or if there is no texture in the crystal then $\overline{C}$ becomes the weighted average for C for a particular g and b. For a cubic crystal:

$$\overline{C} = \overline{C}_{h00}(1 - qH^2) \quad \text{Eq. 3.11}$$

where:

$\overline{C}_{h00}$ is the average dislocation contrast factor for h00 type reflections.

q is the fitting parameter and it depends on the elastic constants of a crystal (C_{11}, C_{12} and C_{44}), the anisotropy factor $A_i = 2C_{44}/(C_{11} - C_{12})$, and the ratio of C_{11}/C_{12}. [163]

$H^2 = (h^2k^2 + h^2l^2 + k^2l^2)/(h^2+k^2+l^2)$

The most important point for the successful application of this method is to obtain a high-quality experimental data. The lower the background noise and the more defined the peak profile the easier it would be to get reliable results. In this work a rotating X-ray generator Rigaku MM9 with a Co target (K_α = 0.178892 nm) and a Ge-monochromator was used. The detector is a position sensitive detector INEL CPS590 with 2θ angular range of 90°.

The sample/material related parameters such as lattice parameters, Burgers vector, wavelength of the radiation used etc. are fed into the CWMP program then the starting values of the fitting parameters (a, b, c, d, e) are varied. The experimental data is modelled using least square optimizing algorithms [161, 164, 165].

The fitting parameters a, b, c, d, e are related to the physical quantities as:

$$\boldsymbol{q = a} \quad \text{Eq. 3.12}$$

$$\boldsymbol{m = exp(b)} \quad \text{Eq. 3.13}$$

$$\boldsymbol{\sigma = c/\sqrt{2}} \quad \text{Eq. 3.14}$$

$$\boldsymbol{\rho = 2/\pi(b_{Burgers}\, d)^2} \quad \text{Eq. 3.15}$$

$$\boldsymbol{R_e^* = exp(-\frac{1}{4})/-2e} \quad \text{Eq. 3.16}$$

The obtained quantities q, m, σ, ρ, R_e* are saved in a file by the software. These are then statistically averaged (within 10% variation). The average crystallite size $<X_{area}>$ is then calculated by the equation:

$$< \boldsymbol{X_{area}} > = \boldsymbol{m\ exp}(\mathbf{2.5}\boldsymbol{\sigma^2}) \qquad \text{Eq. 3.17}$$

where:

m is the mean crystallite size

σ is the variance.

One of the parameters obtained after the analysis of the XRD data through the CWMP program is called the dislocation arrangement parameter or M-parameter. M is an indicator for the strain field intensity as it normalizes the external dislocation cut-off radius $\boldsymbol{R_e}$* to the mean distance of dislocations, according to **M** = $\boldsymbol{R_e}$* $\sqrt{\boldsymbol{\rho}}$ with $\boldsymbol{\rho}$ as the dislocation density. It can be directly derived from the line profile. If M >> 1 then this represents a long-range strain field. If M ~ 1 then this represents screening of strain field of neighboring dislocations. If M << 1 then this represents dislocation dipoles. In practice, the accuracy of measurement of M is sometimes poor as it depends on the quality of the Bragg profiles measured; but at least the measured M-parameters can be used for relative comparisons of results from experiments done under identical conditions. It should be noted that the M-parameter is linearly connected to the so-called dislocation configuration parameter α which e.g. is part of the Taylor equation 5.3 (see Section 5.3.2) with the same physical meaning as M.

Before the start of the experiment all samples were first grinded by 600 and 1200 grit paper, then polished to a mirror finish by 1 μm and 0.3 μm Al_2O_3 particle paste. Care was taken to grind the samples minimally in order not to introduce new stress/strains conditions in the samples.

3.2.5 Differential Scanning Calorimetry (DSC)

Differential Scanning Calorimetry [166] (DSC) is a method to investigate the thermal properties and phase transitions of the materials under controlled conditions. The

sample under investigation is placed alongside a reference sample in the machine in the same atmosphere. The difference in the heat flow between the sample and the reference is then measured as a function of temperature. Reference sample is chosen such that it does not go under any phase change during the experiment. So, for example, aluminum pans are used for experiments conducted below 600 ^{o}C while for experiments above 600 ^{o}C platinum pans are used.

As the sample is heated over a temperature range, there may come a point where the sample may undergo a phase change or lose crystal defects. This change may release some energy (exothermic reaction) or absorb it (endothermic reaction). This release/absorption of energy appears in the heat flow curve. The time derivative of the heat flow Q at constant pressure P is equal to the time derivative of the enthalpy H:

$$\left(\frac{\boldsymbol{dQ}}{\boldsymbol{dt}}\right)_{\boldsymbol{p}} = \boldsymbol{dH/dt} \qquad \text{Eq. 3.18}$$

where:

$H = m\ C_p\ \Delta T$

C_p is the specific heat in J/g.K at constant P

m is the mass of the sample in g.

ΔT is the change in temperature in K.

Differentiating Eq. 3.18 we get:

$$\frac{\boldsymbol{1}}{\boldsymbol{m}}\left(\frac{\boldsymbol{dH}}{\boldsymbol{dt}}\right) = \boldsymbol{C_p\ dT/dt} \qquad \text{Eq. 3.19}$$

The difference in heat flow between the sample and the reference is then given by:

$$\Delta\left(\frac{\boldsymbol{dH}}{\boldsymbol{dt}}\right) = \left(\frac{\boldsymbol{dH}}{\boldsymbol{dt}}\right)_{\boldsymbol{sample}} - \left(\frac{\boldsymbol{dH}}{\boldsymbol{dt}}\right)_{\boldsymbol{reference}} \qquad \text{Eq. 3.20}$$

For an exothermic process ΔH is negative and the curve will show a downward peak while the reverse is true for an endothermic process. Crystallization, grain growth, annihilation

of various defects are examples of exothermic reactions that are relevant to this research.

There are two types of DSC methods that are used [167]; heat flux DSC and power compensated DSC. For this research Netzsch DSC204 was used which is a heat flux DSC. In this DSC the sample and reference pans are connected by a low-resistance heat flow path. The furnace is heated at a linear heating rate. The sample and the reference materials have different heat capacities therefore there would be a temperature difference between them. The heat flow is calculated through this temperature difference using the equation:

$$\boldsymbol{Q = \Delta T / R} \qquad \text{Eq. 3.21}$$

where:

Q is the sample heat flow

ΔT is the temperature difference between the sample and reference

R is the resistance of the heat flow path.

In this research the reason for performing DSC was to determine the specific heat treatment of HPT-deformed samples necessary for selective removal of lattice defects. All samples were enclosed in aluminum pans to protect them from oxidation at high temperature. A constant flow of high-purity argon was also maintained during the experiment. The samples were heated from room temperature to 590 ^{o}C with a heating rate of 10 K/min.

3.2.6 Transmission Electron Microscopy (TEM)

Transmission electron microscopy is the ultimate materials‘ characterization technique that can reveal the structure of the material down to atomic level. In this technique a high energy beam of electrons goes through a specially prepared thin sample (~ 30 nm) and forms an image on a phosphor screen. Alternatively a diffraction pattern is formed in the reciprocal space if the objective aperture is removed and a selected area diffraction (SAD) aperture is inserted at the image plane of the objective lens. The objective aperture controls the collection angle of the beam and can be used to control the contrast of the

image. To get a bright field image the objective aperture is placed on the direct beam while to get a dark field image the objective aperture is placed on the diffracted beam.

The TEM imaging was used for selected samples to get an idea of grain size obtained after HPT deformation. The TEM used is a Philips CM200 microscope with a LaB_6 filament operated at 200 kV.

3.2.7 Heat Treatments of the Samples

To heat treat the samples after HPT deformation a Haake Fisons S recirculating heating oil bath was used. This facility uses a silicone oil that is stable up to 250 ^{o}C. The oil capacity of the machine is about 3 liters. The benefit of using the oil bath is that it protects the sample from oxidation at high temperature. For this research all samples were heat treated at 200 ^{o}C for two hours. The facility took about 15 minutes to reach 200 ^{o}C from room temperature. After two hours the machine was switched off, the facility then took about three hours to come down to room temperature again. To remove the oil residue the samples were left in Acetone for 10 minutes.

3.2.8 Magnetic Measurement by the Hysteresisgraph

The hysteresisgraph used during this research consists of a power amplifier (KEPCO), a data acquisition card (National Instrument PCI-6120), a connector block all connected to a PC. The KEPCO bipolar operational power amplifier (Model BOP 100-4M) can generate a 100 V and a 4 A bipolar signals. The data obtained are further processed by a LabVIEW program. A schematic diagram of this setup is demonstrated in Fig. 3.8.

The data acquisition card PCI-6120 can send out two signals and record four input signals. From the output channel the desired waveform (sinusoidal, triangular, square etc.) voltage signal U(t) is sent which is converted into electrical current by the power amplifier (KEPCO). This magnetic field magnetizes the sample. The magnetic field strength is given by the formula:

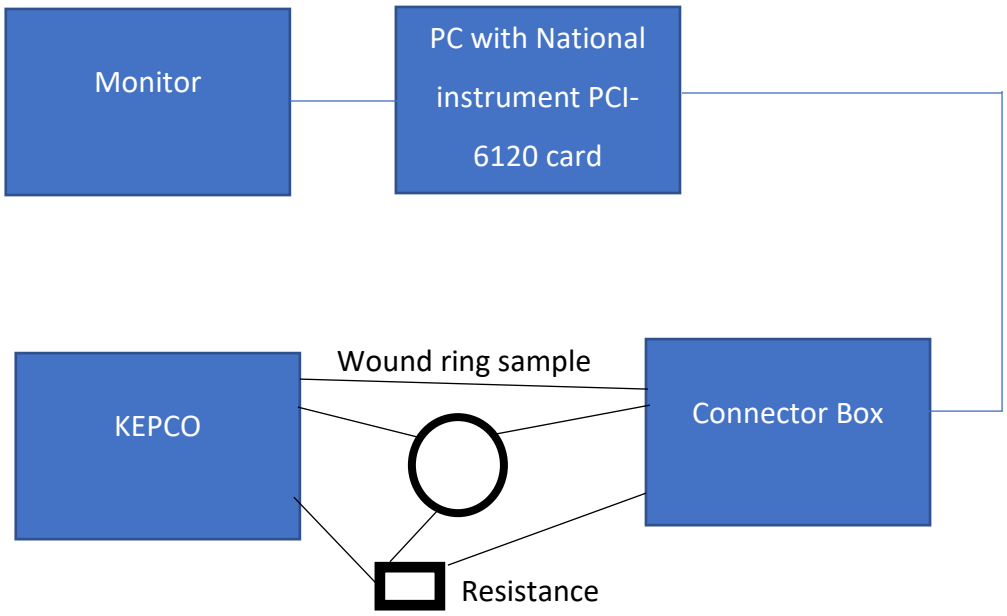

Figure 3.8: Schematic illustration of Hysteresisgraph

$$\boldsymbol{H = U_1 N_1 / R l_m} \qquad \text{Eq. 3.22}$$

where:

H: Magnetic field strength

U_1: Primary voltage

N_1: Number of primary windings

R: Shunt resistance

l_m: Mean magnetic path length

This voltage is picked up by the data acquisition card in the computer and is integrated by the LabVIEW program. Magnetic induction is calculated by:

$$\boldsymbol{B = \left(\frac{1}{N_2 A}\right) \int U_2 \, dt} \qquad \text{Eq. 3.23}$$

where:

B: Magnetic induction

N_2: Number of secondary windings

A: Cross-sectional area

U_2: Secondary voltage

From the data obtained a B vs. H hysteresis graph is plotted using the LabVIEW program. Each measurement starts off by demagnetization of the sample which is done automatically by the system and which is important so that all samples start in the same basic magnetic condition. This system can conduct frequency dependent measurements from 1 Hz to 1000 Hz.

Chapter 4: Results

4.1 DSC of Fe-Si Alloys for Determination of Heat Treatment Temperature

After HPT processing, the sample received a large number of defects including vacancies, dislocations and other free stresses. These defects negatively affect the magnetic properties of the materials under investigation. To determine the optimum heat treatment temperature where vacancies and free dislocations anneal without change of the (sub)grain size, the method of Differential Scanning Calorimetry (DSC) was used. Fig. 4.1 to Fig. 4.3 show DSC graphs of HPT-processed Fe, Fe-3wt%Si and Fe-6.5wt%Si samples.

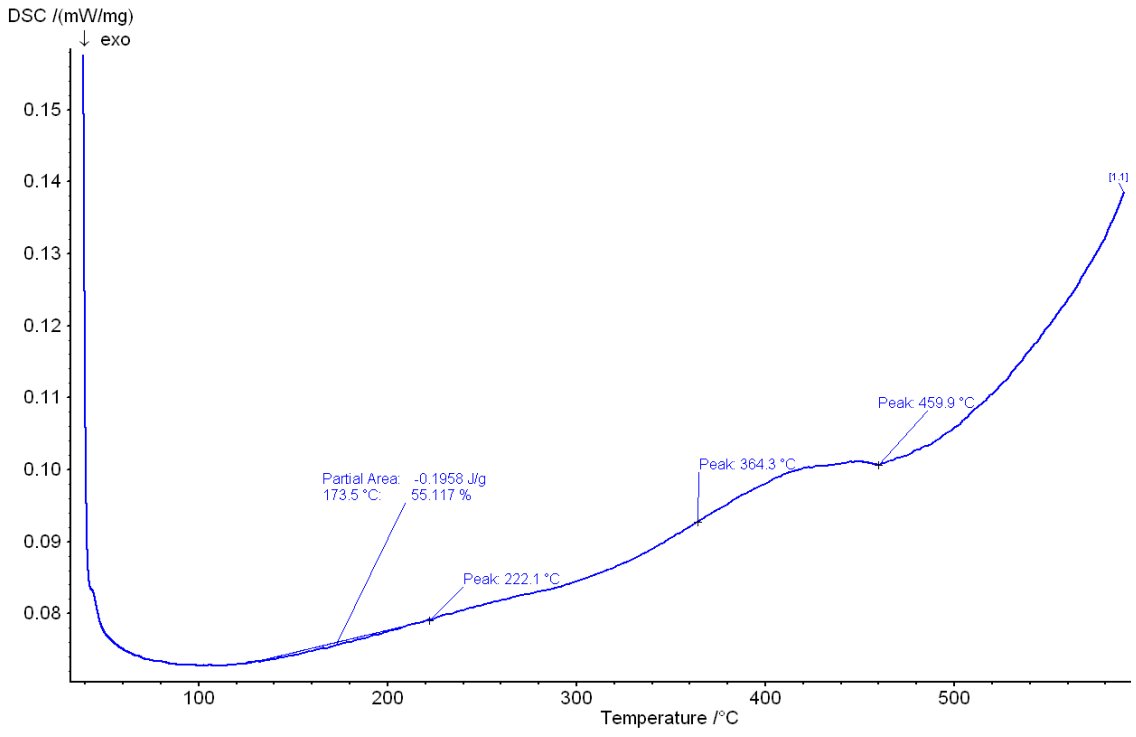

Figure 4.1: DSC graph of HPT-processed Fe sample

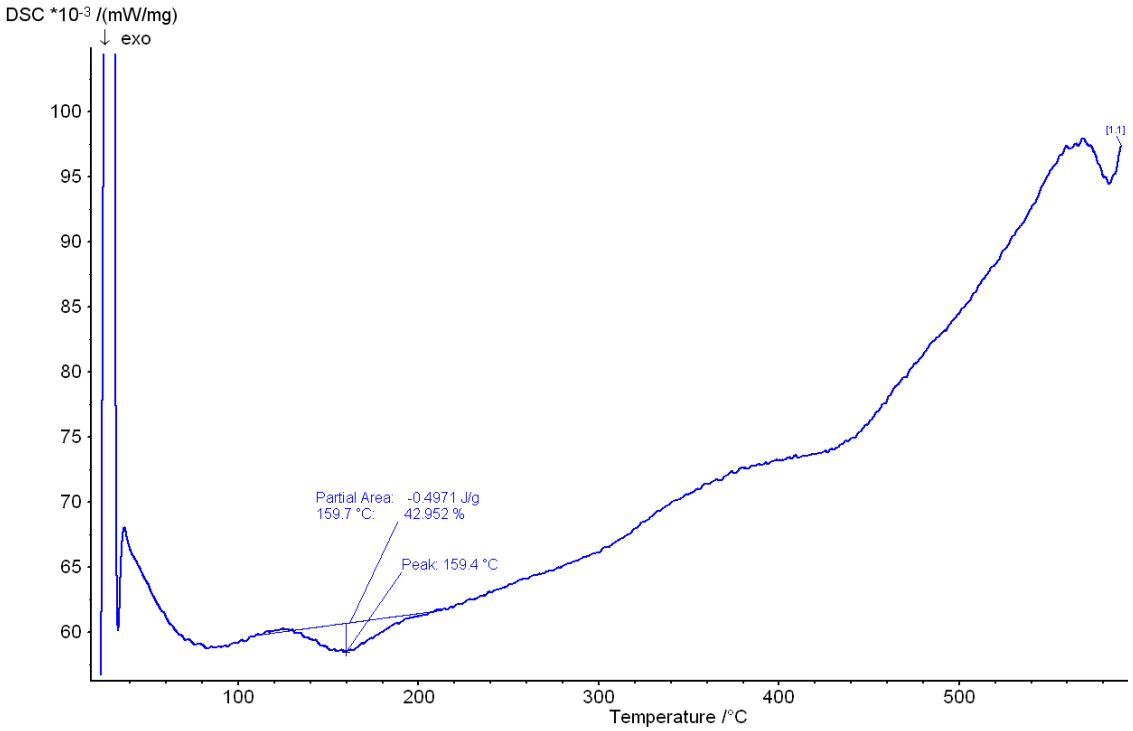

Figure 4.2: DSC graph of HPT-processed Fe-3wt%Si sample

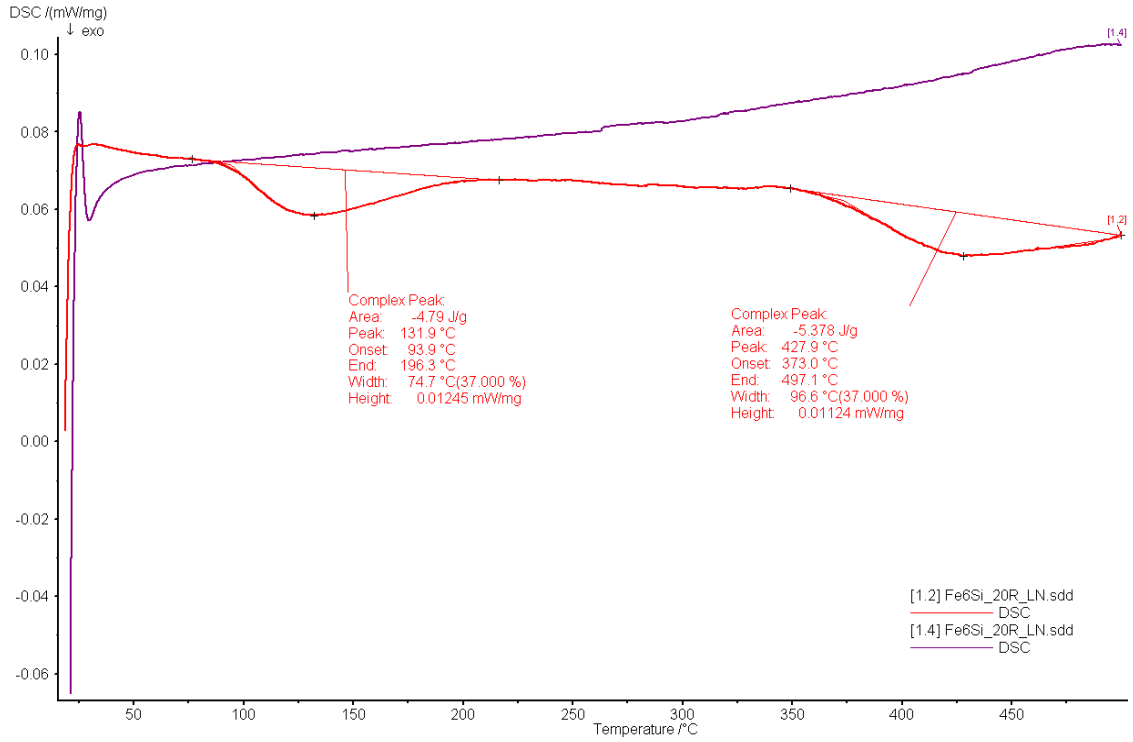

Figure 4.3: DSC graph of HPT-processed Fe-6.5wt%Si sample

All the above samples show a first exotherm that is before 200 ^{o}C. This first peak represents annihilation of defects such as vacancies (and a few free dislocations) in the sample during heating. The second peak is around 450 ^{o}C which represents annealing of dislocations which are part of deformation induced (sub)grain walls; therefore, growth of deformation-induced (sub)grain occurs. The heat treatment temperature was selected to be 200 ^{o}C to remove the defects while avoiding grain growth. The duration of heat treatment was selected to be 2 hours so that the samples have enough time to get rid of the defects. As the percentage of Si increases in the samples, the area of the first peak increases. For pure iron the energy calculated from the partial area of the first peak is 0. 1958 J/g, for Fe-3wt%Si it is 0.4971 J/g and for Fe-6.5wt%Si it is 4.79 J/g. This shows that heat treatment will have a larger effect (i.e., more defects will be annihilated upon heating) on Fe-6.5wt%Si compared to Fe and Fe-3wt%Si.

4.2 Hardness Measurements through Nanoindentation

Nanoindentation was performed on the samples as described in the Experimental section. The results of the measurements are summarized in Fig. 4.4. There are several important results that can be extracted from this graph:

- Silicon increases the hardness of iron as is already well known.
- HPT can induce hardness values being about 2 – 3 times higher than those of the annealed samples.
- Powder samples that are processed at liquid nitrogen temperature show slightly higher hardness than those that are processed at room temperature, while the bulk samples show an opposite effect.
- In Fe the heat treatment, after HPT, at 200 ^{o}C for 2 hours shows no significant annealing effect. The hardness does decrease only slightly.
- In Fe-3wt%Si and Fe-6.5wt%Si an opposite effect is observed. The heat treatment after HPT shows an anneal hardening effect. This affect is shown in other metals and alloys too such as copper alloys [168, 169].

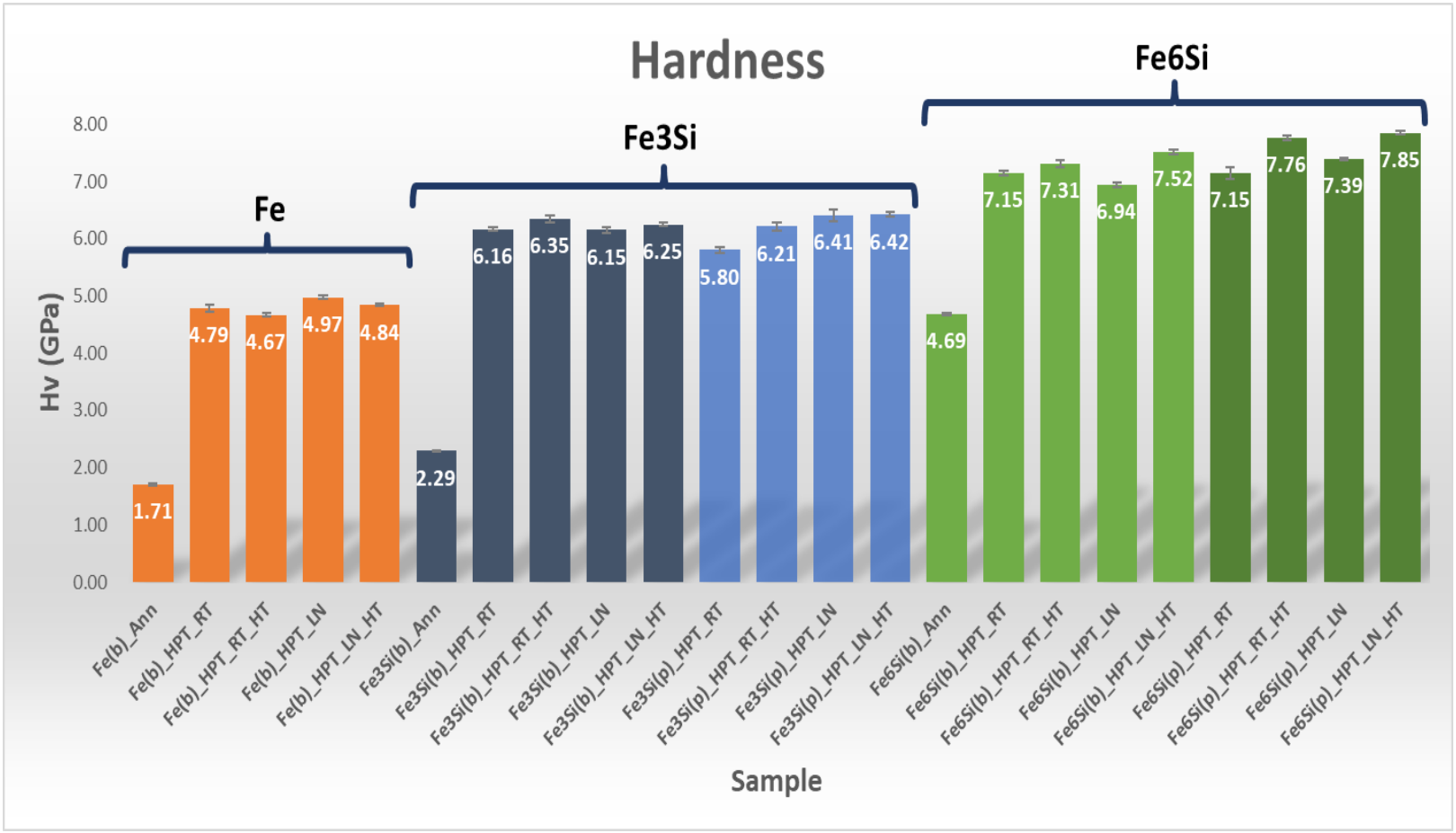

Figure 4.4: Hardness of Fe, Fe-3wt%Si and Fe-6.5wt%Si samples. “Ann” refers to annealed samples at 800 ^{o}C for 2 hours, “b” stands for bulk samples, “p” stands for Powder samples, “RT” stands for HPT-processing at room temperature, “LN” stands for HPT-processing at liquid nitrogen temperature, “HT” refers to heat treatment at 200 ^{o}C for 2 hours.

4.3 Microstructure of HPT-processed Fe-6.5wt%Si

Fig. 4.5 shows optical micrographs of HPT-deformed bulk Fe-6.5wt%Si sample while Fig. 4.6 shows the same for powder Fe-6.5wt%Si samples, both under liquid nitrogen temperature. The main difference between the two is that the powder Fe-6.5wt%Si sample show micron-sized cracks. Fe-6.5wt%Si is a very brittle alloy and a high-deformation at a low temperature causes some cracking in the sample. We can also see elongated grains along the direction of the deformation.

Transmission electron microscopy of HPT-deformed discs of bulk Fe-6.5wt%Si under liquid nitrogen, before and after heat treatment, were made on a Philips CM200 transmission electron microscope operating at 200 kV. Fig. 4.7. shows the micrographs before heat treatment while Fig. 4.8. shows the micrographs after heat treatment. It can be seen that the average grain size is around 70 nm. However some large grains are in reality just two or more separate grains close to each other which becomes evident when contrast is changed in the microscope. This shows that many grains are made up of subgrains that only differ by just few degrees in lattice orientation. There is also a small percentage of high-angle misorientation grains that are 20 - 30 nm in size as can be seen in Fig. 4.9. Such grains exhibit exchange coupling and will have some positive effect on the magnetic properties, however their number is small.

The microstructure after heat treatment looks slightly larger than the one before heat treatment. Although 200 ^{o}C is not enough to induce grain growth in iron-silicon alloys, however the presence of extremely large stress in the samples along with the defect structure should not be ignored. These stresses may have enough stored energy to have a contributory effect with the heat treatment to induce grain growth in the samples.

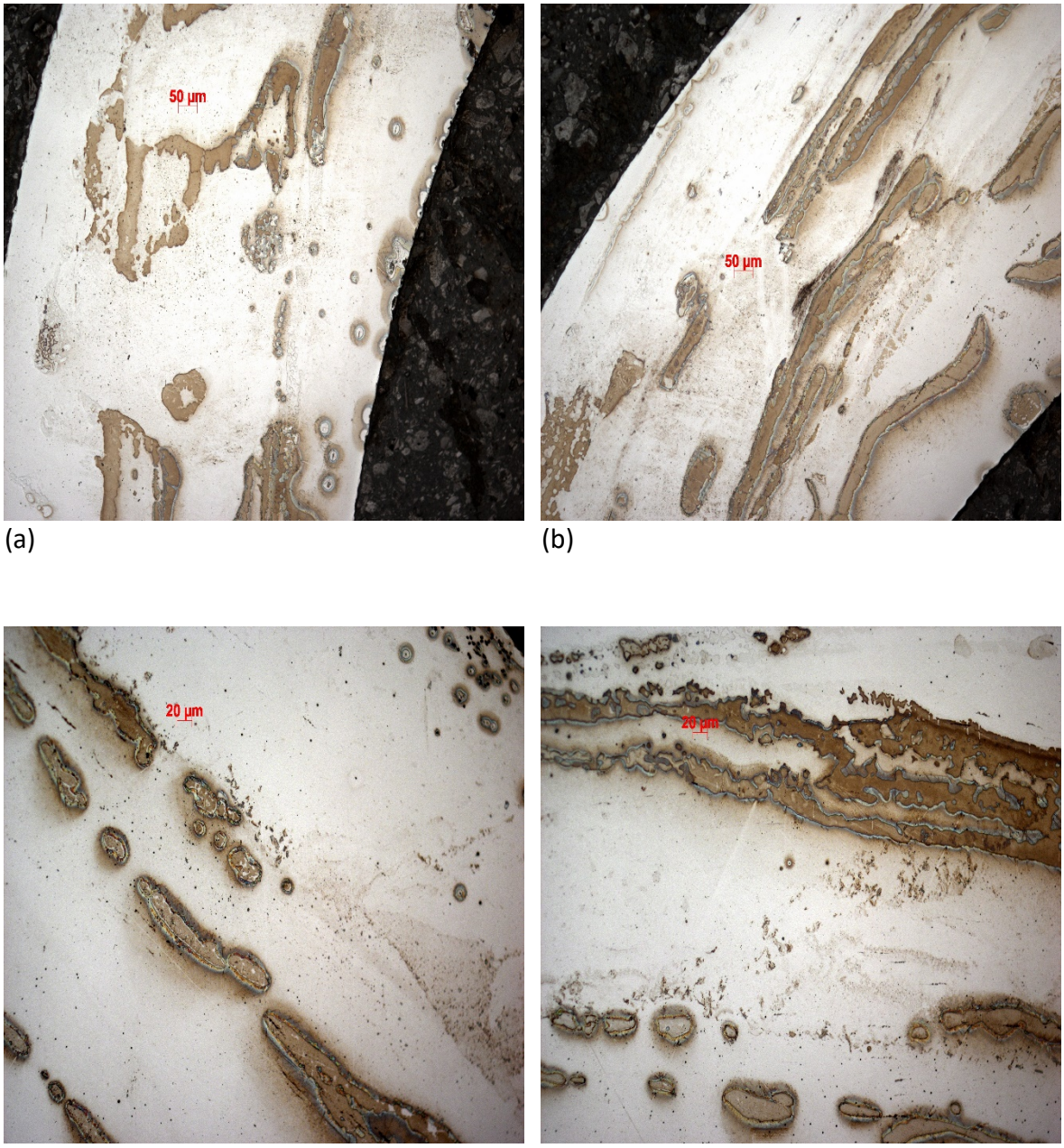

(a) (b)

(c) (d)

Figure 4.5: Optical micrographs of bulk Fe-6.5wt%Si alloy HPT-deformed under liquid nitrogen, with magnifications (a) and (b) 100x; (c) and (d) 200x

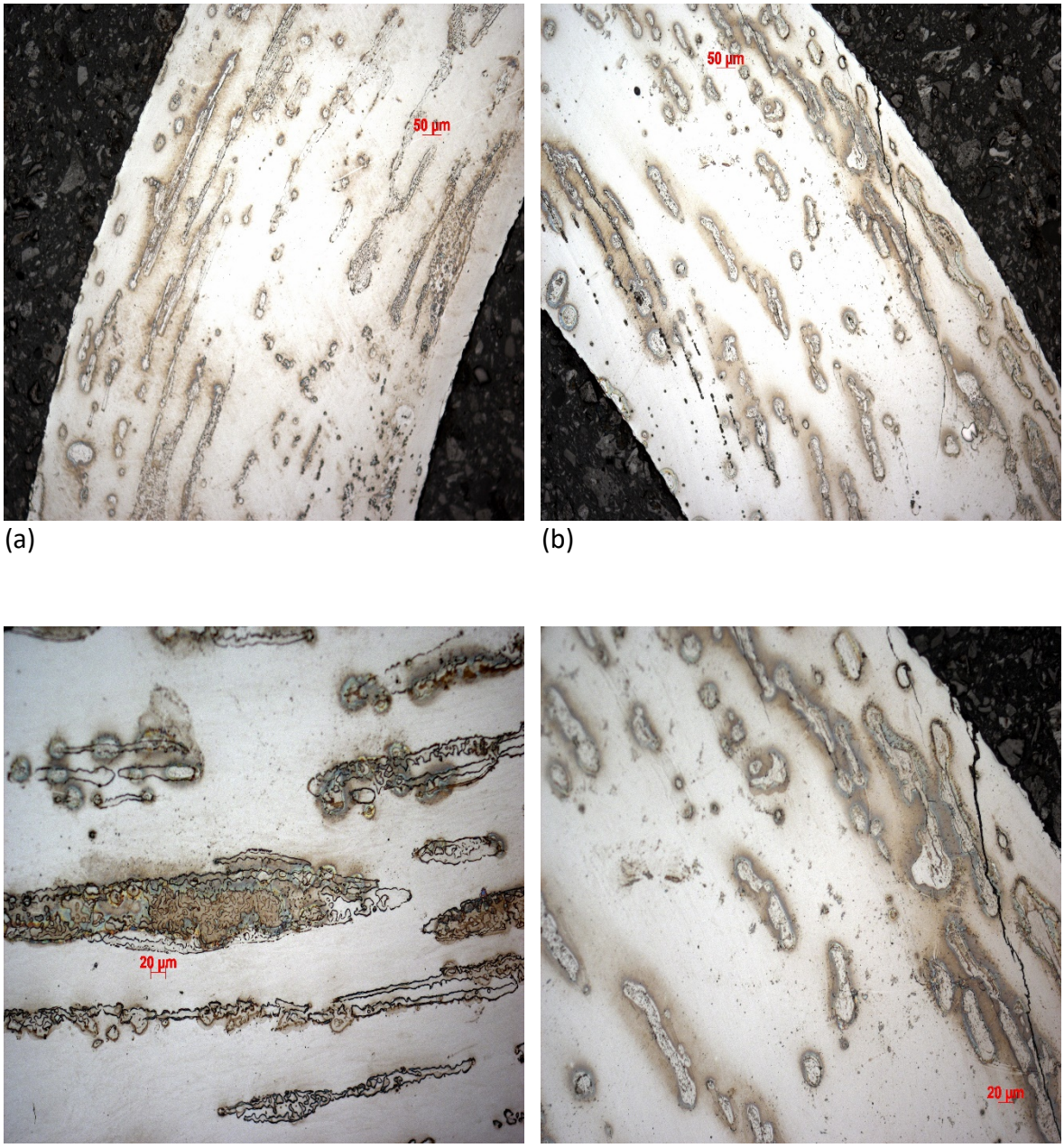

(a) (b)

(c) (d)

Figure 4.6: Optical micrographs of powder Fe-6.5wt%Si alloy HPT-deformed under liquid nitrogen, with magnifications (a) and (b) 100x; (c) and (d) 200x

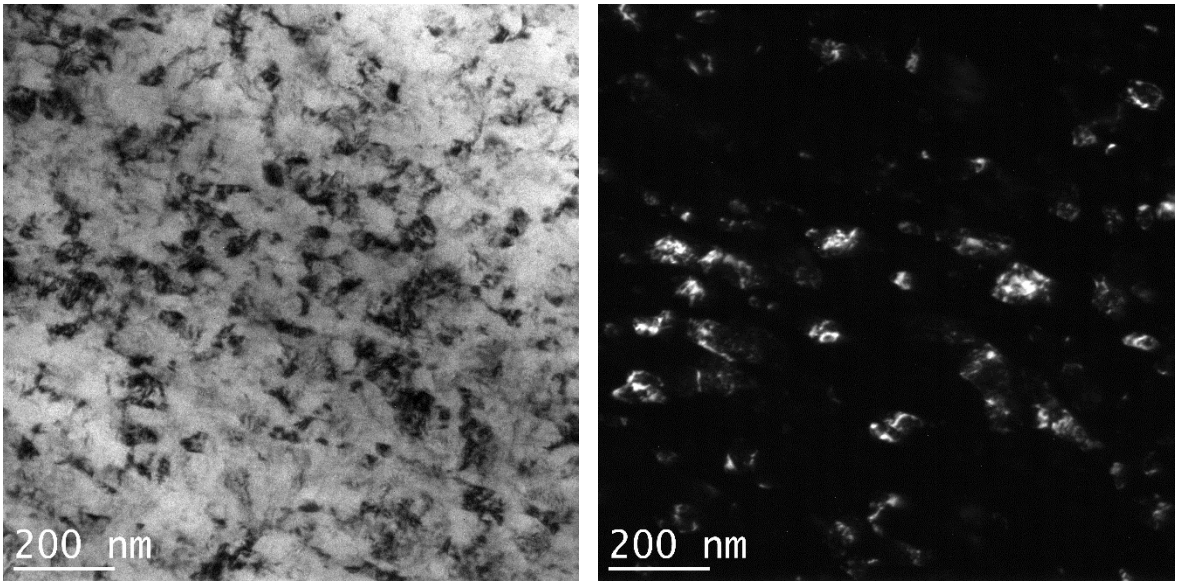

Figure 4.7: TEM micrograph of bulk Fe-6.5wt%Si alloy HPT-deformed under liquid nitrogen

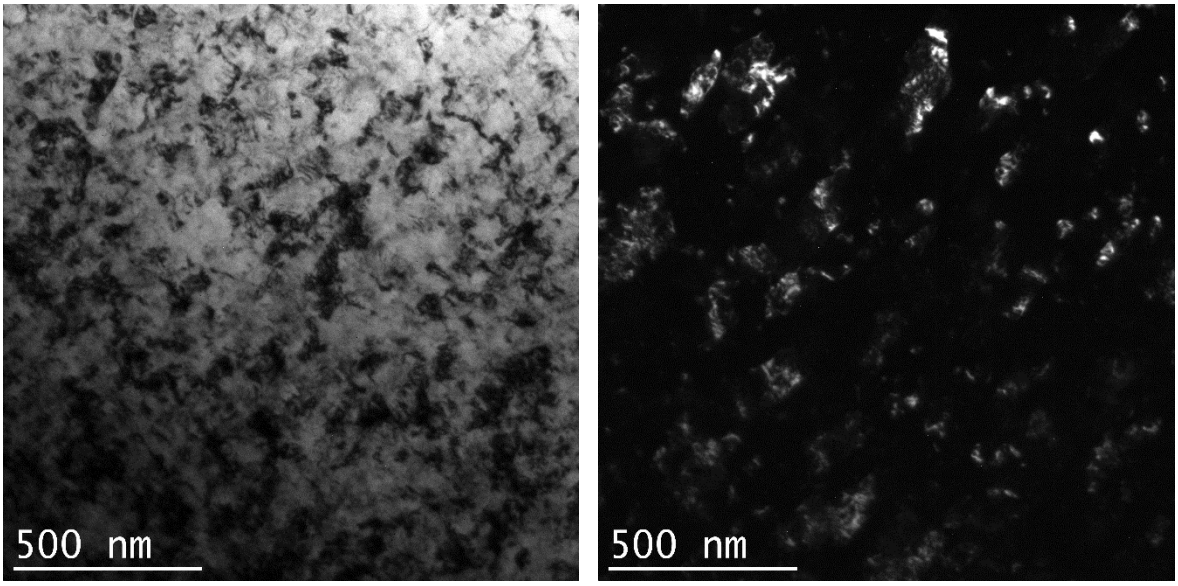

Figure 4.8: TEM micrograph of bulk Fe-6.5wt%Si alloy HPT-deformed under liquid nitrogen after heat treatment at 200 ^{o}C for 2 hours.

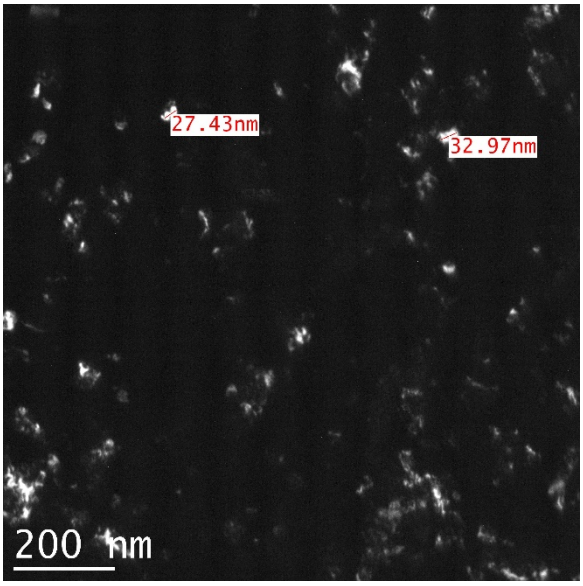

Figure 4.9: TEM micrograph of bulk Fe-6.5wt%Si alloy HPT-deformed under liquid nitrogen showing grains with 20 - 30 nm sizes.

4.4 Shear Strain & von Mises True Equivalent Strain of HPT-deformed Samples

Table 4.1 shows shear strain ($\gamma = 4\pi Nr/3h$) and von Mises true equivalent strain ($\varepsilon = \gamma/\sqrt{3}$) of the HPT-deformed samples:

Table 4.1: Shear strain γ and true accumulated strain ε of the HPT-deformed samples. N = 20 and r = 4 for all samples.

Sample	Shear strain γ	von Mises true equivalent strain ε
Fe(b)_HPT_RT	385	222
Fe(b)_HPT_LN	409	236
Fe-3wt%Si(b)_HPT_RT	500	289
Fe-3wt%Si(b)_HPT_LN	394	228
Fe-3wt%Si(p)_HPT_RT	745	430
Fe-3wt%Si(p)_HPT_LN	684	395
Fe-6.5wt%Si(b)_HPT_RT	394	228
Fe-6.5wt%Si(b)_HPT_LN	409	236
Fe-6.5wt%Si(p)_HPT_RT	508	293
Fe-6.5wt%Si(p)_HPT_LN	516	298

It should be noted that shear strain is an order of magnitude larger than what was achieved by [90]. This is primarily because of larger number of rotations (20 rotations in this research vs. 5 rotations in [90]). Generally, samples deformed under liquid nitrogen show a little higher shear strain compared to the samples that were deformed at room temperature except in the case of Fe-3wt%Si. The shear strain in powder samples is considerably higher than their bulk counterparts.

4.5 Crystallite Size measured through XLPA

Fig. 4.10 shows the graph of the crystallite (or subgrain) size of the materials under investigation as determined by the X-ray Line Profile Analysis (XLPA). The results show a higher crystallite size for pure metal, i.e., Fe, after HPT; while Fe-Si alloys show a much smaller crystallite size after HPT. As the amount of silicon increases the alloy becomes more brittle which results in a smaller crystallite size. The samples that were HPT-deformed under liquid nitrogen show a slightly smaller crystallite size compared to the one that were done at room temperature. After heat treatment the crystallite size increases in all cases. This is corroborated by the fact that the TEM imaging shows a larger grain size after heat treatment as discussed in the previous section.

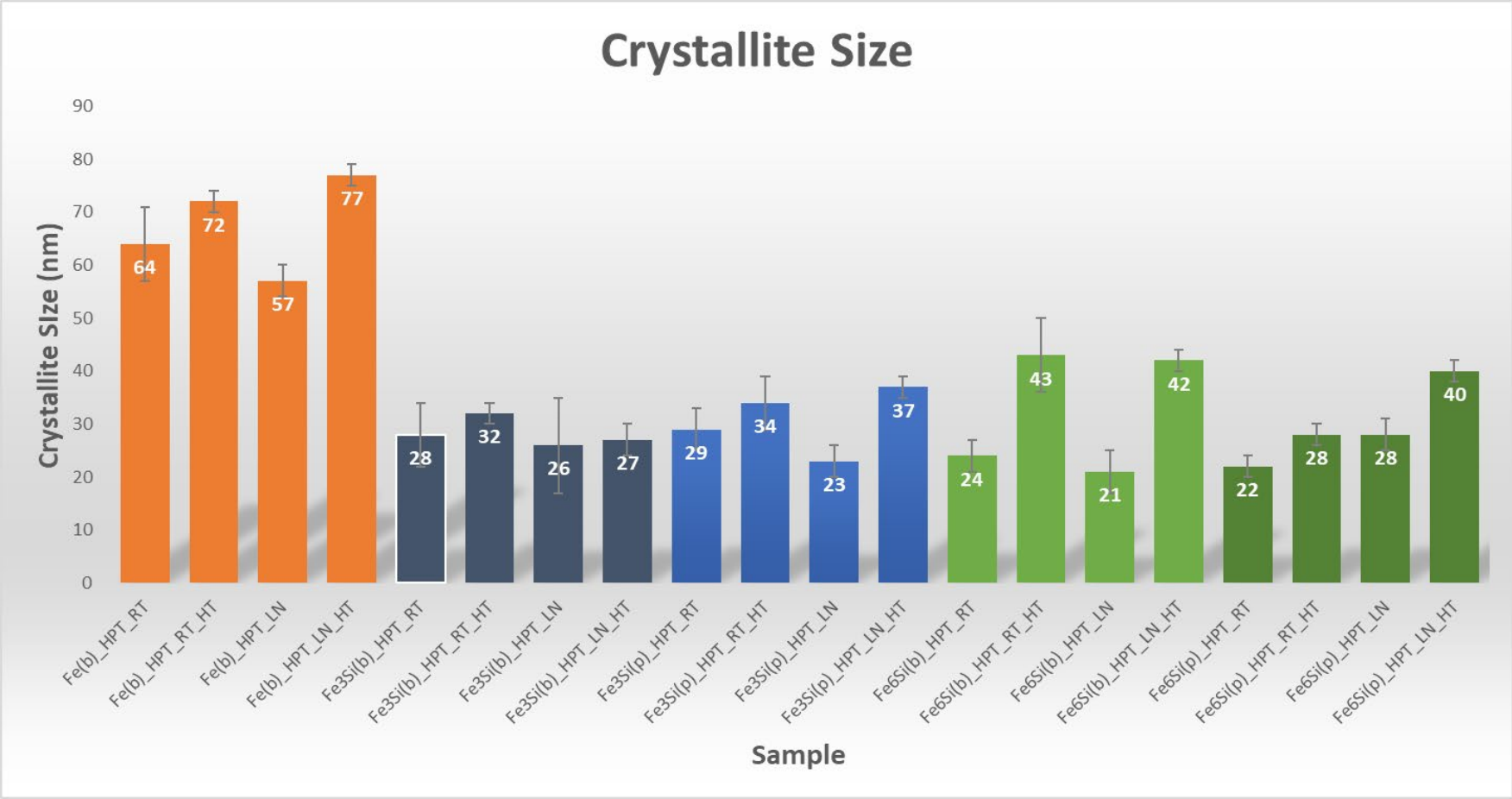

Figure 4.10: Crystallite size of Fe, Fe-3wt%Si and Fe-6.5wt%Si samples as measured by X-ray Line Profile Analysis (XLPA). “b” stands for bulk samples, “p” stands for powder samples, “RT” stands for HPT-processing at room temperature, “LN” stands for HPT-processing at liquid nitrogen temperature, “HT” refers to heat treatment at 200 ^{o}C for 2 hours.

4.6 Dislocation Density measured through XLPA

Fig 4.11 shows the graph of the dislocation density of the materials under investigation as determined by the X-ray line profile analysis (XLPA). The graph shows that pure Fe has lower dislocation density compared to Fe-Si alloys. The dislocation density increases as the amount of Si increases in the alloy. Also, the powder versions of the alloys have almost double the dislocation densities compared to their bulk counterparts. This is most likely because during the production of powders, either through atomization or through grinding of bulk materials, a large of number of defects are already present. The heat treatment after HPT decreases the dislocation density in all cases.

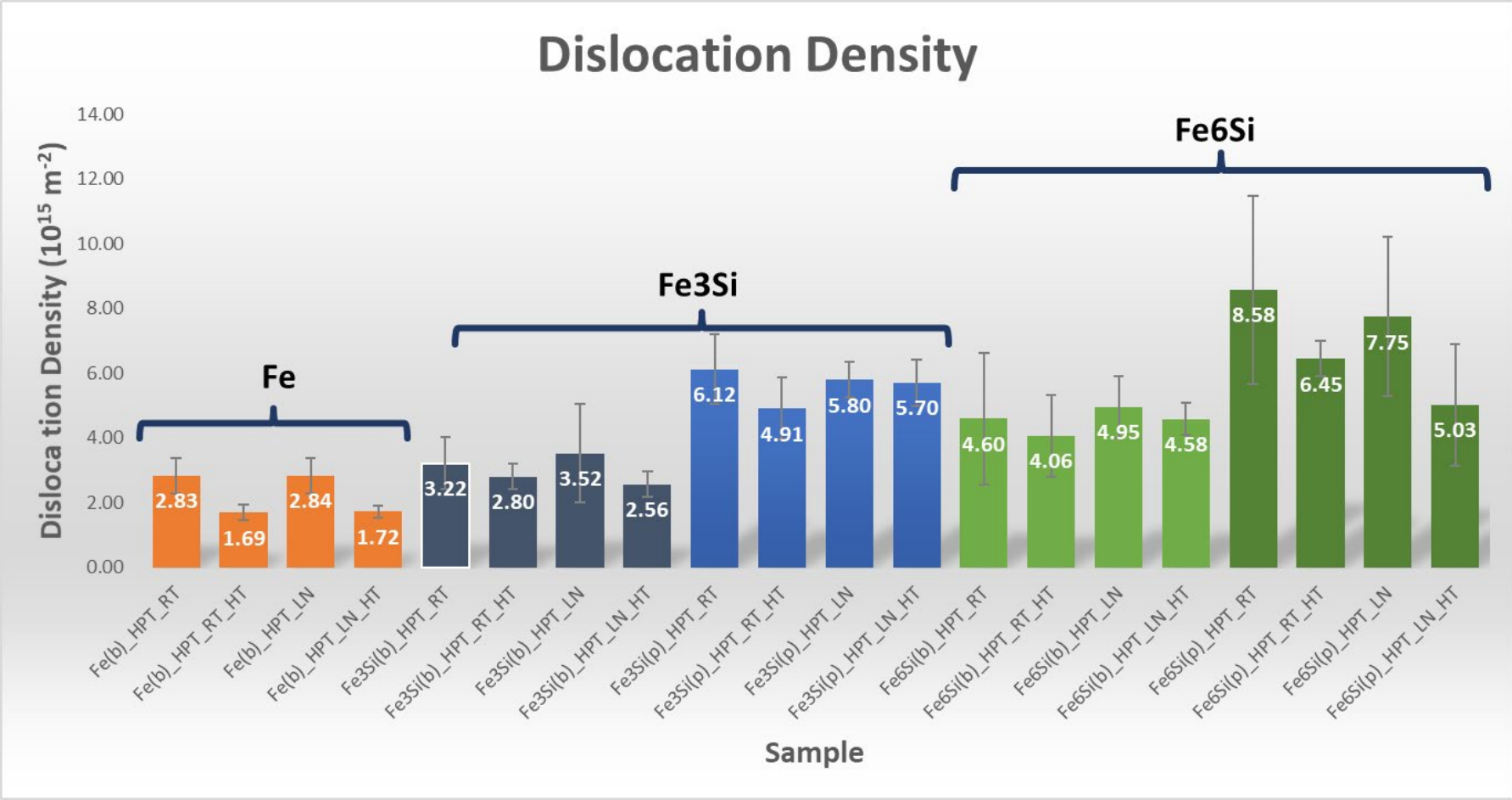

Figure 4.11: Dislocation Density of Fe, Fe-3wt%Si and Fe-6.5wt%Si samples as measured by X-ray Line Profile Analysis (XLPA). “b” stands for bulk samples, “p” stands for powder samples, “RT” stands for HPT-processing at room temperature, “LN” stands for HPT-processing at liquid nitrogen temperature, “HT” refers to heat treatment at 200 ^{o}C for 2 hours.

4.7 Dislocation Arrangement Parameter, M

Table 4.2 shows dislocation arrangement parameter M that is obtained by analyzing the strain broadening of the XRD peaks of the HPT-deformed samples through XLPA.

Table 4.2: Dislocation arrangement parameter, M of HPT-deformed samples

Sample	Dislocation Arrangement Parameter, M
Fe(b)_HPT_RT	5.5
Fe(b)_HPT_RT_HT	1.3
Fe(b)_HPT_LN	5.4
Fe(b)_HPT_LN_HT	0.5
Fe-3wt%Si(b)_HPT_RT	2.8
Fe-3wt%Si(b)_HPT_RT_HT	4.0
Fe-3wt%Si(b)_HPT_LN	0.16
Fe-3wt%Si(b)_HPT_LN_HT	0.08
Fe-3wt%Si(p)_HPT_RT	5.2
Fe-3wt%Si(p)_HPT_RT_HT	4.1
Fe-3wt%Si(p)_HPT_LN	0.3
Fe-3wt%Si(p)_HPT_LN_HT	5.8
Fe-6.5wt%Si(b)_HPT_RT	11
Fe-6.5wt%Si(b)_HPT_RT_HT	0.4
Fe-6.5wt%Si(b)_HPT_LN	3.2
Fe-6.5wt%Si(b)_HPT_LN_HT	1.2
Fe-6.5wt%Si(p)_HPT_RT	6.1
Fe-6.5wt%Si(p)_HPT_RT_HT	4.2
Fe-6.5wt%Si(p)_HPT_LN	1.2
Fe-6.5wt%Si(p)_HPT_LN_HT	1.0

The relative accuracy of determination of M values is between 10-20 %, depending on the quality of profiles measured. If M is close to 1 then this represents screening of strain field of neighboring dislocations. If M is much less than 1 then this represents dislocation dipoles. For more details concerning the M-factor, see Section 3.2.4. In any case, there exists a linear relationship to the dislocation arrangement/interaction parameter α [170] which will be used within this thesis, see Section 5.3.2.

4.8 Magnetic Hysteresis Measurements of Fe-Si Alloys

Magnetic hysteresis loops were measured on a hysteresisgraph as detailed in chapter 3. Samples with their geometric dimensions and parameters used for hysteresis measurements are provided in Table 4.3.

Table 4.3: Dimensions and parameters of samples used for hysteresis measurements

Sample	Cross-Sectional Area, A (m2)	Magnetic Path Length, l_m (m)	Primary Turns, N_1	Secondary Turns, N_2
Fe(b)_Annealed	13.00×10^{-7}	21.865×10^{-3}	85	70
Fe(b)_HPT_RT	12.88×10^{-7}	22.085×10^{-3}	97	55
Fe(b)_HPT_RT_HT	3.74×10^{-7}	21.881×10^{-3}	66	66
Fe(b)_HPT_LN	8.27×10^{-7}	22.117×10^{-3}	92	55
Fe(b)_HPT_LN_HT	8.11×10^{-7}	21.865×10^{-3}	93	47
Fe-3wt%Si(b)_Annealed	12.86×10^{-7}	22.070×10^{-3}	60	60
Fe-3wt%Si(b)_HPT_RT	6.66×10^{-7}	21.520×10^{-3}	71	48
Fe-3wt%Si(b)_HPT_RT_HT	6.67×10^{-7}	21.646×10^{-3}	77	47
Fe-3wt%Si(b)_HPT_LN	7.17×10^{-7}	21.928×10^{-3}	73	49
Fe-3wt%Si(b)_HPT_LN_HT	9.66×10^{-7}	21.520×10^{-3}	76	48
Fe-3wt%Si(p)_HPT_RT	8.64×10^{-7}	21.928×10^{-3}	77	47
Fe-3wt%Si(p)_HPT_RT_HT	3.52×10^{-7}	20.243×10^{-3}	64	66
Fe-3wt%Si(p)_HPT_LN	3.17×10^{-7}	20.205×10^{-3}	64	65
Fe-3wt%Si(p)_HPT_LN_HT	6.66×10^{-7}	21.614×10^{-3}	78	48
Fe-6.5wt%Si(b)_Annealed	12.73×10^{-7}	20.386×10^{-3}	49	49
Fe-6.5wt%Si(b)_HPT_RT	4.62×10^{-7}	20.494×10^{-3}	101	78
Fe-6.5wt%Si(b)_HPT_RT_HT	7.02×10^{-7}	20.343×10^{-3}	71	71
Fe-6.5wt%Si(b)_HPT_LN	8.20×10^{-7}	20.365×10^{-3}	68	68
Fe-6.5wt%Si(b)_HPT_LN_HT	7.08×10^{-7}	20.975×10^{-3}	71	76
Fe-6.5wt%Si(p)_HPT_RT	5.83×10^{-7}	20.978×10^{-3}	84	75
Fe-6.5wt%Si(p)_HPT_RT_HT	5.67×10^{-7}	20.092×10^{-3}	63	70
Fe-6.5wt%Si(p)_HPT_LN	7.87×10^{-7}	21.184×10^{-3}	124	73
Fe-6.5wt%Si(p)_HPT_LN_HT	6.73×10^{-7}	20.086×10^{-3}	61	61

4.8.1 Hysteresis Measurements of HPT-Deformed Bulk Fe

Fig 4.12 shows hysteresis curves of annealed and HPT deformed and heat-treated pure bulk Iron samples. Fig 4.13 and show coercivity vs frequency graphs of HPT-deformed bulk Iron samples and are compared with annealed bulk Iron samples. The frequencies measured in the hysteresis graphs are f = 5, 10, 20, 50, 100, 150 and 200 Hz. In the legend the frequencies are always given in this order from top to bottom. For Fe-6.5wt%Si samples f = 5, 10, 20, 50, 100 and 200 Hz were tested. In Fig. 4.13 the HPT deformation is done at room temperature while in Fig. 4.14 the HPT deformation is done at liquid nitrogen temperature. The results show that HPT deformation (blue line) substantially increases the coercivity of pure Iron. This is because defects induced by deformation hinder the domain wall movement which, in turn, deteriorate the soft magnetic properties of the material. The heat treatment substantially lowers the coercivity of the HPT-deformed sample as shown in Fig. 4.13. This is because a large number of defects are annealed out of the sample. A comparison of the coercivities of heat-treated HPT deformed sample (orange line) and annealed sample (black line) shows that at low frequencies annealed Fe has lower coercivity but at a certain point the HPT-deformed heat-treated sample shows a lower coercivity. This is because at higher frequencies the classical Eddy current losses are higher in annealed sample because it has higher conductivity. The HPT deformation increases the resistivity of the sample which reduces the Eddy current losses, thereby decreasing the coercivity of the sample.

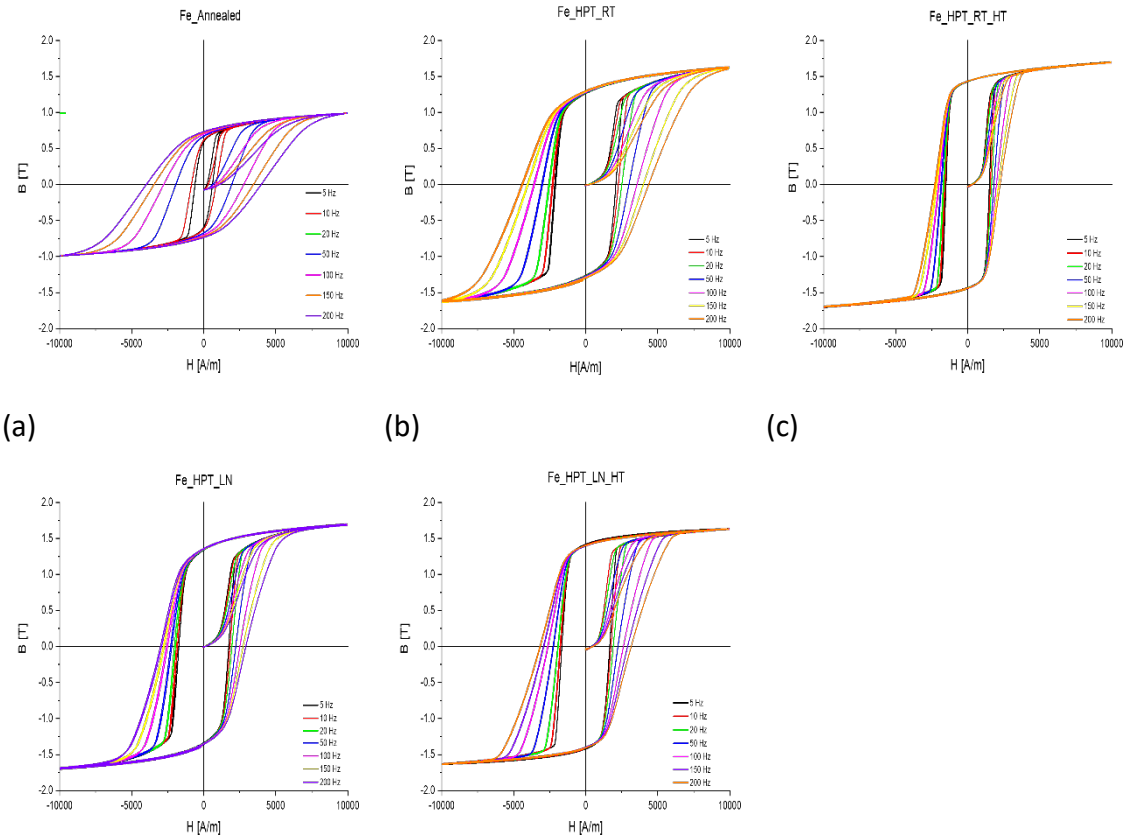

Figure 4.12: The frequency-dependent hysteresis loops of HPT-deformed pure Fe (a) undeformed (annealed); (b) deformed at room temperature; (c) deformed at room temperature followed by heat treatment; (d) deformed at liquid nitrogen temperature; (e) deformed at liquid nitrogen temperature followed by heat treatment.

The HPT deformation of bulk Iron under liquid nitrogen as shown in Fig. 4.14 show very little difference between HPT-deformed sample (blue line) and heat-treated HPT-deformed sample (orange line). There is a substantial difference in coercivity values when deformation is done at room temperature and when it is done at liquid nitrogen temperature. At liquid nitrogen temperature the deformation is higher which increases the defects and increases the resistivity of the samples [90, 171]. This further lowers the coercivity of the sample. The heat treatment in this case has a slightly negative effect as the heat treatment lowers the resistivity a bit and increases the coercivity correspondingly. These results show that if pure bulk Iron is to be used at higher frequencies it is better to use a heat-treated HPT-deformed sample. For lower frequencies an annealed sample is a better choice.

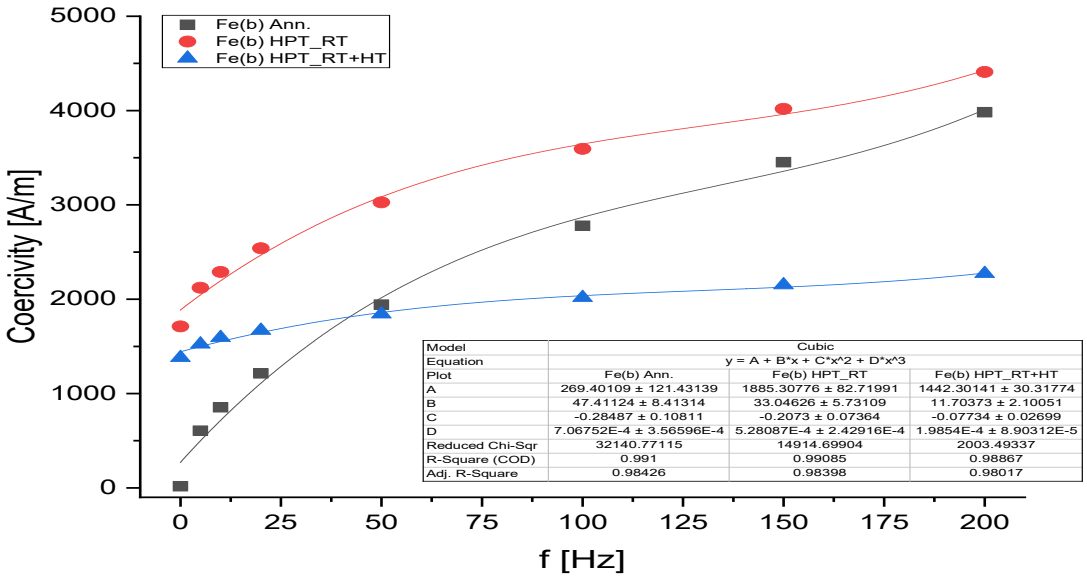

Model	Cubic		
Equation	y = A + B*x + C*x^2 + D*x^3		
Plot	Fe(b) Ann.	Fe(b) HPT_RT	Fe(b) HPT_RT+HT
A	269.40109 ± 121.43139	1885.30776 ± 82.71991	1442.30141 ± 30.31774
B	47.41124 ± 8.41314	33.04626 ± 5.73109	11.70373 ± 2.10051
C	-0.28487 ± 0.10811	-0.2073 ± 0.07364	-0.07734 ± 0.02699
D	7.06752E-4 ± 3.56596E-4	5.28087E-4 ± 2.42916E-4	1.9854E-4 ± 8.90312E-5
Reduced Chi-Sqr	32140.77115	14914.69904	2003.49337
R-Square (COD)	0.991	0.99085	0.98867
Adj. R-Square	0.98426	0.98398	0.98017

Figure 4.13: Comparison of Coercivity (A/m) vs Frequency (Hz) of Annealed and HPT-deformed bulk Iron samples. HPT deformation is done at room temperature.

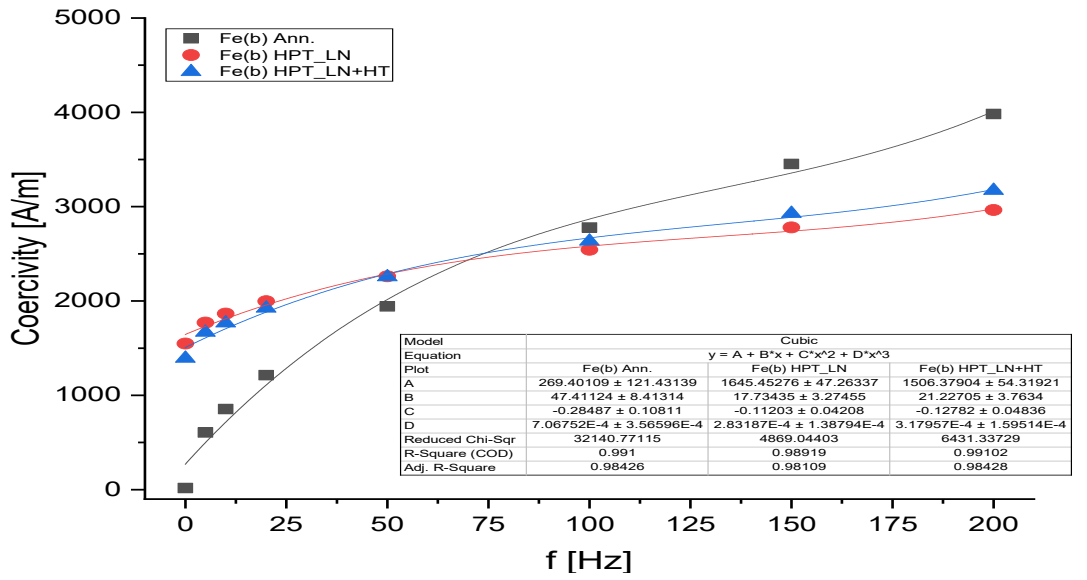

Model	Cubic		
Equation	y = A + B*x + C*x^2 + D*x^3		
Plot	Fe(b) Ann.	Fe(b) HPT_LN	Fe(b) HPT_LN+HT
A	269.40109 ± 121.43139	1645.45276 ± 47.26337	1506.37904 ± 54.31921
B	47.41124 ± 8.41314	17.73435 ± 3.27455	21.22705 ± 3.7634
C	-0.28487 ± 0.10811	-0.11203 ± 0.04208	-0.12782 ± 0.04836
D	7.06752E-4 ± 3.56596E-4	2.83187E-4 ± 1.38794E-4	3.17957E-4 ± 1.59514E-4
Reduced Chi-Sqr	32140.77115	4869.04403	6431.33729
R-Square (COD)	0.991	0.98919	0.99102
Adj. R-Square	0.98426	0.98109	0.98428

Figure 4.14: Comparison of Coercivity (A/m) vs Frequency (Hz) of Annealed and HPT-deformed bulk Iron samples. HPT deformation is done at liquid nitrogen temperature.

4.8.2 Hysteresis Measurements of HPT-Deformed Bulk Fe-3wt%Si

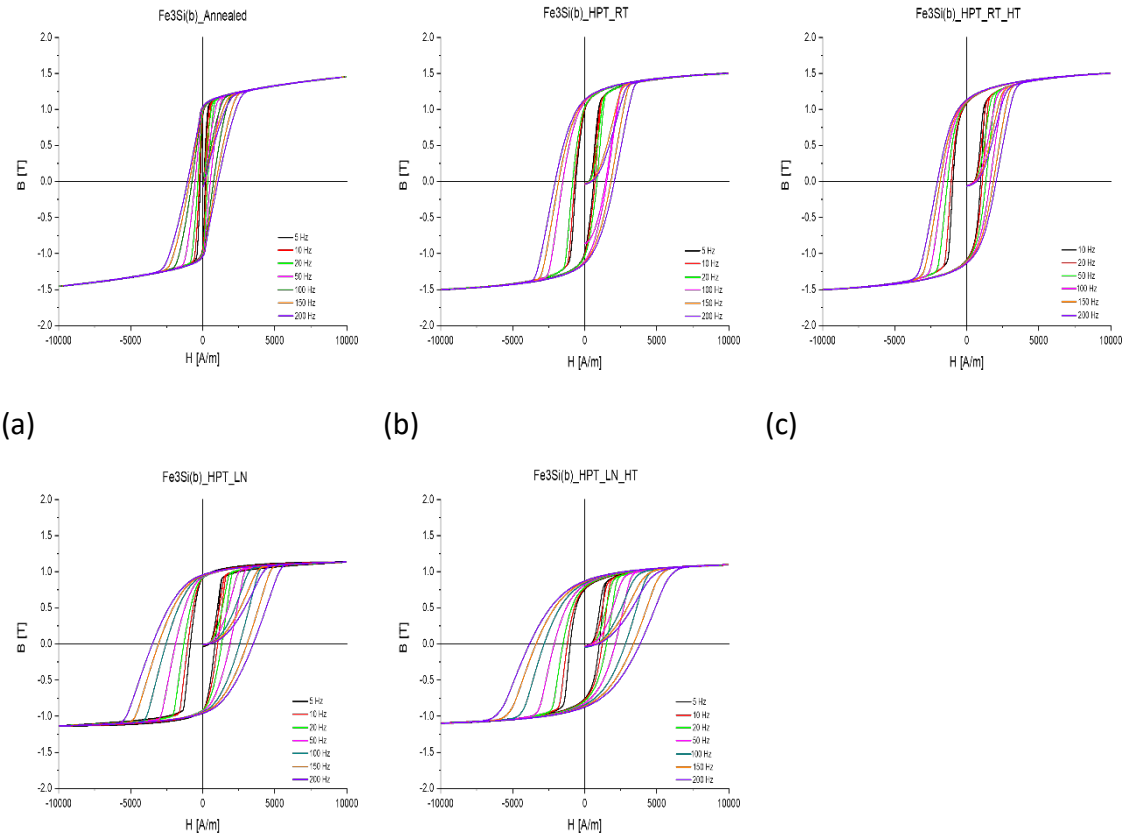

Figure 4.15: The frequency-dependent hysteresis loops of HPT-deformed Bulk Fe-3wt%Si (a) undeformed (annealed); (b) deformed at room temperature; (c) deformed at room temperature followed by heat treatment; (d) deformed at liquid nitrogen temperature; (e) deformed at liquid nitrogen temperature followed by heat treatment.

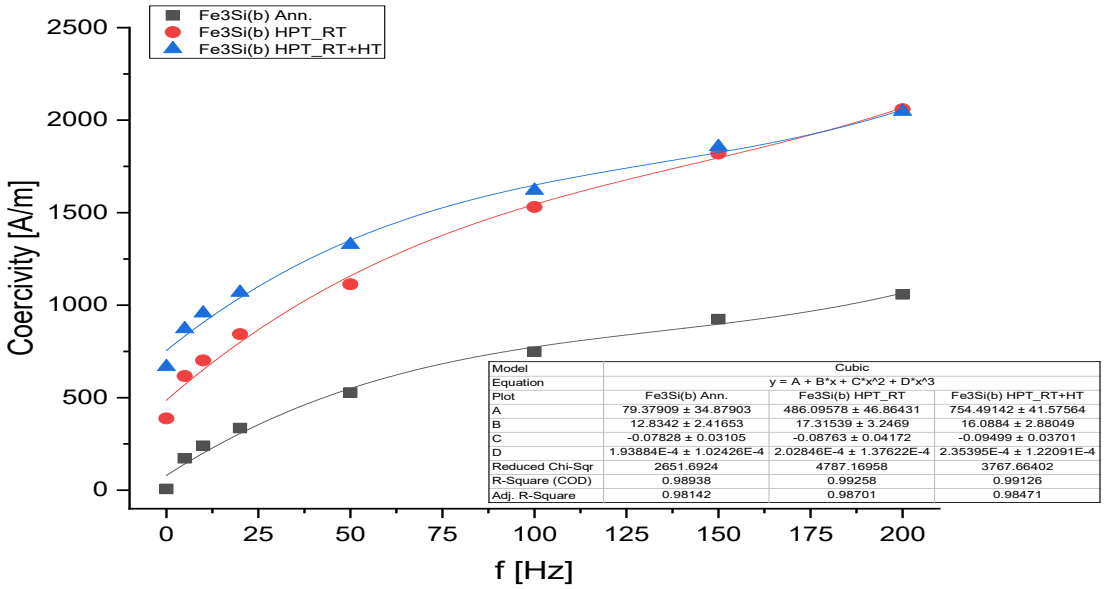

Model	Cubic		
Equation	y = A + B*x + C*x^2 + D*x^3		
Plot	Fe3Si(b) Ann.	Fe3Si(b) HPT_RT	Fe3Si(b) HPT_RT+HT
A	79.37909 ± 34.87903	486.09578 ± 46.86431	754.49142 ± 41.57564
B	12.8342 ± 2.41653	17.31539 ± 3.2469	16.0884 ± 2.88049
C	-0.07828 ± 0.03105	-0.08763 ± 0.04172	-0.09499 ± 0.03701
D	1.93884E-4 ± 1.02426E-4	2.02846E-4 ± 1.37622E-4	2.35395E-4 ± 1.22091E-4
Reduced Chi-Sqr	2651.6924	4787.16958	3767.66402
R-Square (COD)	0.98938	0.99258	0.99126
Adj. R-Square	0.98142	0.98701	0.98471

Figure 4.16: Comparison of Coercivity (A/m) vs Frequency (Hz) of Annealed and HPT-deformed bulk Fe-3wt%Si samples. HPT deformation is done at room temperature.

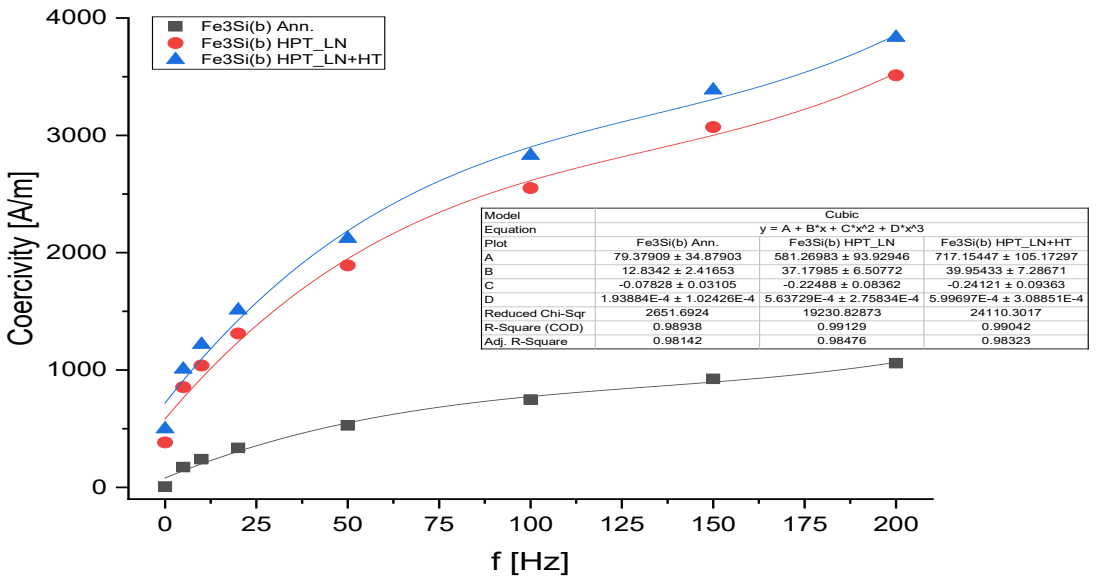

Model	Cubic		
Equation	y = A + B*x + C*x^2 + D*x^3		
Plot	Fe3Si(b) Ann.	Fe3Si(b) HPT_LN	Fe3Si(b) HPT_LN+HT
A	79.37909 ± 34.87903	581.26983 ± 93.92946	717.15447 ± 105.17297
B	12.8342 ± 2.41653	37.17985 ± 6.50772	39.95433 ± 7.28671
C	-0.07828 ± 0.03105	-0.22488 ± 0.08362	-0.24121 ± 0.09363
D	1.93884E-4 ± 1.02426E-4	5.63729E-4 ± 2.75834E-4	5.99697E-4 ± 3.08851E-4
Reduced Chi-Sqr	2651.6924	19230.82873	24110.3017
R-Square (COD)	0.98938	0.99129	0.99042
Adj. R-Square	0.98142	0.98476	0.98323

Figure 4.17: Comparison of Coercivity (A/m) vs Frequency (Hz) of Annealed and HPT-deformed bulk Fe-3wt%Si samples. HPT deformation is done at liquid nitrogen temperature.

Fig. 4.15 shows hysteresis curves of annealed, HPT-deformed and HPT-deformed plus heat-treated bulk Fe-3wt%Si samples. Fig. 4.16 and Fig. 4.17 show coercivity vs frequency graphs of HPT-deformed bulk Fe-3wt%Si samples and are compared with annealed bulk Fe-3wt%Si samples. The graphs show a sharp rise in the coercivity of Fe-3wt%Si samples after HPT deformation. Results show that coercivity rises slightly after heat treatment. HPT-deformation under liquid nitrogen also increases the coercivity compared to room temperature deformation.

4.8.3 Hysteresis Measurements of HPT-Deformed Powder Fe-3wt%Si

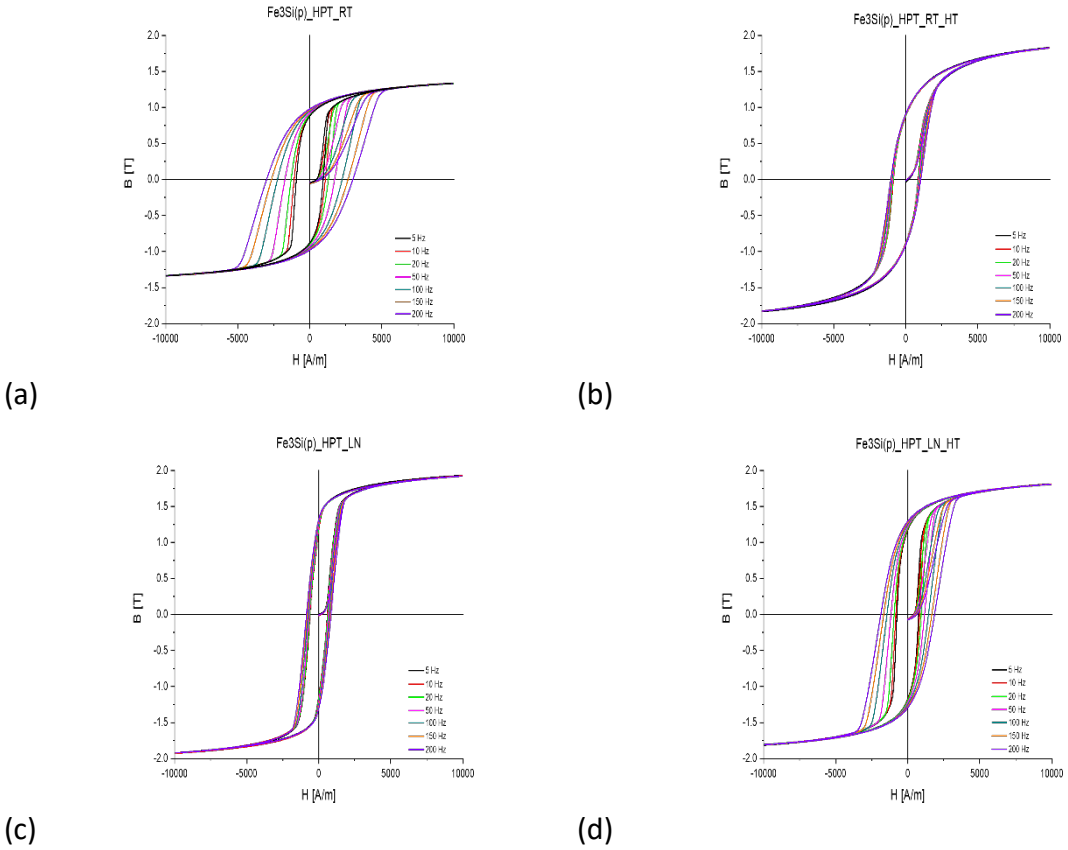

Figure 4.18: The frequency-dependent hysteresis loops of HPT-deformed Powder Fe-3wt%Si (a) deformed at room temperature; (b) deformed at room temperature followed by heat treatment; (c) deformed at liquid nitrogen temperature; (d) deformed at liquid nitrogen temperature followed by heat treatment.

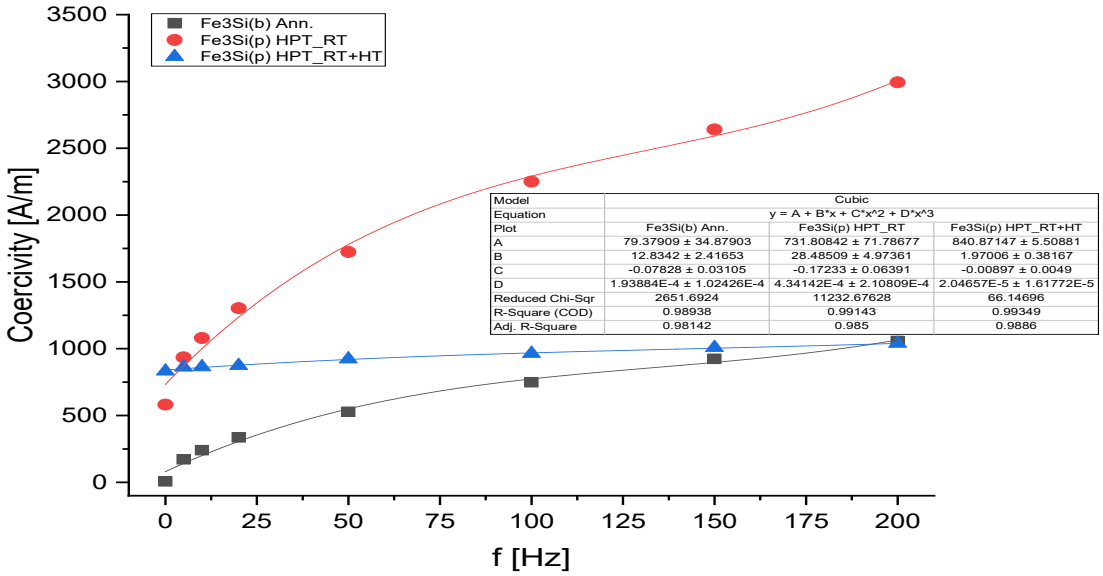

Model	Cubic		
Equation	y = A + B*x + C*x^2 + D*x^3		
Plot	Fe3Si(b) Ann.	Fe3Si(p) HPT_RT	Fe3Si(p) HPT_RT+HT
A	79.37909 ± 34.87903	731.80842 ± 71.78677	840.87147 ± 5.50881
B	12.8342 ± 2.41653	28.48509 ± 4.97361	1.97006 ± 0.38167
C	-0.07828 ± 0.03105	-0.17233 ± 0.06391	-0.00897 ± 0.0049
D	1.93884E-4 ± 1.02426E-4	4.34142E-4 ± 2.10809E-4	2.04657E-5 ± 1.61772E-5
Reduced Chi-Sqr	2651.6924	11232.67628	66.14696
R-Square (COD)	0.98938	0.99143	0.99349
Adj. R-Square	0.98142	0.985	0.9886

Figure 4.19: Comparison of Coercivity (A/m) vs Frequency (Hz) of Annealed and HPT-deformed powder Fe-3wt%Si samples. HPT deformation is done at room temperature.

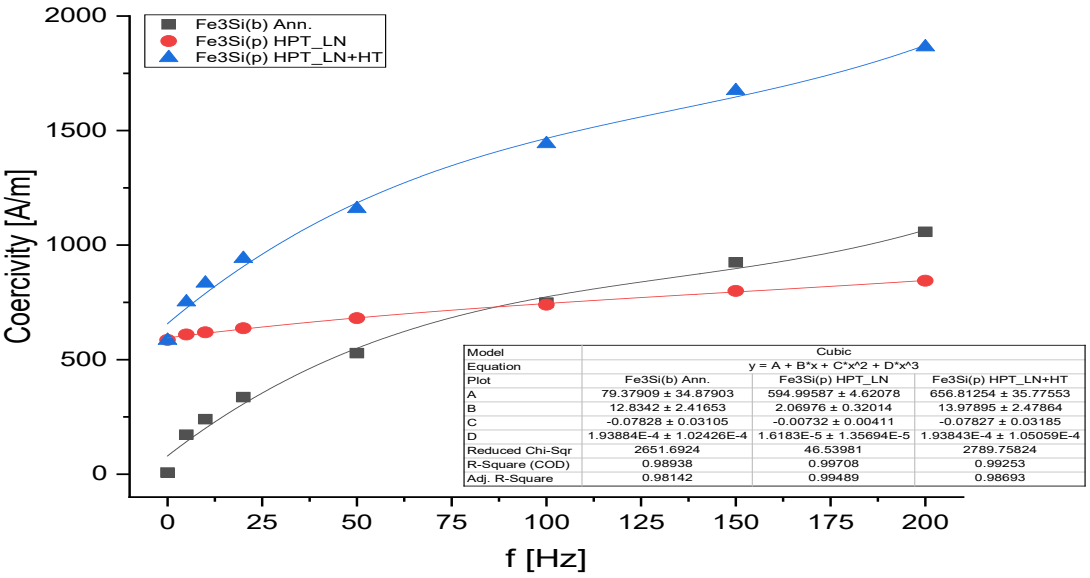

Model	Cubic		
Equation	y = A + B*x + C*x^2 + D*x^3		
Plot	Fe3Si(b) Ann.	Fe3Si(p) HPT_LN	Fe3Si(p) HPT_LN+HT
A	79.37909 ± 34.87903	594.99587 ± 4.62078	656.81254 ± 35.77553
B	12.8342 ± 2.41653	2.06976 ± 0.32014	13.97895 ± 2.47864
C	-0.07828 ± 0.03105	-0.00732 ± 0.00411	-0.07827 ± 0.03185
D	1.93884E-4 ± 1.02426E-4	1.6183E-5 ± 1.35694E-5	1.93843E-4 ± 1.05059E-4
Reduced Chi-Sqr	2651.6924	46.53981	2789.75824
R-Square (COD)	0.98938	0.99708	0.99253
Adj. R-Square	0.98142	0.99489	0.98693

Figure 4.20: Comparison of Coercivity (A/m) vs Frequency (Hz) of Annealed and HPT-deformed powder Fe-3wt%Si samples. HPT deformation is done at liquid nitrogen temperature.

Fig. 4.18 shows hysteresis curves of annealed and HPT deformed and heat-treated powder Fe-3wt%Si samples. The graph in Fig. 4.19 shows a room temperature HPT-deformed sample (blue line) and a heat-treated sample (orange line) compared to an annealed bulk Fe-3wt%Si sample. Again, the coercivity rises sharply with HPT deformation. After heat treatment the coercivity decreases drastically but it is still above the coercivity of annealed sample.

In case of the samples are deformed under liquid nitrogen a reverse behavior is evident as shown in Fig. 4.20. After heat treatment a rise in coercivity is observed.

4.8.4 Hysteresis Measurements of HPT-Deformed Bulk Fe-6.5wt%Si

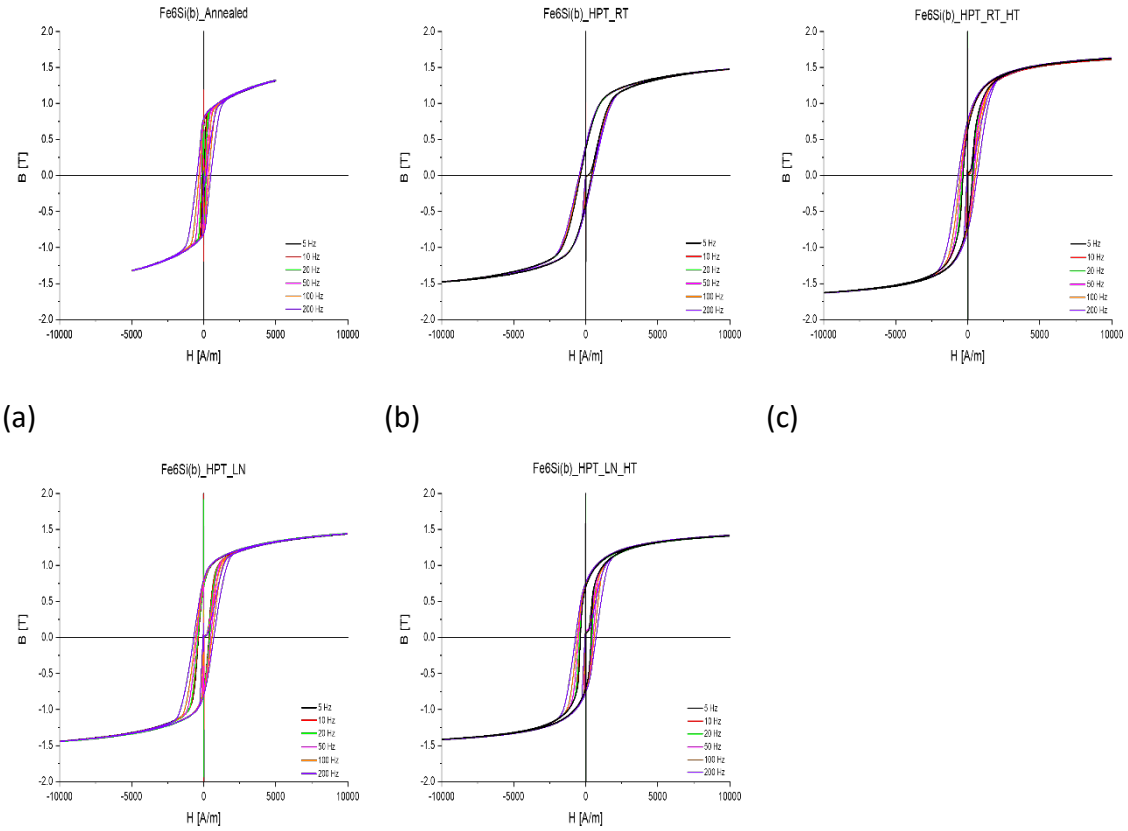

(a) (b) (c)

(d) (e)

Figure 4.21: The frequency-dependent hysteresis loops of HPT-deformed Bulk Fe-6.5wt%Si (a) undeformed (annealed); (b) deformed at room temperature; (c) deformed at room temperature followed by heat treatment; (d) deformed at liquid nitrogen temperature; (e) deformed at liquid nitrogen temperature followed by heat treatment.

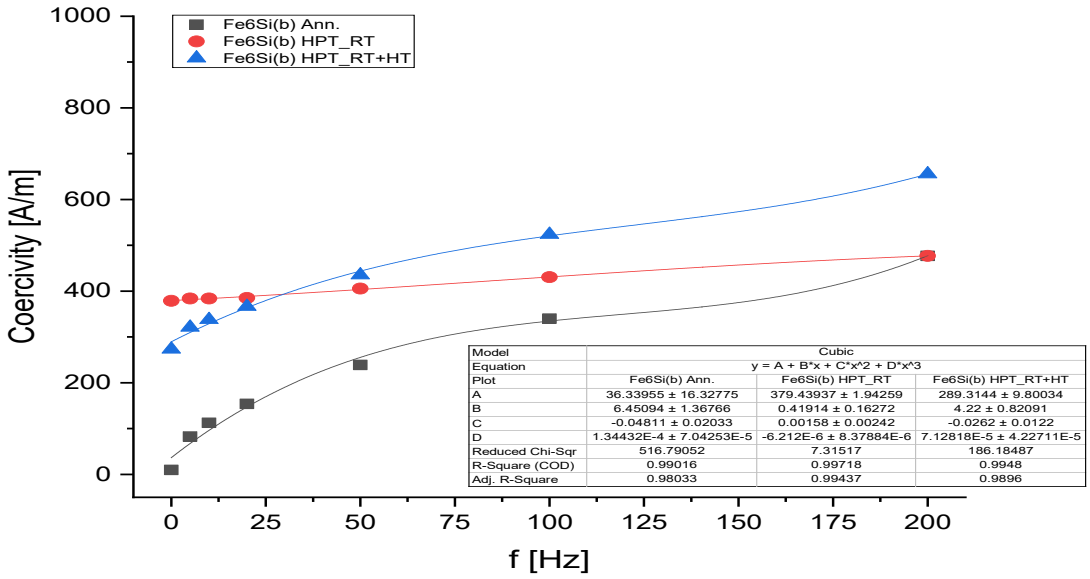

Model	Cubic		
Equation	y = A + B*x + C*x^2 + D*x^3		
Plot	Fe6Si(b) Ann.	Fe6Si(b) HPT_RT	Fe6Si(b) HPT_RT+HT
A	36.33955 ± 16.32775	379.43937 ± 1.94259	289.3144 ± 9.80034
B	6.45094 ± 1.36766	0.41914 ± 0.16272	4.22 ± 0.82091
C	-0.04811 ± 0.02033	0.00158 ± 0.00242	-0.0262 ± 0.0122
D	1.34432E-4 ± 7.04253E-5	-6.212E-6 ± 8.37884E-6	7.12818E-5 ± 4.22711E-5
Reduced Chi-Sqr	516.79052	7.31517	186.18487
R-Square (COD)	0.99016	0.99718	0.9948
Adj. R-Square	0.98033	0.99437	0.9896

Figure 4.22: Comparison of Coercivity (A/m) vs Frequency (Hz) of Annealed and HPT-deformed bulk Fe-6.5wt%Si samples. HPT deformation is done at room temperature.

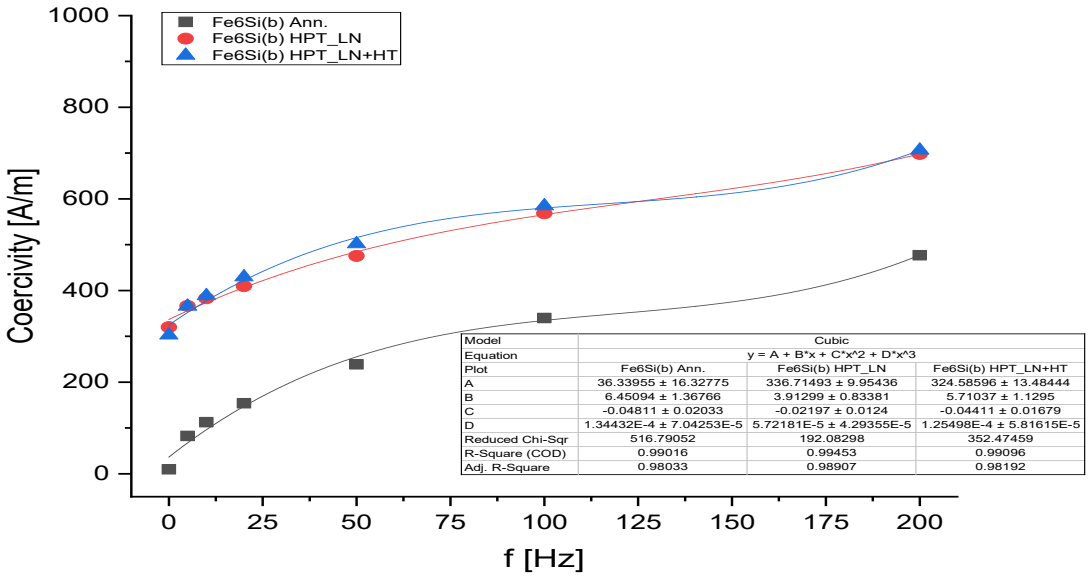

Model	Cubic		
Equation	y = A + B*x + C*x^2 + D*x^3		
Plot	Fe6Si(b) Ann.	Fe6Si(b) HPT_LN	Fe6Si(b) HPT_LN+HT
A	36.33955 ± 16.32775	336.71493 ± 9.95436	324.58596 ± 13.48444
B	6.45094 ± 1.36766	3.91299 ± 0.83381	5.71037 ± 1.1295
C	-0.04811 ± 0.02033	-0.02197 ± 0.0124	-0.04411 ± 0.01679
D	1.34432E-4 ± 7.04253E-5	5.72181E-5 ± 4.29355E-5	1.25498E-4 ± 5.81615E-5
Reduced Chi-Sqr	516.79052	192.08298	352.47459
R-Square (COD)	0.99016	0.99453	0.99096
Adj. R-Square	0.98033	0.98907	0.98192

Figure 4.23: Comparison of Coercivity (A/m) vs Frequency (Hz) of Annealed and HPT-deformed bulk Fe-6.5wt%Si samples. HPT deformation is done at liquid nitrogen temperature.

Fig. 4.21 shows hysteresis curves of annealed and HPT deformed and heat-treated bulk Fe-6.5wt%Si samples while Fig. 4.22 and Fig. 4.23 show comparison of annealed and HPT-deformed bulk Fe-6.5wt%Si samples. Compared to annealed samples, deformed samples show higher coercivity. In case of room temperature deformation, heat treatment seems to increase coercivity especially at higher frequencies. In case of liquid nitrogen deformation there is very little difference between HPT-deformed and heat-treated samples.

4.8.5 Hysteresis Measurements of HPT-Deformed Powder Fe-6.5wt%Si

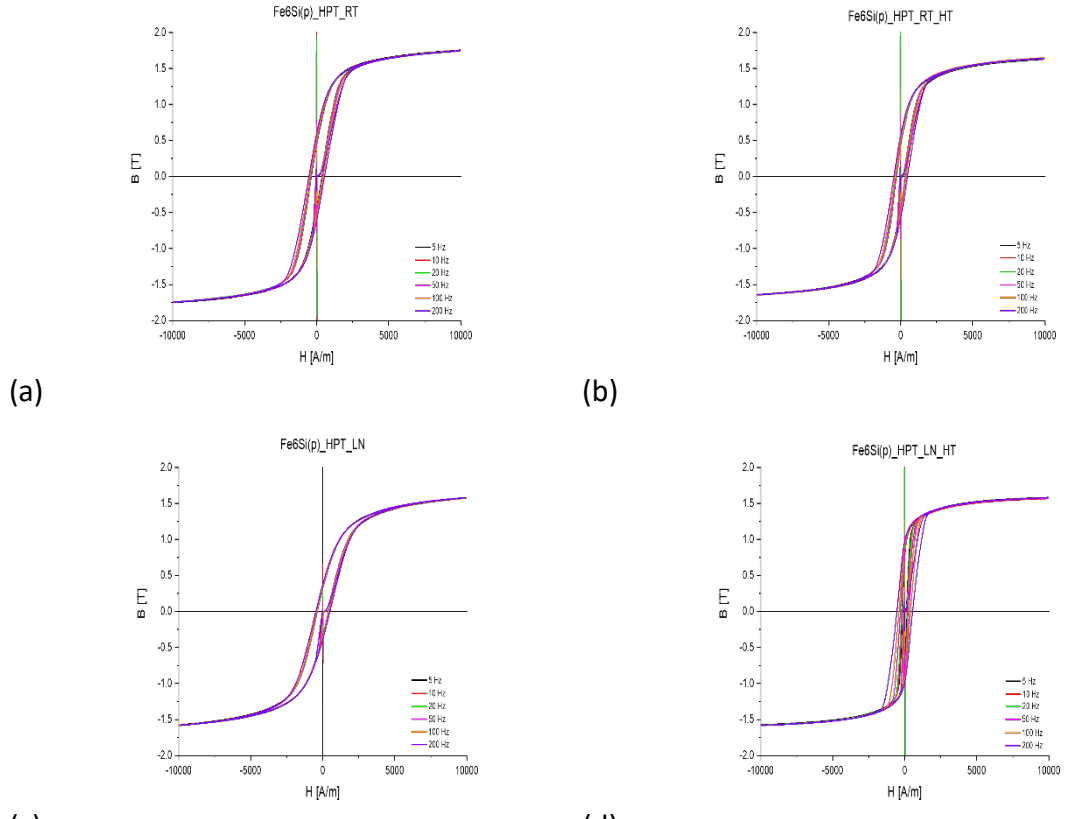

(a) (b)

(c) (d)

Figure 4.24: The frequency-dependent hysteresis loops of HPT-deformed Powder Fe-6.5wt%Si (a) deformed at room temperature; (b) deformed at room temperature followed by heat treatment; (c) deformed at liquid nitrogen temperature; (d) deformed at liquid nitrogen temperature followed by heat treatment.

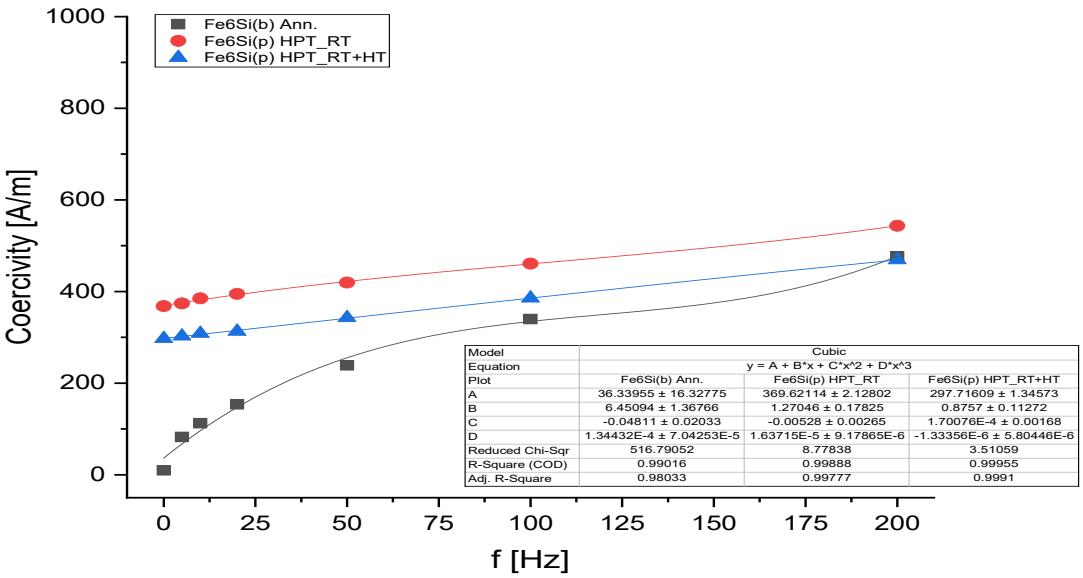

Model	Cubic		
Equation	y = A + B*x + C*x^2 + D*x^3		
Plot	Fe6Si(b) Ann.	Fe6Si(p) HPT_RT	Fe6Si(p) HPT_RT+HT
A	36.33955 ± 16.32775	369.62114 ± 2.12802	297.71609 ± 1.34573
B	6.45094 ± 1.36766	1.27046 ± 0.17825	0.8757 ± 0.11272
C	-0.04811 ± 0.02033	-0.00528 ± 0.00265	1.70076E-4 ± 0.00168
D	1.34432E-4 ± 7.04253E-5	1.63715E-5 ± 9.17865E-6	-1.33356E-6 ± 5.80446E-6
Reduced Chi-Sqr	516.79052	8.77838	3.51059
R-Square (COD)	0.99016	0.99888	0.99955
Adj. R-Square	0.98033	0.99777	0.9991

Figure 4.25: Comparison of Coercivity (A/m) vs Frequency (Hz) of Annealed and HPT-deformed powder Fe-6.5wt%Si samples. HPT deformation is done at room temperature.

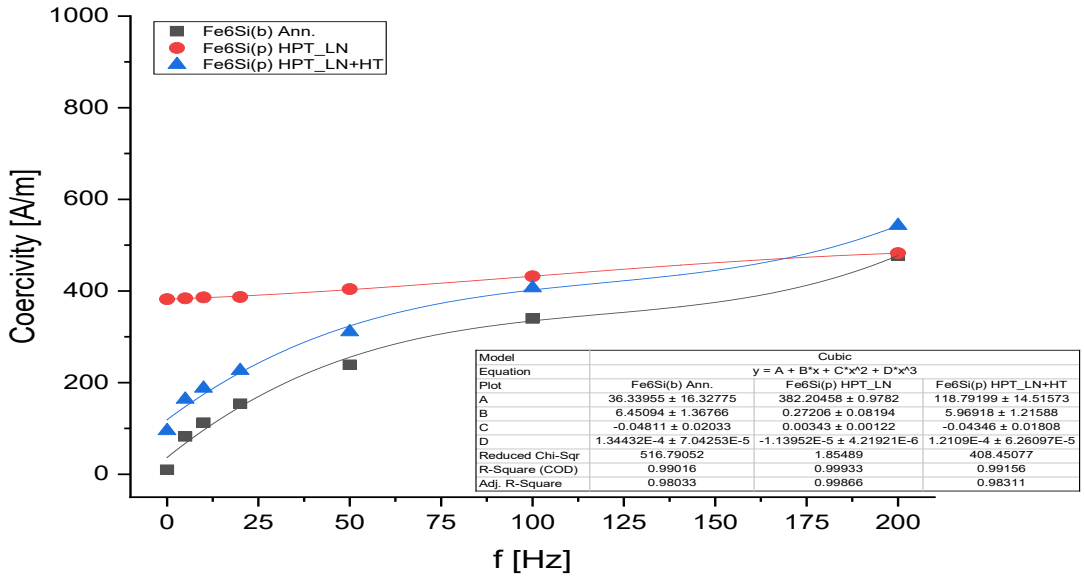

Model	Cubic		
Equation	y = A + B*x + C*x^2 + D*x^3		
Plot	Fe6Si(b) Ann.	Fe6Si(p) HPT_LN	Fe6Si(p) HPT_LN+HT
A	36.33955 ± 16.32775	382.20458 ± 0.9782	118.79199 ± 14.51573
B	6.45094 ± 1.36766	0.27206 ± 0.08194	5.96918 ± 1.21588
C	-0.04811 ± 0.02033	0.00343 ± 0.00122	-0.04346 ± 0.01808
D	1.34432E-4 ± 7.04253E-5	-1.13952E-5 ± 4.21921E-6	1.2109E-4 ± 6.26097E-5
Reduced Chi-Sqr	516.79052	1.85489	408.45077
R-Square (COD)	0.99016	0.99933	0.99156
Adj. R-Square	0.98033	0.99866	0.98311

Figure 4.26: Comparison of Coercivity (A/m) vs Frequency (Hz) of Annealed and HPT-deformed powder Fe-6.5wt%Si samples. HPT deformation is done at liquid nitrogen temperature.

Fig. 4.25 and Fig. 4.26 yield comparisons of powder HPT-deformed Fe-6.5wt%Si samples with annealed bulk Fe-6.5wt%Si sample. Results show that deformation increases the coercivity, but heat treatment generally decreases the coercivity to some extent. In case of liquid nitrogen deformation (Fig. 4.26), at higher frequencies, heat-treated samples show higher coercivity than HPT-deformed sample. At lower frequencies, heat treatment lowers coercivity compared to all other samples.

4.9 Zero-Frequency Extrapolated Coercivity

Eq. 2.14 which reads as ($\frac{P}{f} = C_o + C_1.f + C_2.f^{1/2}$) can be used to extrapolate the coercivity at 0 Hz frequency. Fig. 4.27 shows the extrapolated coercivity at zero frequency. Compared to the same materials researched in [90, 91] we can see that coercivity values are generally lower in the present research. For example, there is an 8% decrease in room temperature HPT-deformed bulk iron, while room temperature HPT-deformed bulk Fe-3wt%Si show a 44% decrease in coercivity.

Heat treating the samples, in case of iron and Fe-6.5wt%Si, show a further decrease in coercivity, while Fe-3wt%Si show a reverse trend, that is, coercivity increases after heat treatment. Only bulk samples are compared here because [90, 91] only worked with bulk samples.

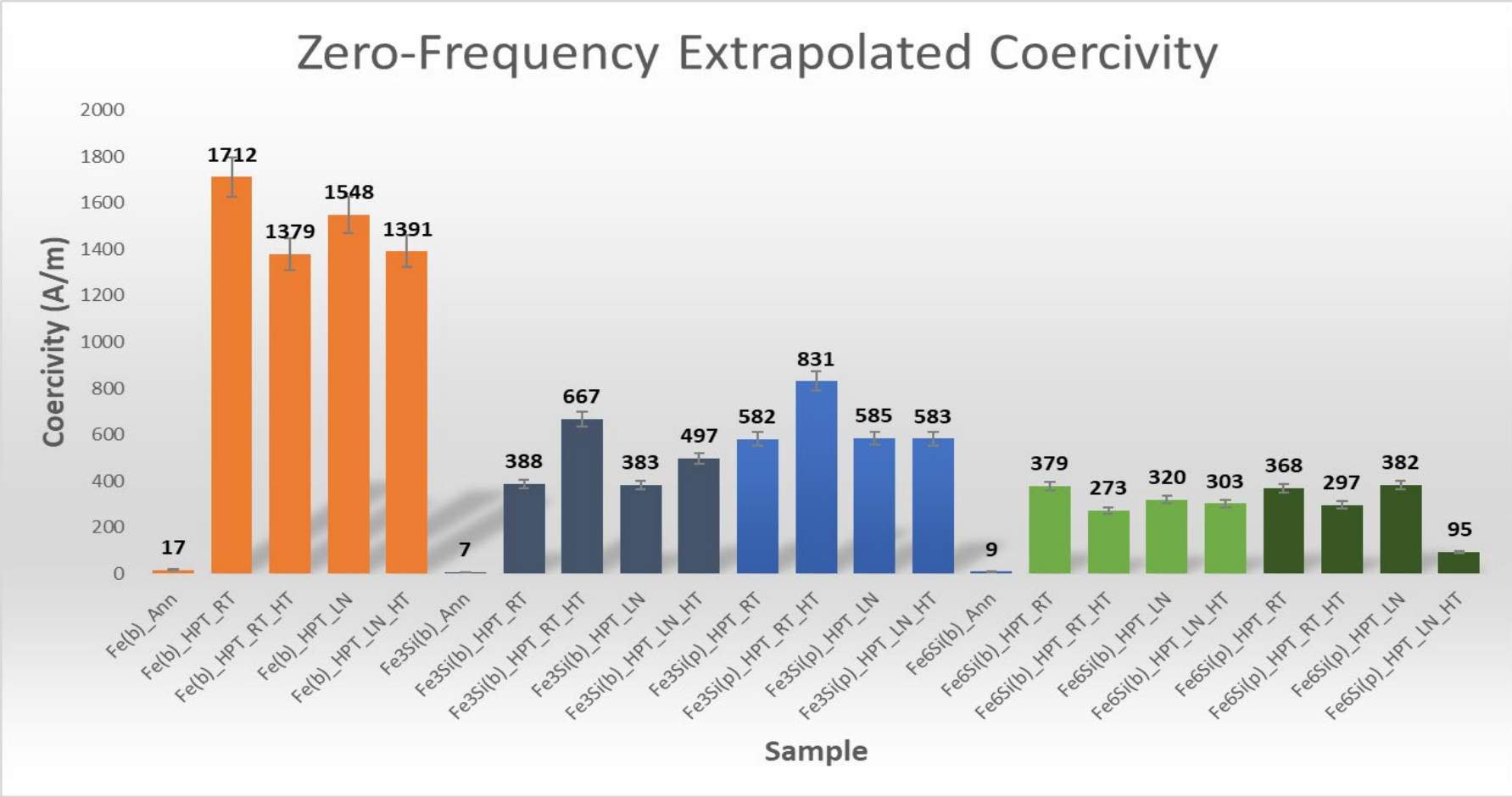

Figure 4.27: Zero-frequency extrapolated coercivity of Fe, Fe-3wt%Si and Fe-6.5wt%Si samples calculated from Eq. 2.14. “b” stands for bulk samples, “p” stands for powder samples, “RT” stands for HPT-processing at room temperature, “LN” stands for HPT-processing at liquid nitrogen temperature, “HT” refers to heat treatment at 200 ^{o}C for 2 hours.

4.10 Magnetic Losses

The area of the hysteresis curve gives the magnetic losses of that material at a particular frequency. This is done by integrating the area of the hysteresis curve in Origin software. Three frequencies have been chosen to represent the losses; 5 Hz (Fig. 4.28), 50 Hz (Fig. 4.29) and 200 Hz (Fig. 4.30).

4.10.1 Total Magnetic Losses at 5 Hz, 50 Hz and 200 Hz

The analysis of the data shows that the losses follow the same pattern as the coercivity because both quantities are dependent on each other. Fig. 4.28 shows losses at 5 Hz. Between the annealed and HPT-deformed bulk Iron samples, the annealed samples have the lowest losses. The losses rise about five to six-fold after the deformation. After heat treatment there is a decrease in losses.

In case of Fe-3wt%Si samples a reverse trend is observed in general. Heat treatment seems to increase the losses, except in case of heat-treated bulk Fe-3wt%Si samples deformed in liquid nitrogen. The Fe-6.5wt%Si samples show the least amount of losses compared to Iron ad Fe-3wt%Si samples. HPT deformation increases the losses but after heat treatment a decrease in losses is observed.

Fig. 4.29 shows losses at 50 Hz. This frequency is especially important for general electrical applications. The losses in all materials, more or less, show the same trend as in case of 5 Hz frequency. The magnitude of the losses is higher than the 5 Hz losses because at higher frequencies the Eddy current losses are higher. Fe-6.5wt%Si samples show the least amount of change because the presence of Si lowers the Eddy current losses by increasing the resistivity of the sample.

Finally, Fig. 4.30 shows the losses at 200 Hz. Only the magnitude of the losses is higher compared to the previous two frequencies while the trend remains the same except for a couple of samples. For example, after heat treatment the HPT-deformed powder Fe-6.5wt%Si sample shows a higher loss compared to the same at 5 and 50 Hz. However, the values are within the margin of error.

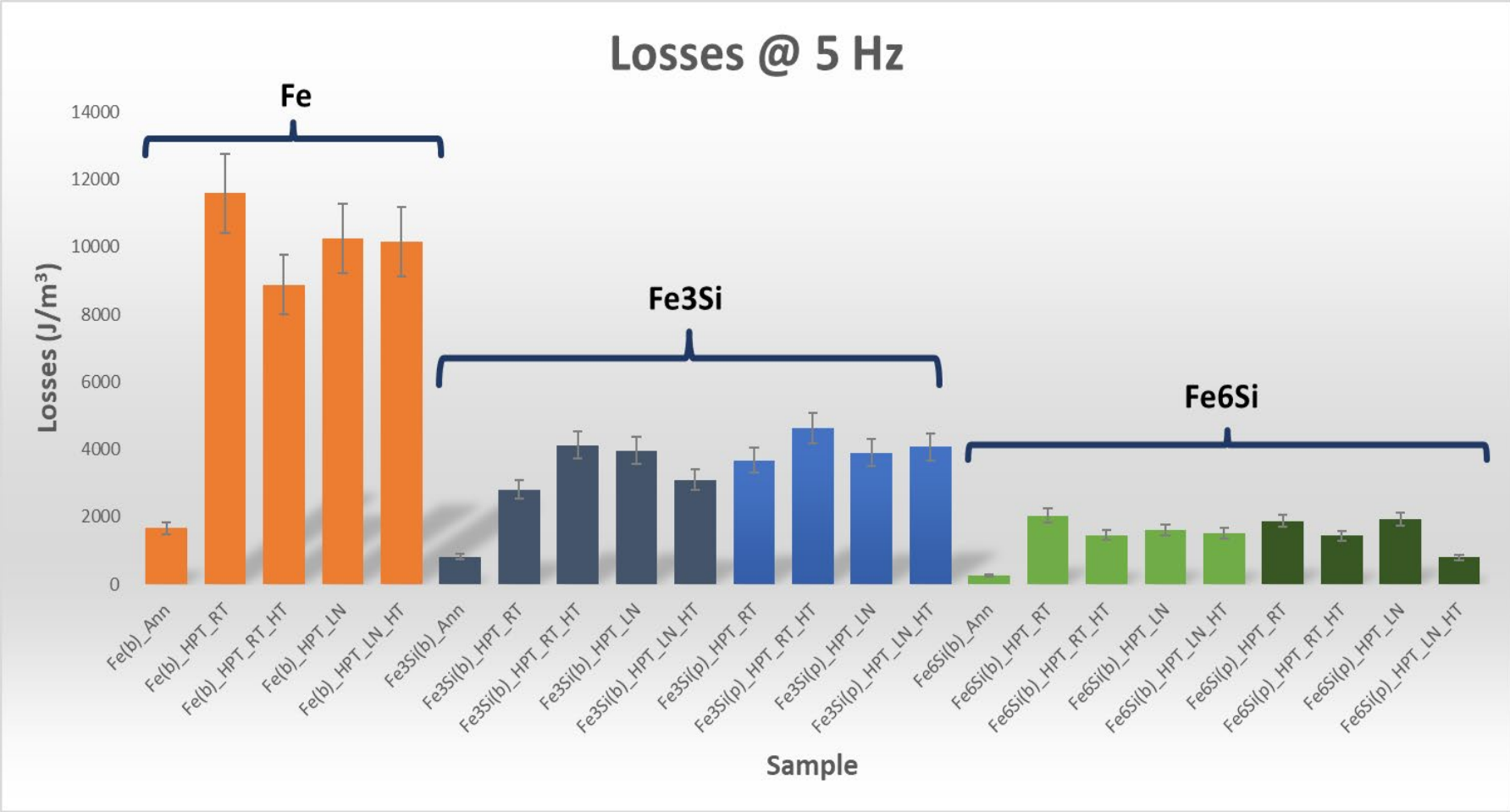

Figure 4.28: Total losses at 5 Hz frequency calculated by integrating the hysteresis curve area.

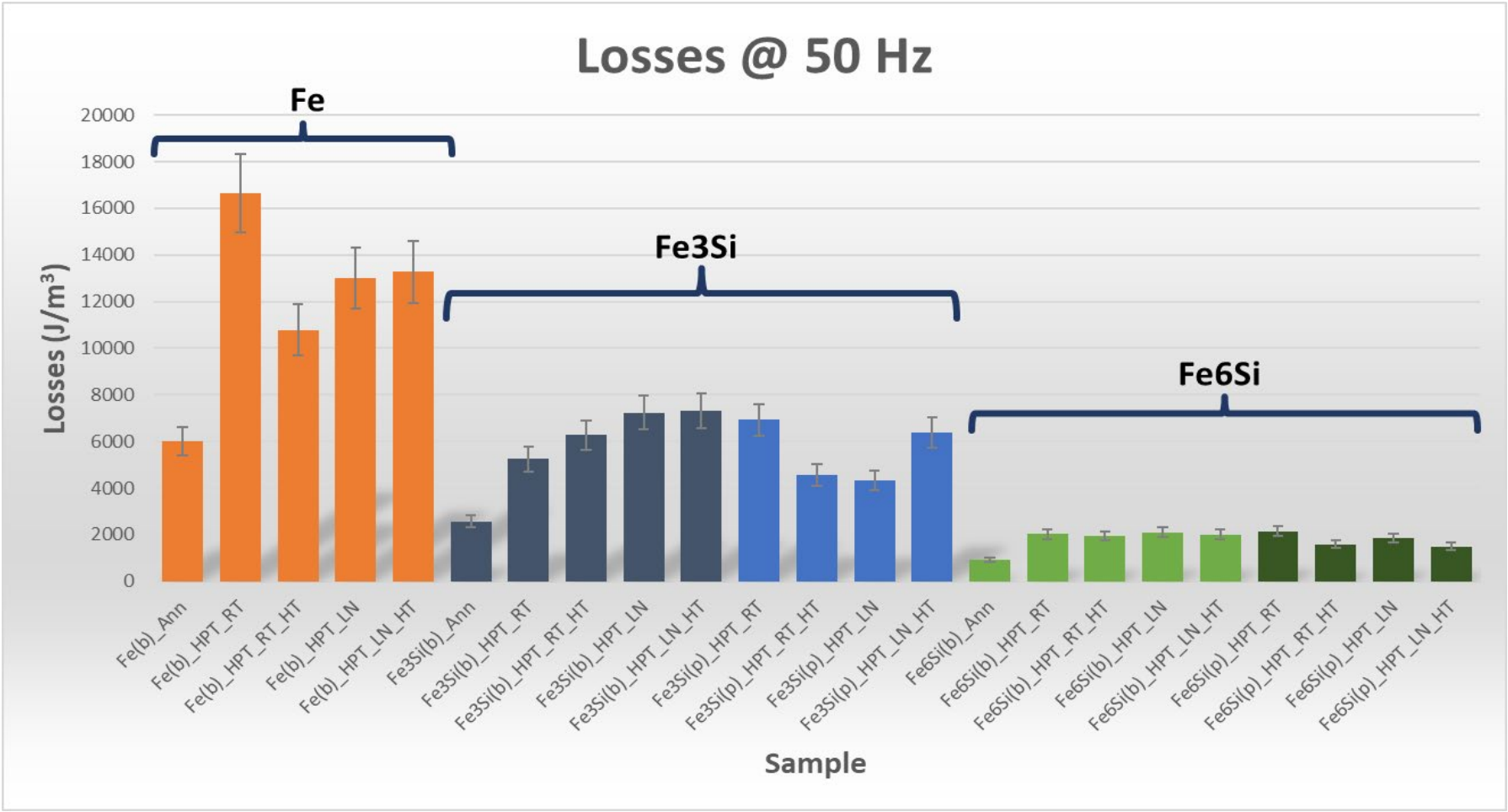

Figure 4.29: Total losses at 50 Hz frequency calculated by integrating the hysteresis curve area.

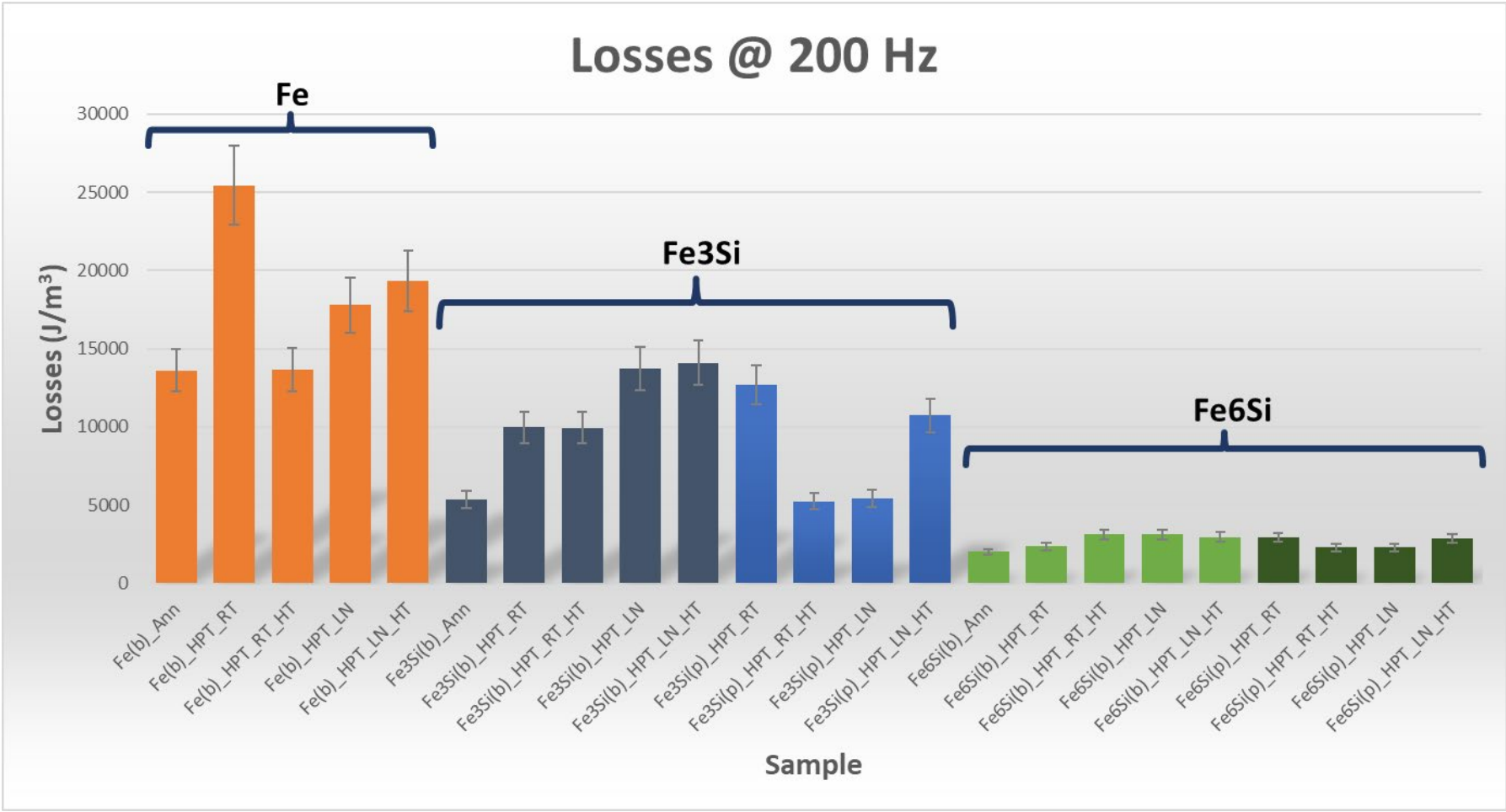

Figure 4.30: Total losses at 200 Hz frequency calculated by integrating the hysteresis curve area.

4.10.2 Magnetic Losses at 0 Hz

Eq. 2.14 which reads as ($\frac{P}{f} = C_o + C_1.f + C_2.f^{1/2}$) can also be used to extrapolate losses at 0 Hz frequency. C_o represents the static losses and it gives great insight into the composition and microstructure of the material under investigation. Static losses are frequency-independent. C_1 represents classical Eddy current losses while C_2 represents excess Eddy current losses.

Fig. 4.31 shows static losses of the materials under investigation. The graph signifies the importance of Si addition in Iron as losses decrease by three to four-fold as the percentage of Si is increased in Iron. In terms of magnitude at 0 Hz, static losses represent the largest portion of the total losses. In bulk Iron, HPT deformation increases the losses whereas heat treatment lowers the losses to some extent. In case of Fe-3wt%Si a reverse behavior is observed in room temperature deformed bulk and powder samples where heat treatment increases the losses. In liquid nitrogen HPT-deformed samples, heat treatment decreases the losses. In case of Fe-6.5wt%Si, heat treatment reduces the losses.

Fig. 4.32 shows the classical Eddy current losses at 0 Hz. There does not appear to be a trend in the values across all materials. In some cases heat treatment reduces the losses whereas in other cases it increases the losses. It should be noted that there are several variables that affect Eddy current losses such as composition, conductivity/resistivity etc. the density of powder samples is 97% ± 1.5% compared to theoretical density so it may be another factor in determining the coercivity and losses of the corresponding samples.

Fig. 4.33 shows excess Eddy current losses of the samples. These losses depend on the damping of the domain wall motion. Some values are omitted because the margin of error was equivalent to or greater than the obtained value which made the value unreliable for any meaningful interpretation of the results.

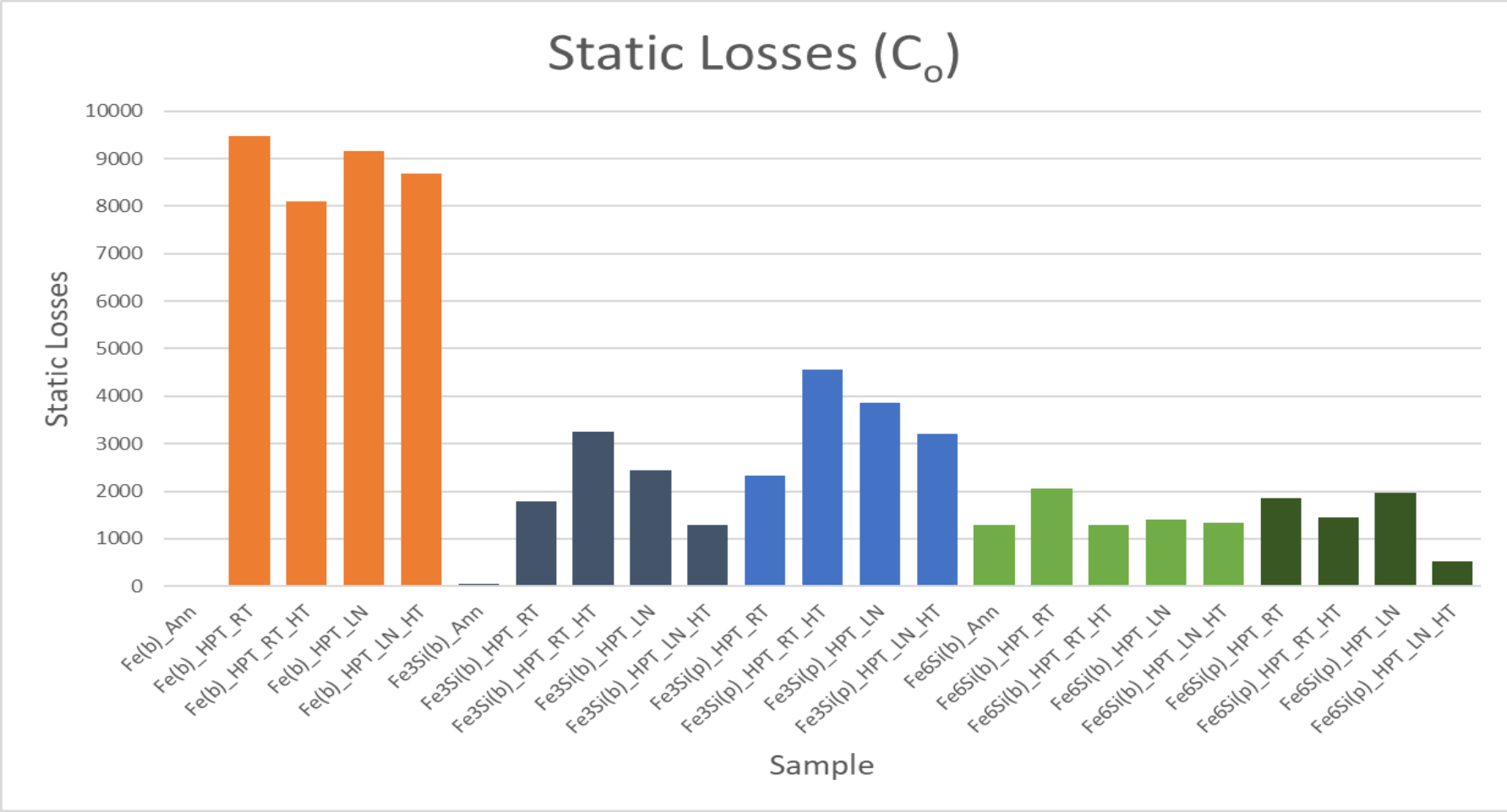

Figure 4.31: Static losses at 0 Hz frequency.

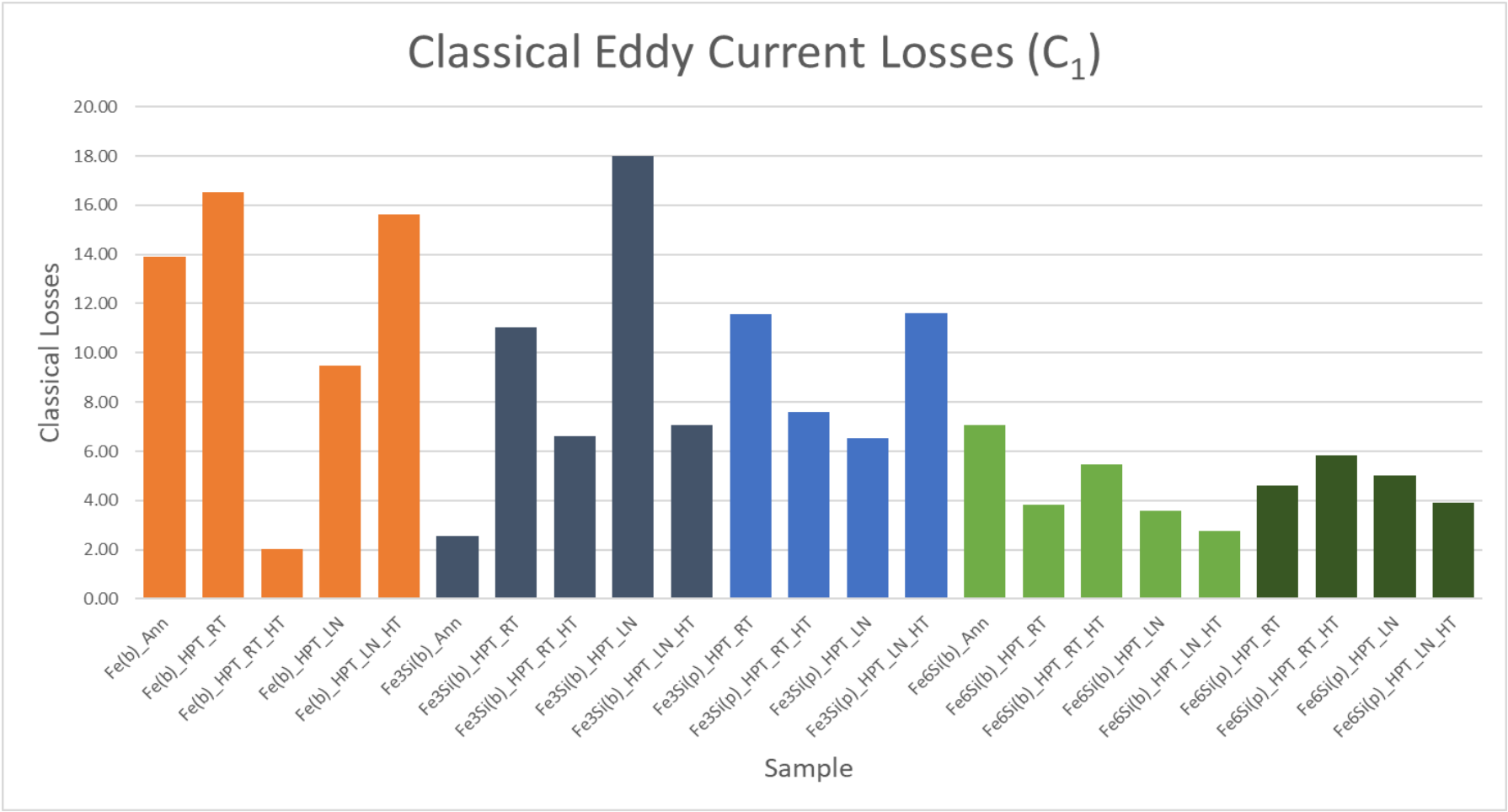

Figure 4.32: Classical Eddy Current losses at 0 Hz frequency.

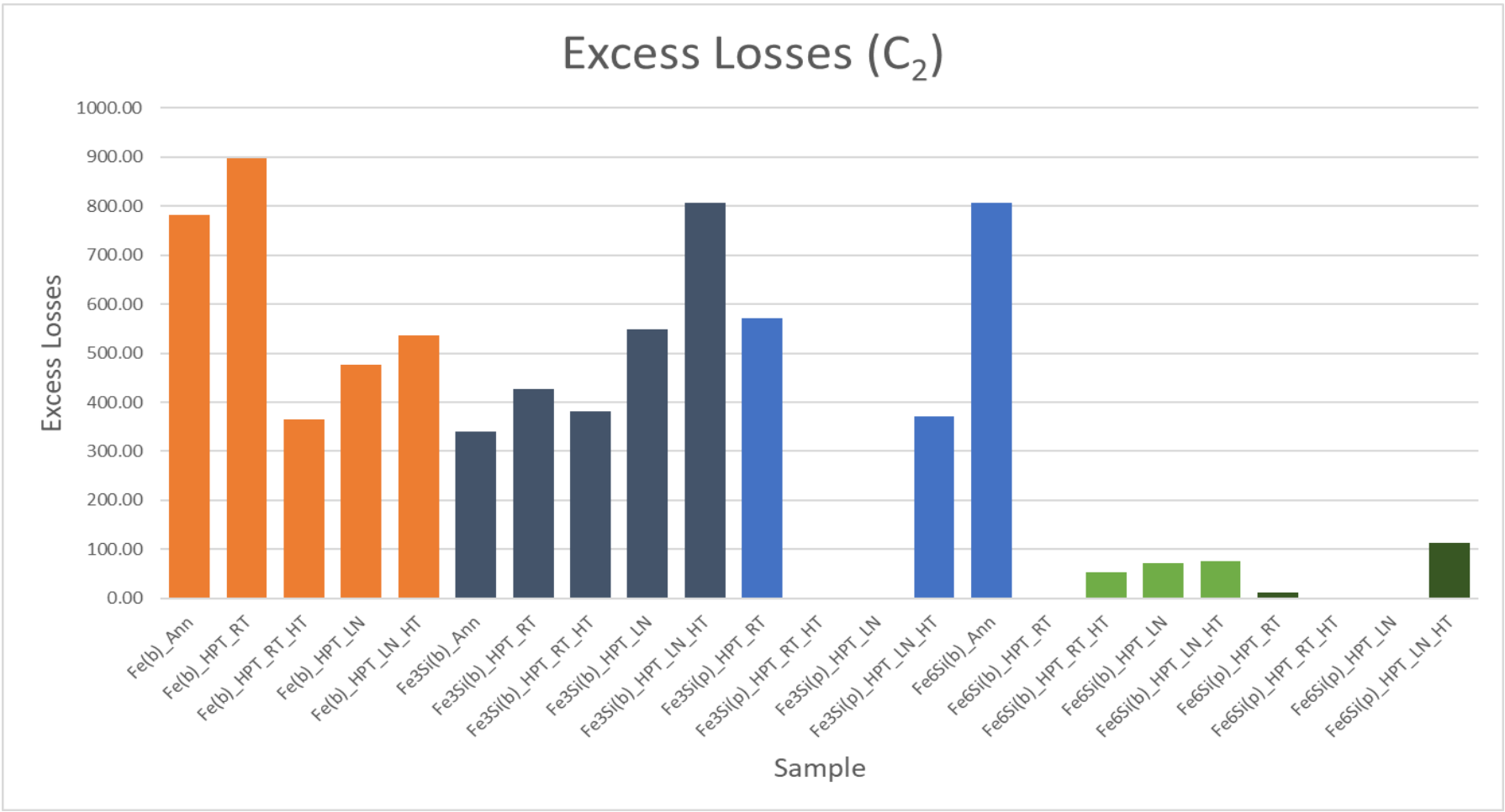

Figure 4.33: Excess Eddy Current losses at 0 Hz frequency.

4.11 Relative Permeability μ_r of Fe, Fe-3wt%Si and Fe-6.5wt%Si Samples

Fig. 4.34 to Fig. 4.38 show permeabilities μ_r of undeformed and HPT-deformed Fe, Fe-3wt%Si and Fe-6.5wt%Si samples. Compared to undeformed samples, HPT deformation reduces the relative permeability in all cases except in the case of pure Iron.

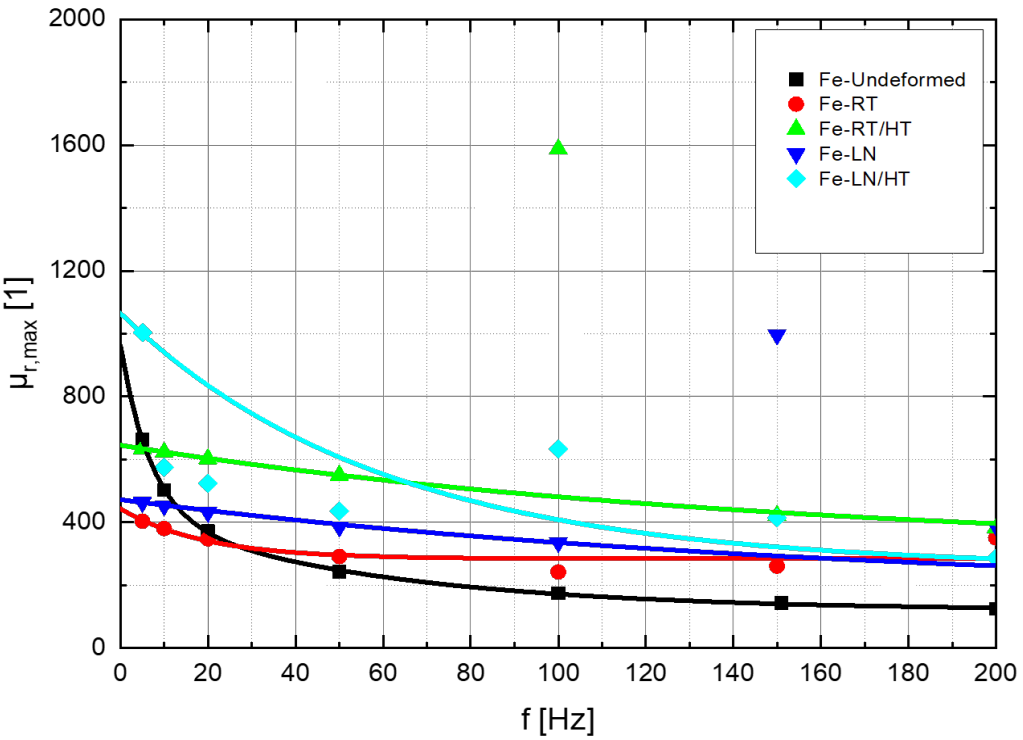

Figure 4.34: Maximum relative permeability vs Frequency (Hz) of HPT-deformed bulk Fe samples.

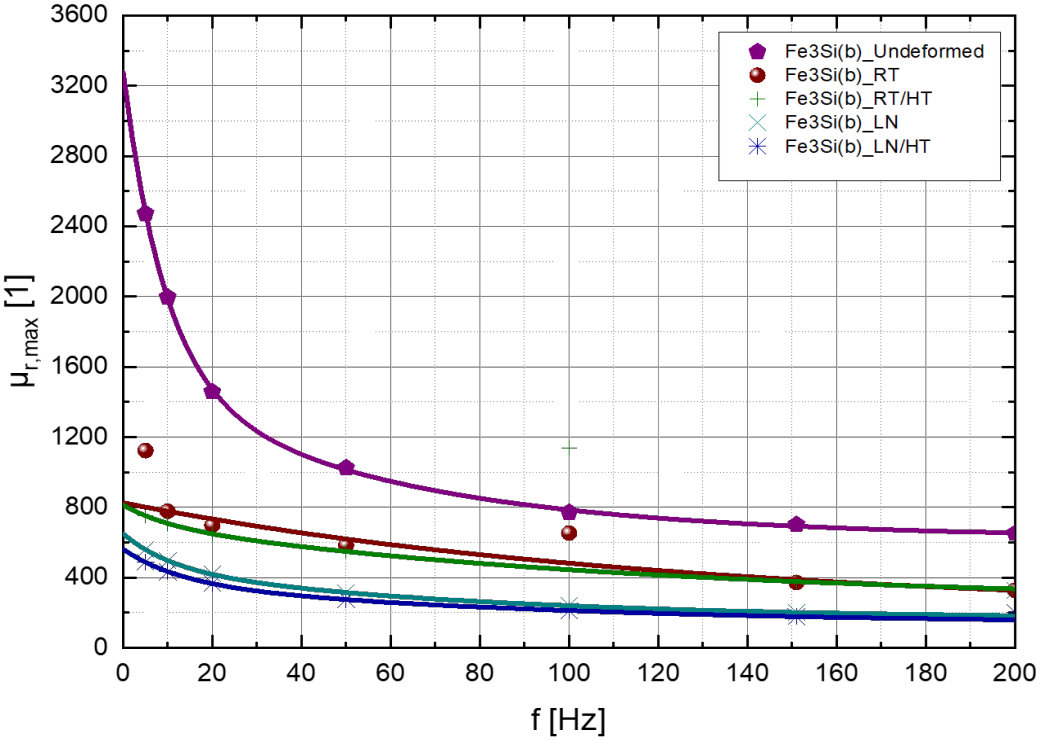

Figure 4.35: Maximum relative permeability vs Frequency (Hz) of HPT-deformed bulk Fe-3wt%Si samples.

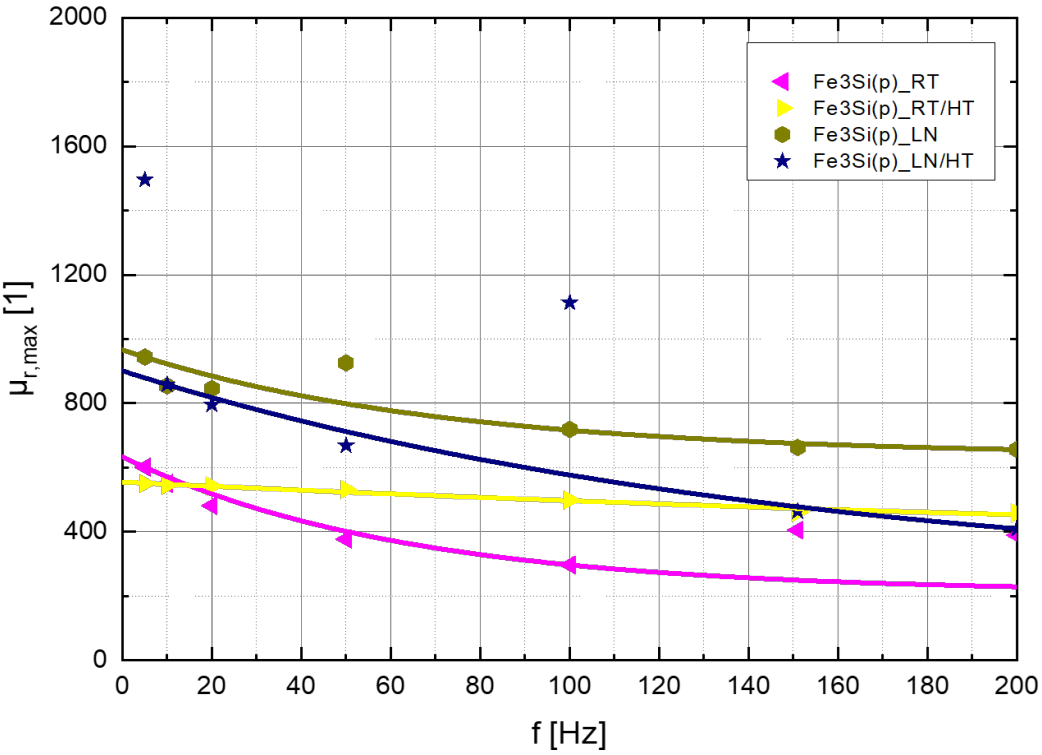

Figure 4.36: Maximum relative permeability vs Frequency (Hz) of HPT-deformed powder Fe-3wt%Si samples.

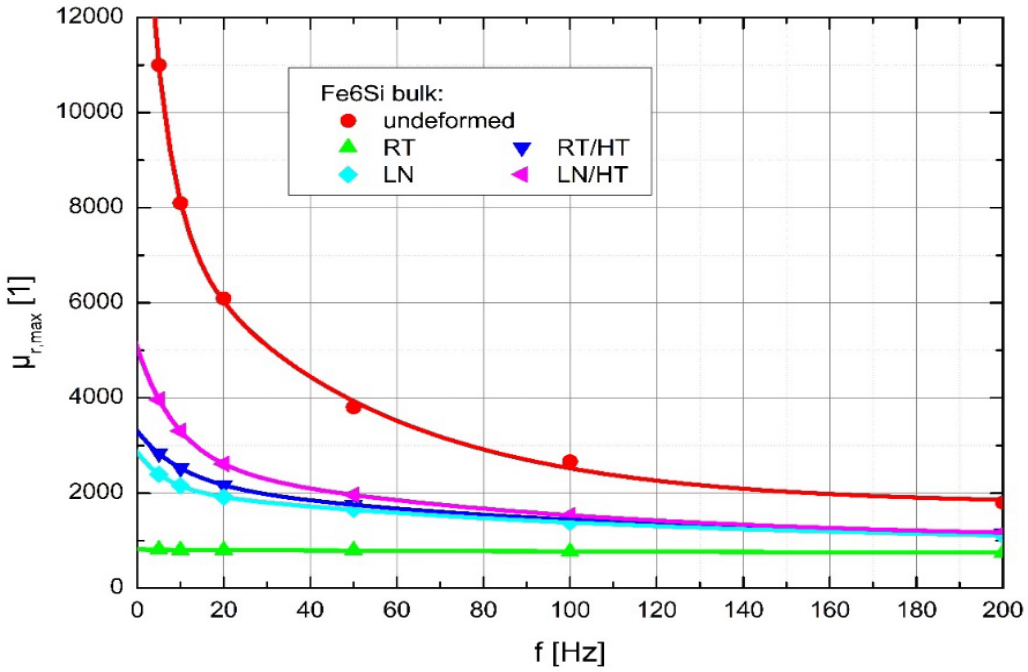

Figure 4.37: Maximum relative permeability vs Frequency (Hz) of HPT-deformed bulk Fe-6.5wt%Si samples.

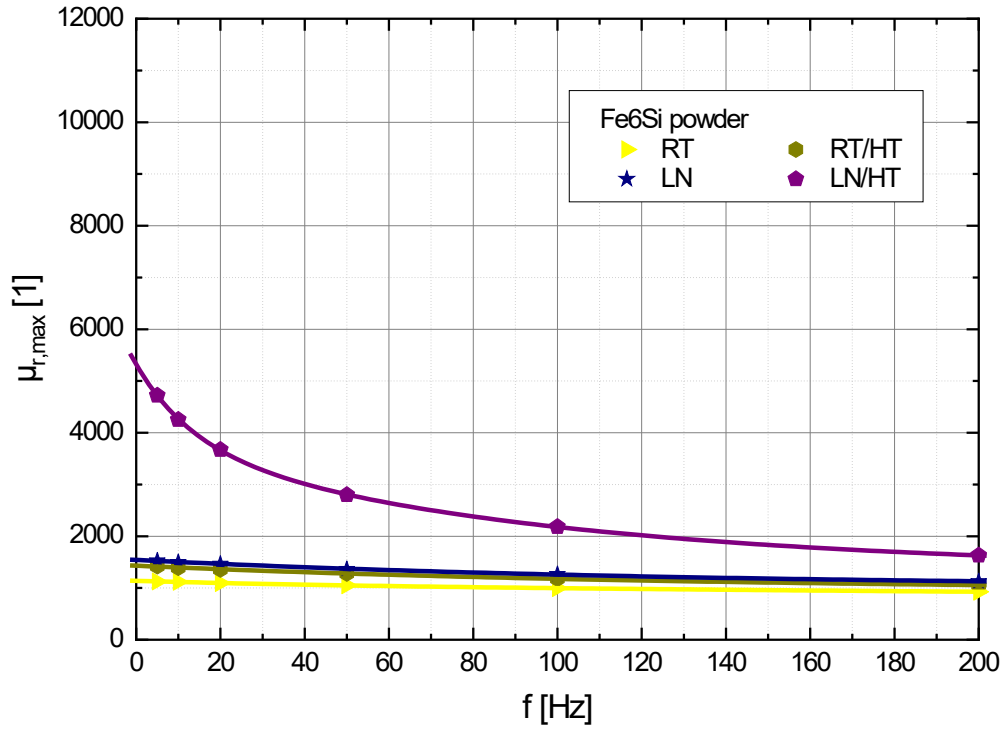

Figure 4.38: Maximum relative permeability vs Frequency (Hz) of HPT-deformed powder Fe-6.5wt%Si samples.

Eddy currents are one reason why permeability is reduced. Due to Eddy currents the magnetic field is unable to penetrate deep into the magnetic material and is rather concentrated in the surface layer. At higher frequencies when Eddy currents increase, permeability further decreases. Permeability also depends upon the coercive field strength as well the frequency with which this coercive field is applied. It is non-linear and depends upon several parameters such as temperature [172]. When coercivity increases with increasing frequency the permeability decreases. Generally, after HPT deformation the permeability decreases but tends to be more stable (i.e., almost remains constant) at higher frequencies.

The whole idea of magnetic permeability is how easily a material allows to form a magnetic field within itself in response to an outside magnetic field. Therefore, it is easy to imagine that high stress and strain fields would interfere with the ability of the material to generate magnetic fields within it. HPT deformation generally reduces the relative permeability to about half (or less) the value of the corresponding undeformed material. Heat treatment increases permeability in some cases and reduces it in other cases. This may be because of an interplay between strain fields and the Eddy currents. If Eddy currents are increased due to heat treatment (i.e., if it reduces resistivity) then it will negatively affect permeability. Similarly, if strain fields are high they will again reduce permeability.

4.12 Microstructure of Amorphous VITROPERM Alloy

Fig. 4.39 shows HPT-deformed amorphous VITROPERM sample deformed at 400 ^{o}C under 10 GPa pressure and 5 rotations. Fig. 4.40 shows the same material deformed under the same pressure but at room temperature for 20 rotations. Results show that higher deformation (20 rotations vs. 5 rotations) plus a lower deformation temperature (room temperature vs. 400 ^{o}C) greatly improves the quality of the VITROPERM samples. At higher temperature and lower deformation there are large cracks (of the order of 100 μm) visible in Fig. 4.39, whereas at lower temperature and higher deformation the cracks are reduced, and the size of cracks is also reduced (of the order of 10 μm or less) as shown in Fig. 4.40. Through experience in working with this material it is the opinion of the

author that completely eliminating cracks does not seem likely. The quality of the sample can be improved to some extent but some cracks will always be there because of the nature of the sample and the deforming process.

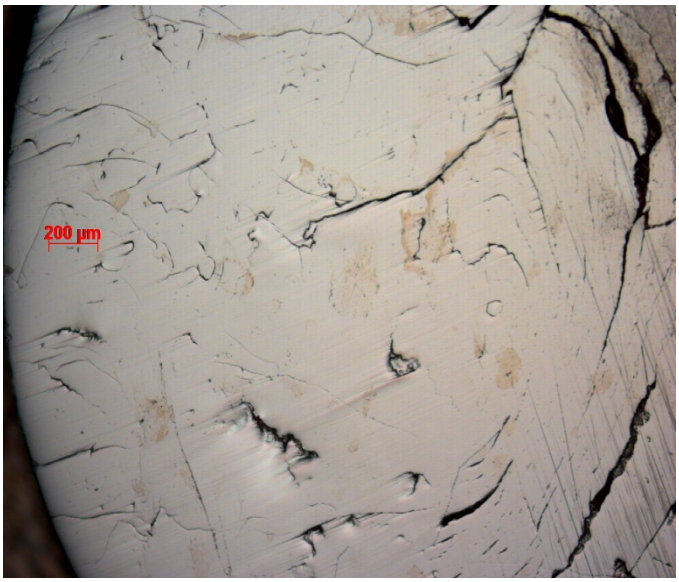

(a)

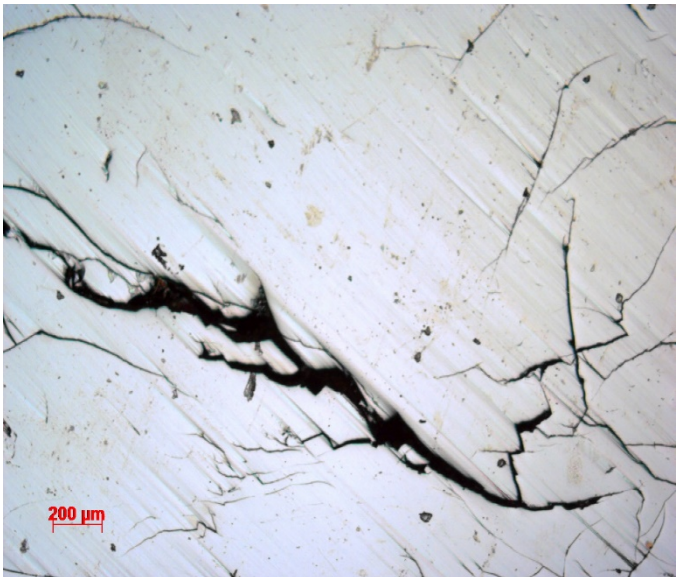

(b)

Figure 4.39: Optical micrographs of HPT-deformed amorphous VITROPERM P = 10 GPa, 5 rotations, 400 ^{o}C. (a) and (b) 50x

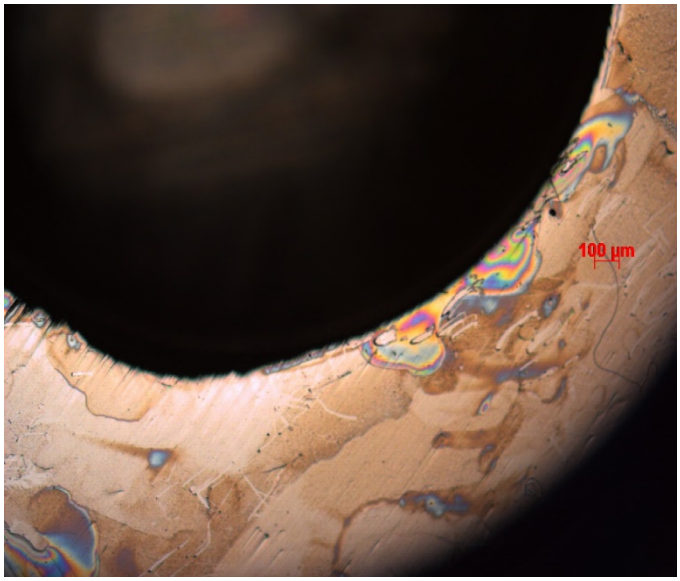

(a)

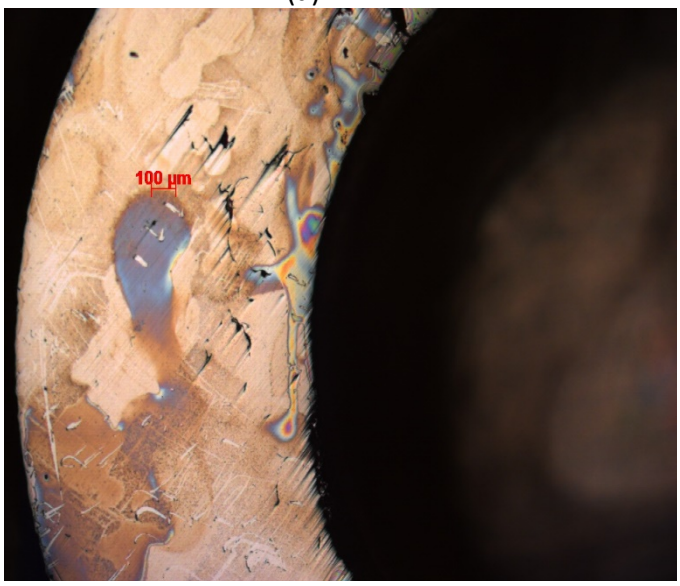

(b)

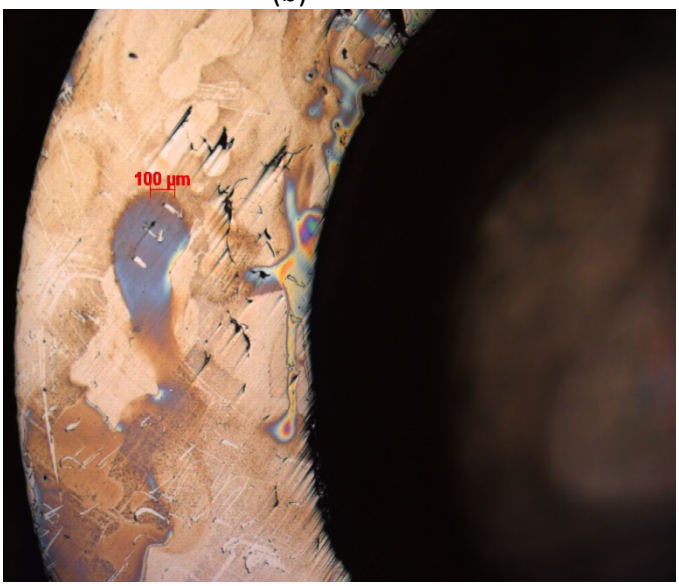

(c)

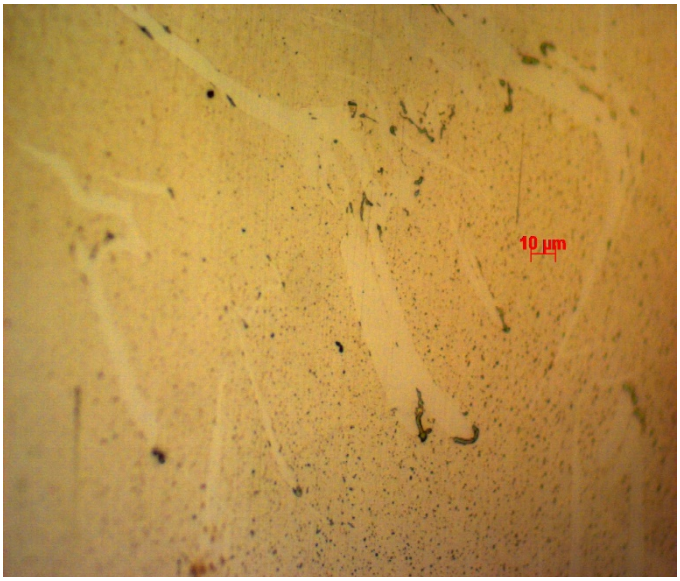

(d)

Figure 4.40: Optical micrographs of HPT-deformed Amorphous VITROPERM P = 10 GPa, 20 rotations, room temperature. (a), (b) and (c) 50x; (d) 500x

When the deformation starts there is a small explosion that takes place when the machine is applying pressure on the sample. This explosion removes some material from the sample. The same behavior is observed in the lab with other amorphous alloys too (for example, some Co-based amorphous alloys). This removal of material is also a reason why the quality of the sample degrades. It may be possible to reduce this effect by slowing down the speed of application of pressure. This would require a change in the equipment itself. It should also be noted that one needs to finely polish the sample to get good quality surface. Amorphous VITROPERM is very soft and erodes at a very high rate. If the sample is thin, it may not be possible to polish it. On the other hand, if the sample is too thick then there will be no deformation in the middle of the sample. For samples thicker than 0.4 - 0.5 mm one could actually see undeformed layer in the middle of the sample. In the present study good results were obtained when an anvil cavity depth of 0.25 mm was used.

4.13 Microstructure of Nanocrystalline VITROPERM Alloys

Nanocrystalline VITROPERM is much more brittle than amorphous VITROPERM. It behaves like a thin sheet of glass whereas amorphous VITROPERM is more ductile. Due to this there are much larger cracks (sometimes of the order of mm) in nanocrystalline VITROPERM as can be seen in Fig 4.41.

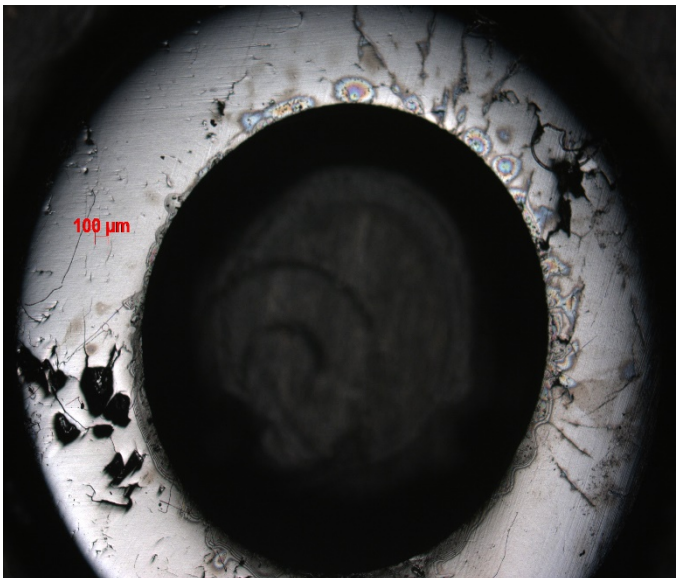

(a)

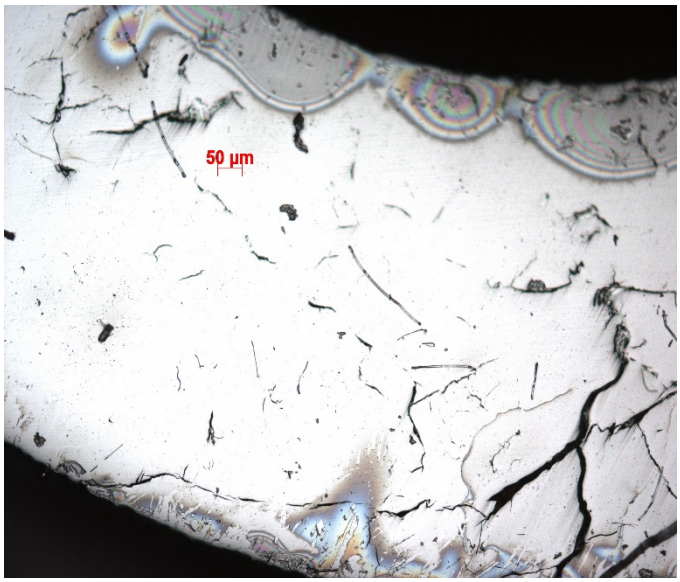

(b)

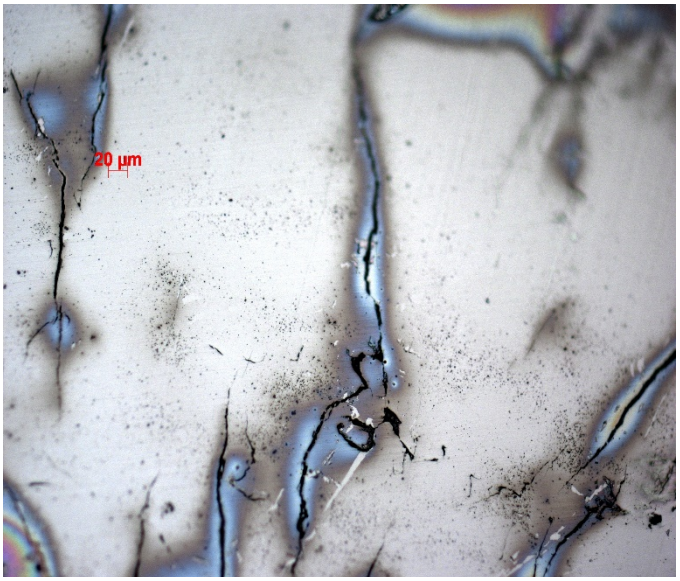

(c)

Figure 4.41: Optical micrographs of HPT-deformed Nanocrystalline VITROPERM P = 10 GPa, 20 rotations, room temperature. (a) 25x; (b) 100x; (c) 200x.

4.14 DSC and XRD of Amorphous and Nanocrystalline VITROPERM Alloys

Fig. 4.42 shows a comparison of DSC graphs obtained from an undeformed amorphous VITROPERM foil (Fig. 4.42a) and an HPT-deformed amorphous VITROPERM sample (Fig. 4.42b). Both graphs show characteristic endothermic peak at around 530 ^{o}C which represents conversion of amorphous VITROPERM to nanocrystalline VITROPERM. These graphs also show that there is no crystallization happening in the amorphous VITROPERM due to HPT deformation. Some change in the shape of the peak is due to the huge amount of deformation induced in the sample due to HPT deformation. No crystallization in the amorphous VITROPERM is further corroborated by the XRD pattern shown in Fig. 4.44. Even the deformation at 400 ^{o}C shows no change in XRD profile. It should be noted that the samples after HPT deformation are finely polished before they are tested. It is possible that the surface of the HPT deformed sample may show some nanocrystallization, however, this was not tested.

Fig. 4.43 shows a comparison of DSC graphs obtained from an undeformed nanocrystalline VITROPERM foil (Fig. 4.43a) and an HPT-deformed nanocrystalline VITROPERM sample (Fig. 4.43b). As expected the graphs show no strong peaks as no phase change is occurring between room temperature and 600 °C.

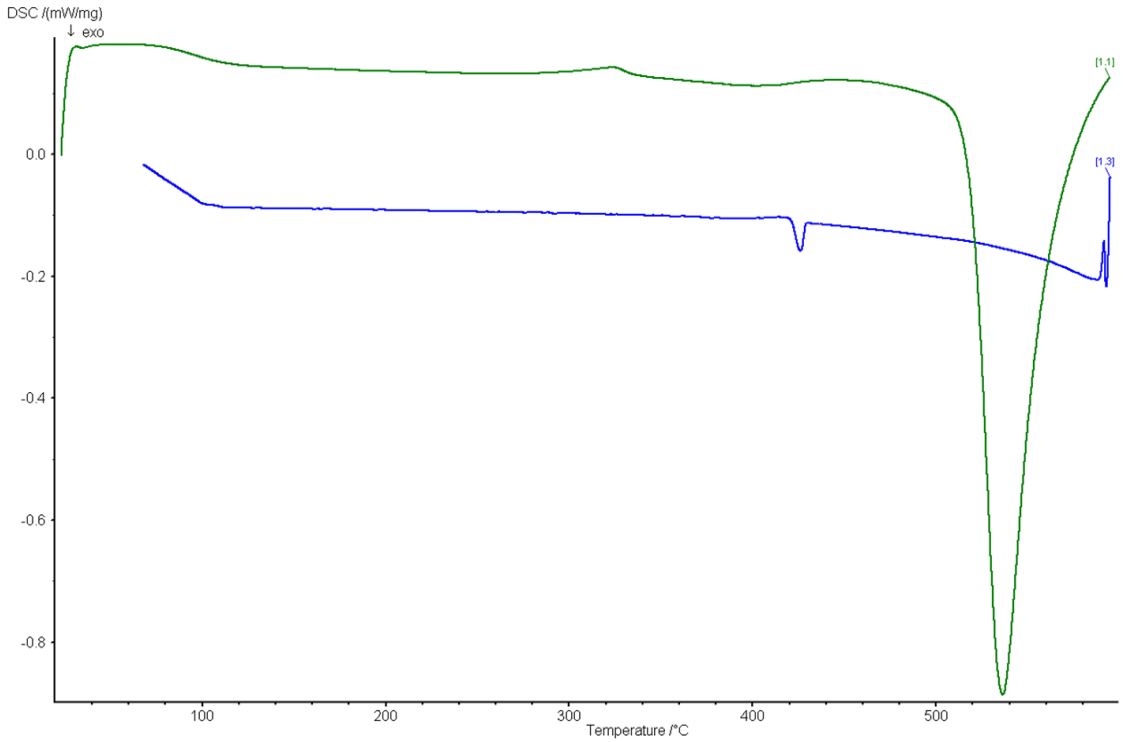

(a)

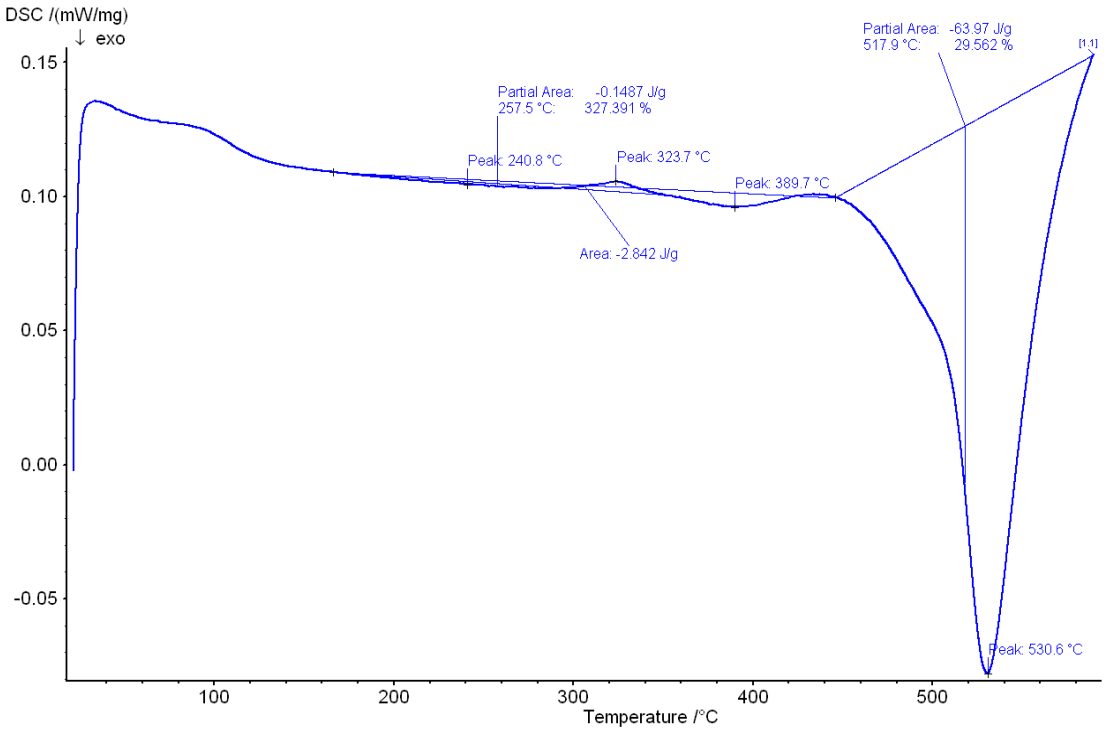

(b)

Figure 4.42: DSC graph of (a) Amorphous VITROPERM foil; (b) HPT-deformed Amorphous VITROPERM sample

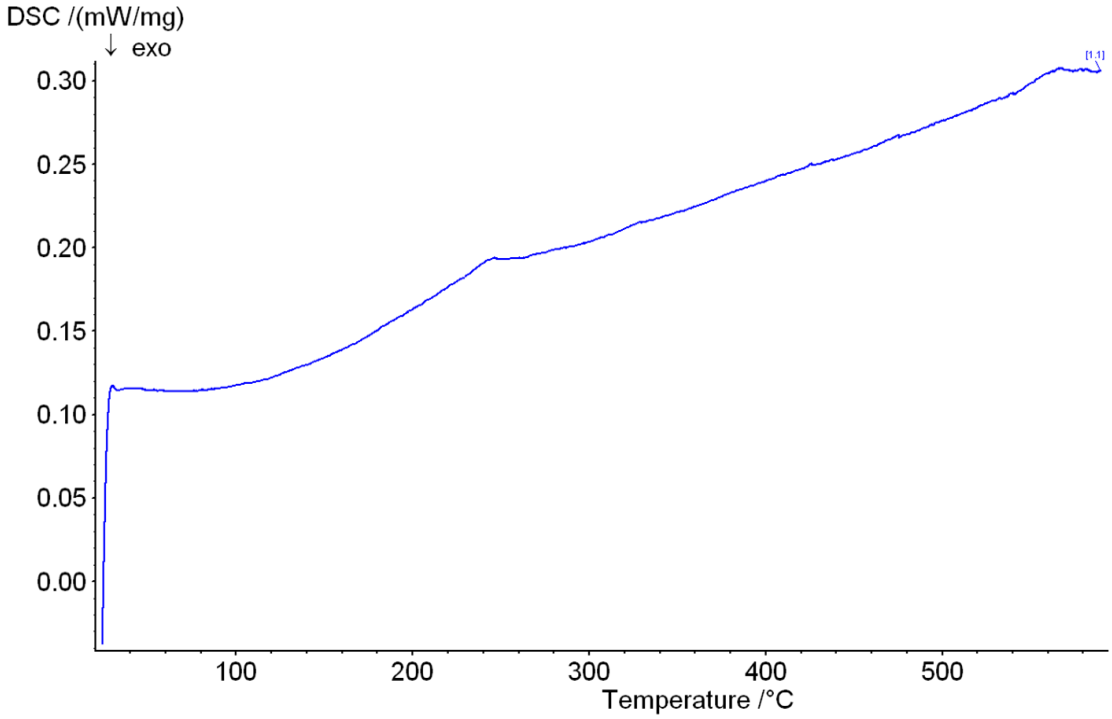

(a)

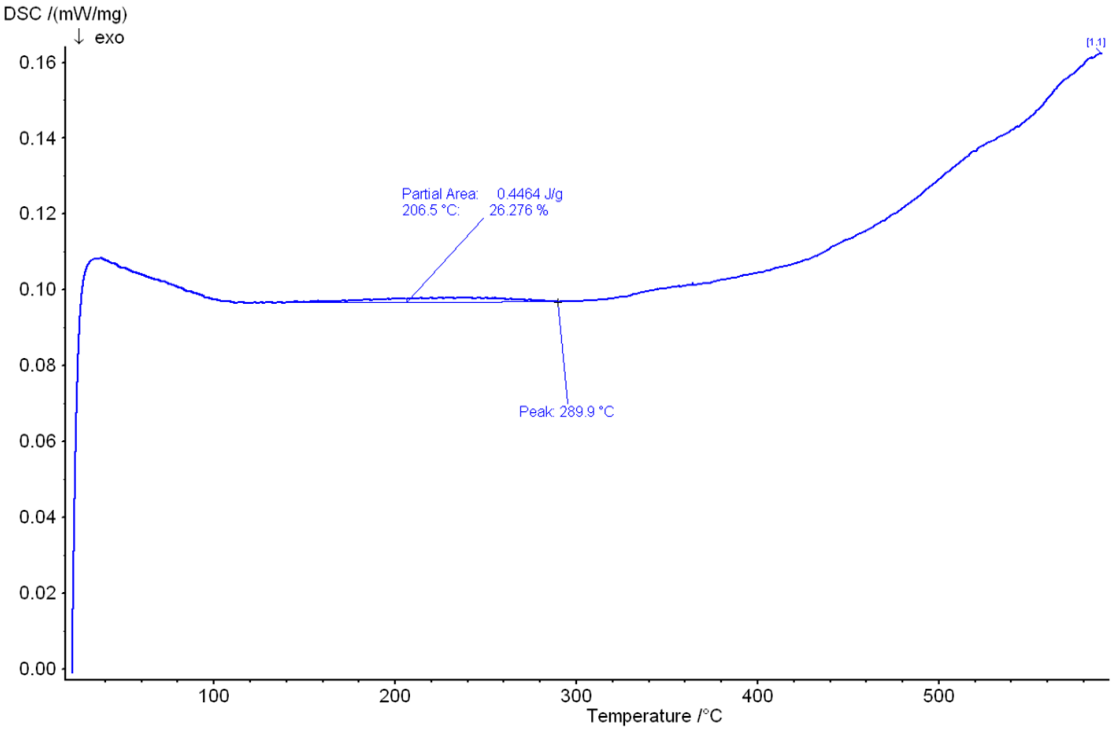

(b)

Figure 4.43: DSC graph of (a) Nanocrystalline VITROPERM foil; (b) HPT-deformed Nanocrystalline VITROPERM sample

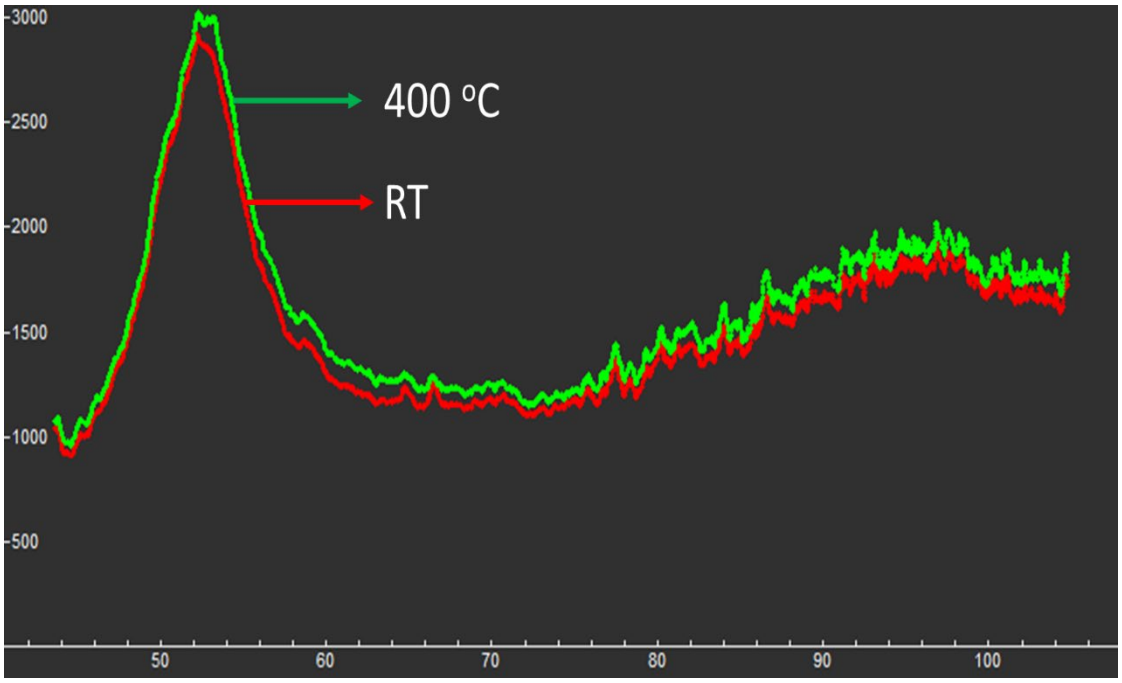

Figure 4.44: XRD pattern of HPT-deformed amorphous VITROPERM samples deformed at room temperature (RT) and 400 °C.

Chapter 5: Discussion

5.1 Fe and Fe-Si Alloys

Iron-based soft magnetic materials such as Fe, Fe-3wt%Si and Fe-6.5wt%Si were deformed using the High-Pressure Torsion (HPT) technique. The samples were deformed at room temperature and liquid nitrogen temperature. One of the goals of the present research was to see if the heat treatment of the HPT-deformed samples improves their soft magnetic properties. To find out appropriate heat treatment temperature Differential Scanning Calorimetry (DSC) was used (Fig. 4.1 – 4.3) and based on that all samples were heat treated at 200 ^{o}C for 2 hours. Two main techniques were used among others to characterize the samples; X-ray line profile analysis (XLPA) to determine crystallite size (Fig. 4.10) and dislocation density (Fig. 4.11) of the samples, and magnetic characterization through hysteresisgraph to find out coercivity, permeability, losses etc. Across all materials (Fe, Fe-3wt%Si and Fe-6wt%Si) the largest impact on magnetic properties is made by the addition of Si. Si is the best addition to Iron with regards to soft magnetic properties. It increases the resistivity of Iron which reduces the Eddy current losses, decreases coercivity while keeping the saturation magnetization to an acceptable value. Adding 6.5wt% Si to Iron reduces the magnetostriction to almost zero, however, it makes the material very difficult to process and due to this it is not widely used. The behavior of each of the researched material will be discussed below:

5.1.1 Fe

After HPT deformation a crystallite size of 64 nm is obtained for room temperature deformation and 57 nm after deformation under liquid nitrogen. After heat treatment the crystallite size increases from 12% (RT) to 35% (LN) compared to respective non-heat-treated samples. This is due to large amount of energy stored in the sample during deformation. Due to this energy a modest heat treatment at 200 ^{o}C is able to increase the crystallite size. On the other hand, dislocation density decreases by about 40% after heat treatment of the HPT-deformed samples. The dislocation arrangement parameter M tells us that there are long-range strain fields after HPT deformation which are then reduced after heat treatment. It is proportional to the configuration parameter α [170]

which determines the internal stress field connected to a certain density of dislocations N (for details see Section 5.3).

After HPT deformation there is a substantial increase in the coercivity of the Fe samples. Soft magnetic properties are better when there is no hinderance to the domain wall motion. After HPT deformation there are a large number of defects and strain fields within the sample that restrict the domain wall motion, therefore, the coercivity of the samples rises sharply. The values obtained for the coercivity correspond well with the earlier research [53, 91]. After heat treatment there is a substantial decrease in the coercivity values across all frequencies. In fact, at higher frequencies (above 50 Hz) the coercivity values of the heat-treated samples are lower than the undeformed samples. HPT deformation increases the resistivity of the sample which reduces the Eddy current losses. After heat treatment there is some loss of resistivity but then there is also ease of domain wall motion due to removal of defects and strain fields which reduces the overall coercivity. Therefore, there is a competition between several factors that determine the final value of the coercivity of the sample.

Comparing HPT-deformed bulk iron samples in [90, 91] with the ones in the present research we see an 8% decrease in room temperature HPT-deformed iron samples but a 22% increase in liquid nitrogen HPT-deformed samples. Heat treatment has a very positive effect on the coercivity values as we see a 26% decrease in coercivity values in room temperature HPT-deformed iron samples while a 10% increase in liquid nitrogen HPT-deformed samples.

5.1.2 Fe-3wt%Si

Two forms of Fe-3wt%Si were processed using HPT; bulk and powder. The idea was to see whether powder material behaves any differently from the bulk form with regards to HPT processing and magnetic properties or not.

The dislocation arrangement parameter, M (Table 4.2) shows a peculiar trend in the case of Fe-3wt%Si samples where, after heat treatment, M increases except in the case of room temperature HPT-deformed powder samples. This behavior is contrary to the behavior that was observed in the case of bulk Iron samples. The same behavior is then observed in the coercivity vs. frequency behavior of Fe-3wt%Si samples as shown in Fig.

4.16, 4.17, 4.19, 4.20. After heat treatment coercivity rises instead of decreasing as was observed in the case of Iron samples. The only exception is the room temperature HPT-deformed powder samples where coercivity decreases sharply after heat treatment. It seems that heat treatment is having a reverse effect on strain fields whereby strain fields increase in the sample after heat treatment.

Crystallite size and dislocation density explains the coercivity behavior of Fe-3wt%Si samples in most cases. Comparing the crystallite size of HPT-deformed bulk Fe-3wt%Si samples, the heat-treated samples have a slightly higher crystallite size therefore we see a slightly higher coercivity value for heat treated samples. For room temperature HPT-deformed powder samples there is about 20% reduction in dislocation density. The Eddy current losses are also reduced after heat treatment. Therefore overall coercivity value is reduced in this case. For liquid nitrogen HPT-deformed powder samples there is about 60% increase in crystallite size whereas dislocation density almost remains the same. Therefore the heat-treated samples have higher coercivity compared to non-heat-treated samples.

Comparing HPT-deformed bulk Fe-3wt%Si samples in [90, 91] with the ones in the present research we see an 44% decrease in coercivity in room temperature HPT-deformed iron samples and a 34% increase in coercivity in liquid nitrogen HPT-deformed samples. Heat treatment has an inverse effect on the coercivity values as we see only a 4% decrease in coercivity values in heat treated room temperature HPT-deformed iron samples while a 29% increase in heat treated liquid nitrogen HPT-deformed samples.

5.1.3 Fe-6.5wt%Si

As in the case of Fe-3wt%Si, two forms of Fe-6.5wt%Si were processed using HPT; bulk and powder. Fe-6.5wt%Si shows somewhat mixed results when it comes to the effects of heat treatment. In bulk Fe-6.5wt%Si heat treatment increases the coercivity to some extent. This could be attributed to a decrease in resistivity due to the heat treatment. The coercivity of all samples is significantly higher in HPT-deformed samples compared to undeformed sample. Overall the coercivity is lower compared to Fe and Fe-3wt%Si samples because of the increase amount of Si.

It is also noteworthy that although the average grain size is about 70 nm as shown in Fig. 4.7 the exchange coupling may not occur to a large extent. The percentage of grains of about 20 nm size appears to be too small to significantly allow for exchange coupling.

The behavior of Fe-6.5wt%Si samples as shown in Fig. 4.22, 4.23, 4.25 and 4.26 can be explained to some extent by considering the crystallite size (Fig. 4.10) and dislocation density (Fig. 4.11). Heat treatment increases the crystallite size and correspondingly coercivity goes up. Although at the same time the dislocation density goes down but the effect of crystallite size seems dominant in this case.

Comparing room temperature HPT-deformed powder Fe-6Si samples with their heat-treated counterparts, we can see that the difference in crystallite size is minimum whereas there is a 25% reduction in dislocation density, therefore in this case the effect of dislocation density is dominant and we see a lower coercivity for heat treated samples. For the case of liquid nitrogen processed powder samples, there is a 42% increase in crystallite size and a 35% reduction in dislocation density, therefore at low frequencies the heat-treated samples have lower coercivity while at higher frequencies non-heat-treated samples show lower coercivity.

Comparing HPT-deformed bulk Fe-6.5wt%Si samples in [90, 91] with the ones in the present research we see an 18% decrease in coercivity in room temperature HPT-deformed iron samples and a 17% decrease in coercivity in liquid nitrogen HPT-deformed samples. Heat treatment has a positive effect on the coercivity values as we see a 41% decrease in coercivity values in heat treated room temperature HPT-deformed iron samples while a 21% decrease in heat treated liquid nitrogen HPT-deformed samples.

5.2 Magnetic Losses of the Fe-Si Alloys

Cumulative magnetic losses that are obtained by integrating the area of the hysteresis curve follow the same trend as the coercivity as they are interdependent. Losses shown in Fig. 4.28 to 4.30 show the drastic effect of Si addition in Iron. Static losses decrease by many-fold as the quantity of Si is increased in Iron. Classical Eddy current losses decrease

too, as Si increases resistivity. Magnetic losses also increase with the frequency. This is because Eddy current losses and Excess losses are frequency-dependent.

Compared to undeformed samples, HPT deformation increases the losses because of the domain wall pinning effect due to defects and strain fields induced by HPT deformation. Heat treatment increases or decreases losses depending on various factors such as reduction of strain fields/dislocation density, decrease in resistivity and increase in the crystallite and/or grain size of the deformed material. The average grain size as shown in Fig. 4.7 is about 70 nm which seems to increase a bit after heat treatment as shown in Fig. 4.8. Fig. 4.9 shows grains that are 20 nm in size. Such grains would contribute to exchange coupling but their percentage is small. So the final losses are an average of all these factors combined.

5.3 Internal Stress Calculations

Two methods have been employed to estimate internal stresses of the samples. First method is through the use of magnetic data according to Eq. 5.1 [54, 91].

$$\boldsymbol{H_c = \lambda\sigma/\mu_o M_s} \qquad \text{Eq. 5.1}$$

where:

H_c is the coercivity at 0 Hz

λ is the magnetostriction

σ is the internal stress

M_s is the saturation magnetization

μ_o is the permeability

The internal stresses can also be estimated (at least to some part, i.e., the internal stresses of 3rd order, see Section 5.3.2) from the dislocation density, and the dislocation configuration parameter α, by using the following equations:

$$\boldsymbol{G = E/2(1+v)} \qquad \text{Eq. 5.2}$$

$$\boldsymbol{\tau_{CRSS} = \alpha G b N^{1/2}} \qquad \text{Eq. 5.3}$$

$$\boldsymbol{\sigma = 2.75\, \tau_{CRSS}} \qquad \text{Eq. 5.4}$$

where:

G = shear modulus

E = Young's modulus obtained from nanoindentation data

ν = Poisson's ratio

τ_{CRSS} = critical resolved shear stress

α = configuration parameter describing the stress field intensity of a given dislocation arrangement and dislocation density.

b = Burgers vector

N = dislocation density

σ = internal stress

The factor 2.75 in Eq. 5.4 is used for bcc materials and is taken from [173].

5.3.1 Calculations of Internal Stresses from Magnetic Data

Table 5.1 shows stress calculations by using the extrapolated 0 Hz coercivity values of the materials under investigation. The same calculations are done by Grössinger et. al. [53] with the same materials under different processing conditions. The constant values of magnetostriction λ, saturation magnetization M_s and μ_o in Eq. 5.1 are incorporated into factor f (i.e., $f = \lambda/\mu_o M_s$) also listed in Table 5.1. For each material these values are taken from [53]; they are constants for a particular material. The values of internal stress σ listed in column 3 were calculated from the measured values of extrapolated 0 Hz-coercivity H_c for each sample.

Fig. 5.1 shows a graphical representation of the values given in Table 5.1. For a given material, Eq. 5.1 states that coercivity H_c is directly proportional to stress as all other parameters are constants for a material.

The results in Fig. 5.1 show a higher stress in pure bulk Fe compared to Fe-Si alloys. For some samples such as heat-treated Fe-3wt%Si bulk and powder samples that are HPT-deformed at room temperature, the value of internal stress is higher than their non-heat-treated counterparts.

Table 5.1: Internal stresses calculated from the magnetic data

Sample	H_c	f	σ
Fe(b)_HPT_RT	1713	6.510424	263
Fe(b)_HPT_RT_HT	1379	6.510424	212
Fe(b)_HPT_LN	1548	6.510424	238
Fe(b)_HPT_LN_HT	1391	6.510424	214
Fe-3wt%Si(b)_HPT_RT	388	4.282674	91
Fe-3wt%Si(b)_HPT_RT_HT	667	4.282674	156
Fe-3wt%Si(b)_HPT_LN	383	4.282674	89
Fe-3wt%Si(b)_HPT_LN_HT	497	4.282674	116
Fe-3wt%Si(p)_HPT_RT	582	4.282674	136
Fe-3wt%Si(p)_HPT_RT_HT	831	4.282674	194
Fe-3wt%Si(p)_HPT_LN	586	4.282674	137
Fe-3wt%Si(p)_HPT_LN_HT	584	4.282674	136
Fe-6.5wt%Si(b)_HPT_RT	379	4.523001	84
Fe-6.5wt%Si(b)_HPT_RT_HT	273	4.523001	60
Fe-6.5wt%Si(b)_HPT_LN	320	4.523001	71
Fe-6.5wt%Si(b)_HPT_LN_HT	303	4.523001	67
Fe-6.5wt%Si(p)_HPT_RT	368	4.523001	81
Fe-6.5wt%Si(p)_HPT_RT_HT	297	4.523001	66
Fe-6.5wt%Si(p)_HPT_LN	382	4.523001	85
Fe-6.5wt%Si(p)_HPT_LN_HT	95	4.523001	21

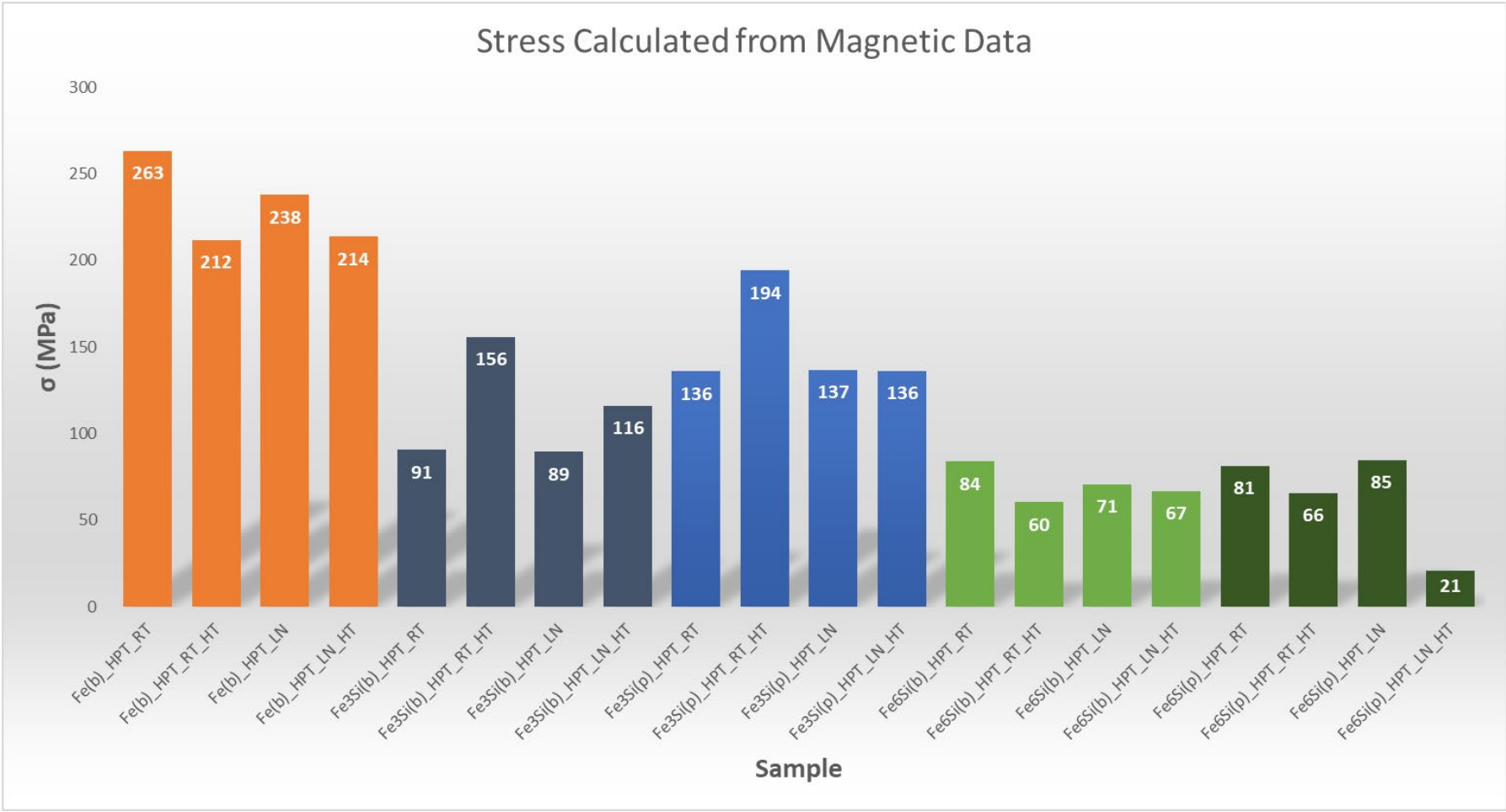

Figure 5.1: Internal stress calculated from the magnetic data.

5.3.2 Stress Calculations from Dislocation Data

As already mentioned in the preamble of Section 5.3, there is another possibility to conclude the internal stresses, i.e., from the dislocation density data obtained through X-ray line profile analysis (XLPA). These calculations were made by using Eq. 5.2 to Eq. 5.4 that are found in books on mechanical metallurgy. Fig. 5.2 shows the results of such calculations. Using the values of dislocation densities given in Fig. 4.11, and assuming that for high strains achieved by HPT the configuration parameter α is about 0.1 [2], one receives the values of internal stress σ listed in Table 5.2. Fig. 5.2 shows a graphical representation of these values. In contrast to the derivation from magnetic quantities, the values of internal stress in pure bulk Fe are lower than the values in Fe-Si alloys and, above all, in all cases the heat treatment lowers the internal stresses produced by the HPT treatment. The powder versions of Fe-Si alloys show higher stress values because the powder particles get some internal stresses during production which the bulk alloys during casting would not. In summation, the internal stress values calculated from the measured dislocation densities by assuming always the same dislocation arrangement appear more plausible than the ones derived from the magnetic data.

Table 5.2: Internal stresses calculated from the dislocation density data using a constant dislocation configuration parameter α.

Sample	Dislocation Density, N	ν	E	G	α	b	$N^{1/2}$	τ_{CRSS}	σ
	10^{15} m^{-2}		GPa	MPa		10^{-10} m	10^{7}	MPa	MPa
Fe(b)_HPT_RT	2.83	0.30	222	85385	0.10	2.48	5.32	113	310
Fe(b)_HPT_RT_HT	1.69	0.30	222	85385	0.10	2.48	4.11	87	239
Fe(b)_HPT_LN	2.84	0.30	222	85385	0.10	2.48	5.33	113	310
Fe(b)_HPT_LN_HT	1.72	0.30	222	85385	0.10	2.48	4.15	88	242
Fe-3wt%Si(b)_HPT_RT	3.22	0.30	210	80769	0.10	2.47	5.67	113	311
Fe-3wt%Si(b)_HPT_RT_HT	2.80	0.30	210	80769	0.10	2.47	5.29	106	290
Fe-3wt%Si(b)_HPT_LN	3.52	0.30	210	80769	0.10	2.47	5.93	118	325
Fe-3wt%Si(b)_HPT_LN_HT	2.56	0.30	210	80769	0.10	2.47	5.06	101	278
Fe-3wt%Si(p)_HPT_RT	6.12	0.30	210	80769	0.10	2.47	7.82	156	429
Fe-3wt%Si(p)_HPT_RT_HT	4.91	0.30	210	80769	0.10	2.47	7.01	140	384
Fe-3wt%Si(p)_HPT_LN	5.80	0.30	210	80769	0.10	2.47	7.62	152	418
Fe-3wt%Si(p)_HPT_LN_HT	5.70	0.30	210	80769	0.10	2.47	7.55	151	414
Fe-6.5wt%Si(b)_HPT_RT	4.60	0.30	208	80000	0.10	2.46	6.78	133	367
Fe-6.5wt%Si(b)_HPT_RT_HT	4.06	0.30	208	80000	0.10	2.46	6.37	125	345
Fe-6.5wt%Si(b)_HPT_LN	4.95	0.30	208	80000	0.10	2.46	7.04	138	381
Fe-6.5wt%Si(b)_HPT_LN_HT	4.58	0.30	208	80000	0.10	2.46	6.77	133	366
Fe-6.5wt%Si(p)_HPT_RT	8.58	0.30	208	80000	0.10	2.46	9.26	182	501
Fe-6.5wt%Si(p)_HPT_RT_HT	6.45	0.30	208	80000	0.10	2.46	8.03	158	435
Fe-6.5wt%Si(p)_HPT_LN	7.75	0.30	208	80000	0.10	2.46	8.8	173	476
Fe-6.5wt%Si(p)_HPT_LN_HT	5.03	0.30	208	80000	0.10	2.46	7.09	140	384

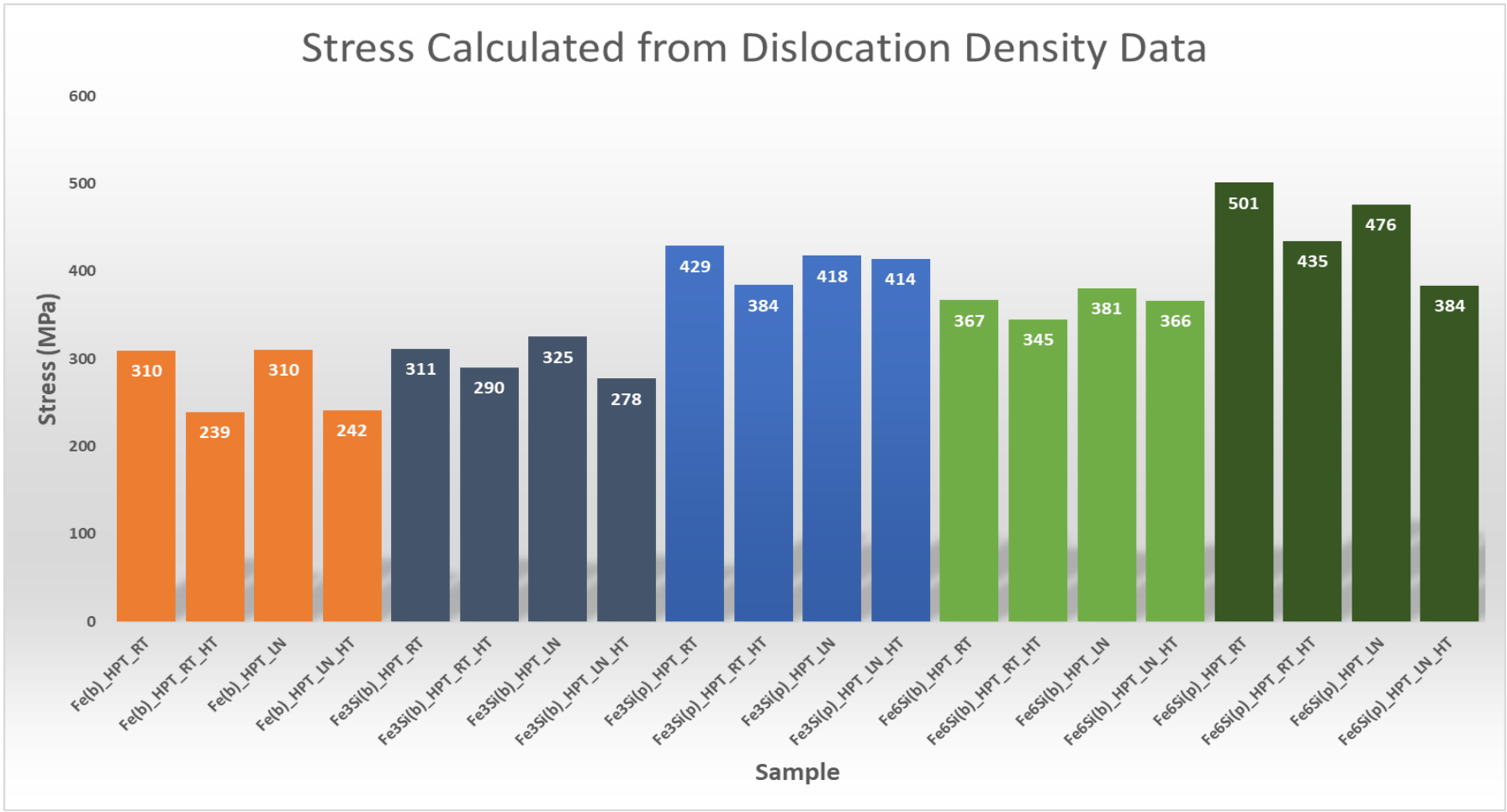

Figure 5.2: Internal stress calculated from the dislocation density data using a constant dislocation configuration parameter α.

However, while comparing the internal stresses calculated from dislocations shown in Table 5.2 and Fig. 5.2, with those calculated from the magnetic data in Table 5.1 and Fig. 5.1, most of their absolute values are higher. Trying a more careful considerations of the internal stresses according to E. Macherauch (see, e.g., [174]), one should distinguish several types of internal stresses where those from dislocations represent the very local 3rd order stresses; besides 1st order internal stresses (i.e., macroscopic internal stresses) which extend the scale of the grains and are caused by external asymmetric forces on the sample, as well as 2nd order stresses (i.e., misorientation between grains) exist. If one accepts the validity of Eq. 5.1, all three types of internal stresses may contribute to the values of internal stresses calculated by Eq. 5.1; therefore those values appear as an upper possible limit. In order to better account for that limit than the data in Table 5.2 and Fig. 5.2, and also to take the occasion to use the M parameter measured by the XLPA method as this allows to derive real and specific values of the dislocation configuration parameter α, another calculation of the dislocation internal stresses was tried. According to T. Ungar [170], M is proportional to α, M = c * α, with a constant factor c that depends on the material being considered. Table 5.3 shows the calculation of stress values that are corrected by M-values obtained by XLPA (see Table 4.2), with c = 61 chosen in order to roughly keep to the upper limit mentioned, and not to receive unrealistic α values.

Comparing the correlation of corrected dislocation stress with the coercivity we can see that in 70 % of all cases, the H_c is correlated with the stresses caused from dislocations. For the 30% uncorrelated cases, it is not the abnormal growth of crystallites which causes the deviation as can be seen in Fig. 4.10. Rather, it can be argued that some part of internal stresses can come from sources other than dislocations, i.e., 2nd order internal stresses from misorientations between the grains, or even 1st order internal stresses, i.e., macroscopic internal stresses which extend the scale of grains and are caused by external asymmetric forces on the sample. It should be mentioned that all values presented in Section 5.3 appear realistic as they do not get larger than the external UTS values derived from the measured hardness data. Those can be gained by dividing the hardness data by a factor of 3.06 at least for the case of steel.

Table 5.3: Internal stresses calculated from the dislocation density data using variable α-values derived from measured parameter M.

Sample	Dis. stress σ (α=0.1=const)	M	α=M/61	G	Dislocation Stress (Corrected)	H_c	Quality of Simulation regarding parallelity of dis. stress to H_c
	MPa			MPa	MPa	A/m	
Fe(b)_HPT_RT	310	5.5	0.090	85385	280	1712	good
Fe(b)_HPT_RT_HT	239	1.3	0.021	85385	51	1379	good
Fe(b)_HPT_LN	310	5.4	0.089	85385	274	1548	good
Fe(b)_HPT_LN_HT	242	0.5	0.0008	85385	20	1391	good
Fe-3wt%Si(b)_HPT_RT	311	2.8	0.046	80769	143	388	good
Fe-3wt%Si(b)_HPT_RT_HT	290	4.0	0.066	80769	190	667	good
Fe-3wt%Si(b)_HPT_LN	325	0.16	0.003	80769	9	383	bad
Fe-3wt%Si(b)_HPT_LN_HT	278	0.08	0.001	80769	4	497	bad
Fe-3wt%Si(p)_HPT_RT	429	5.2	0.085	80769	366	582	bad
Fe-3wt%Si(p)_HPT_RT_HT	384	4.1	0.067	80769	258	831	bad
Fe-3wt%Si(p)_HPT_LN	418	0.3	0.005	80769	21	585	bad
Fe-3wt%Si(p)_HPT_LN_HT	414	5.8	0.095	80769	394	583	bad
Fe-6.5wt%Si(b)_HPT_RT	367	11	0.180	80000	662	379	good
Fe-6.5wt%Si(b)_HPT_RT_HT	345	0.4	0.007	80000	23	273	good
Fe-6.5wt%Si(b)_HPT_LN	381	3.2	0.052	80000	200	320	good
Fe-6.5wt%Si(b)_HPT_LN_HT	366	1.2	0.020	80000	72	303	good
Fe-6.5wt%Si(p)_HPT_RT	501	6.1	0.100	80000	501	368	good
Fe-6.5wt%Si(p)_HPT_RT_HT	435	4.2	0.069	80000	300	297	good
Fe-6.5wt%Si(p)_HPT_LN	476	1.2	0.020	80000	94	382	good
Fe-6.5wt%Si(p)_HPT_LN_HT	384	1.0	0.016	80000	63	95	good

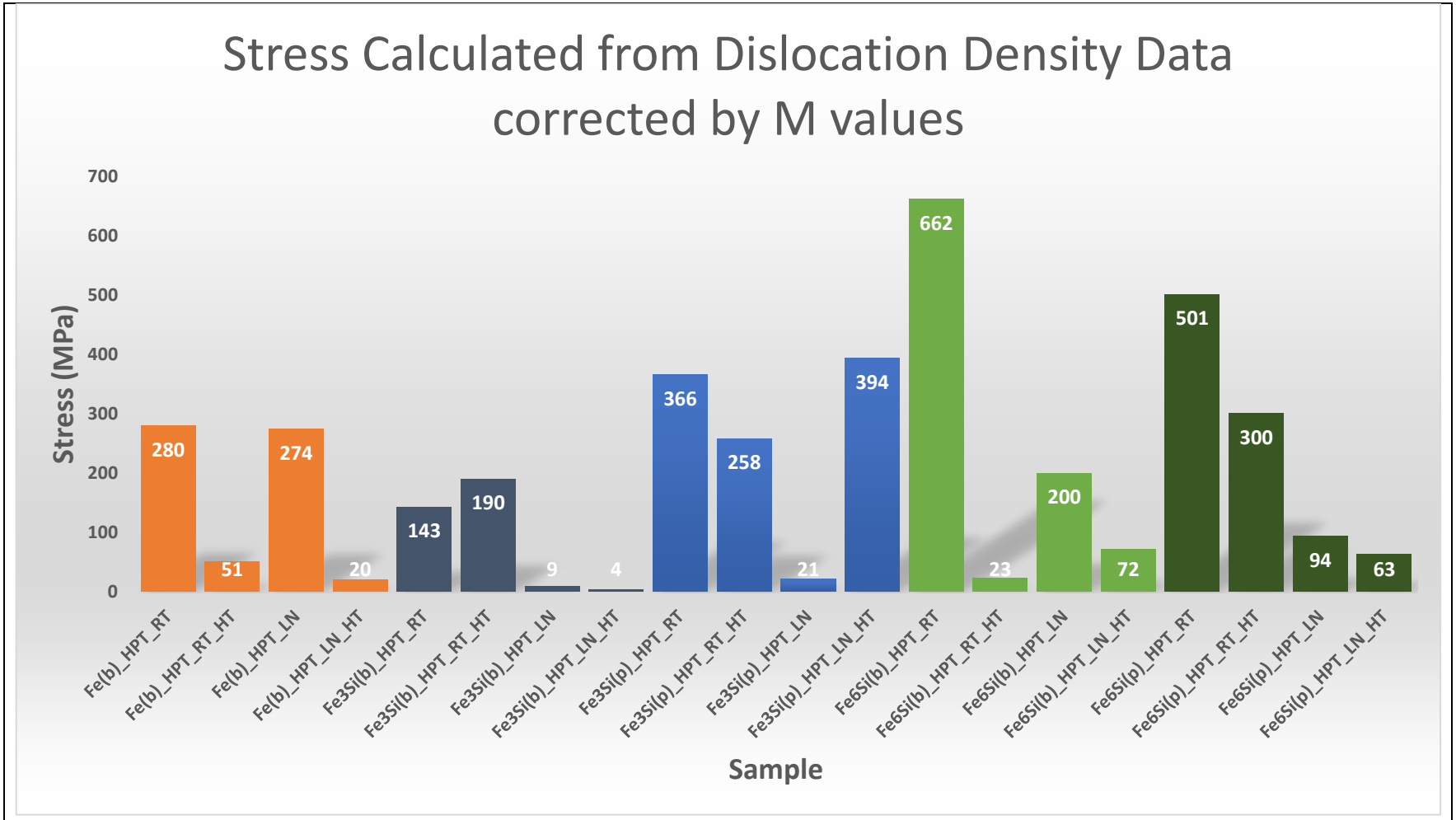

Figure 5.3: Internal stress calculated from the dislocation density data using variable α-values derived from measured parameter M.

5.4 Dependence of Coercivity on Crystallite Size

Herzer plots [55, 63, 67] are famous graphs between coercivity and grain size that show a D^6-dependence (or D^3-dependence in some cases) between the coercivity and grain size. It should be noted that D^6 part of the graph in [55, 63] is made by amorphous alloys or nanocrystalline alloys where nanocrystals are grown within the amorphous matrix by appropriate heat treatments. In contrast to that, the 1/D part of the graph is valid for materials whose grain size ranges from roughly 100 nm to mm size. In both cases, therefore, the internal stresses are minimum. In case of SPD-processed materials, however, a very high dislocation density along with very high internal stresses are generated. Grössinger et. al. [5, 53] plotted a similar plot for HPT-deformed materials and found significant deviations from the D^6 law. In the present research, a similar approach is taken but with crystallite or subgrain size that is obtained through X-ray line profile analysis (XLPA). This means that the macroscopic uniaxial anisotropies may dominate over the magnetic anisotropy. For this case, Herzer recently designed an extension of the above model (n = 6) which predicts a distinctly lower exponent (n = 3) [66]. That is why we fitted the plots with the subgrain sizes by the equation $y = a * x^n$ and checked the situation for the resulting value of n. The prefactor a is some combination of $p_c K_1^a/J_s.A^b$ as is given in Eq. 2.9 (from Herzer's plots).

Fig. 5.3 shows the graph of coercivity H_c vs. crystallite size D, for HPT-deformed materials while Fig. 5.4 shows that of coercivity H_c vs. crystallite size D, for HPT-deformed materials that are followed by heat treatment.

As is evident from the results, the coercivity follows a $D^{1.5}$ - dependency in case of HPT-deformed materials, and regression value is excellent ($R^2 = 0.96$) in this case. In case of HPT + HT materials, as shown in Fig. 5.4, the coercivity shows a $D^{1.47}$ - dependency and the regression value is a little lower but still acceptable ($R^2 = 0.63$) when this is compared with several analogous plots of Herzer. This can be explained by the broader size distribution of subgrain size resulting from the heat treatment; obviously, the subgrains underwent a heterogeneous growth during the heat treatment. Another hint that all the fits are reliable is the absolute value of prefactor 'a' which is near to 3 A/m which is also the case with Herzer's plots when $n < 6$ [66].

In any case, the results, in general, point towards a decrease in coercivity values with decreasing crystallite size. This shows that the phenomenon of exchange interaction is operative over here. This also indicates that crystallite or subgrain size (especially in as-deformed samples) is the relevant structural element and not the highly misoriented grains, which would – in this work - give an increase in coercivity and not a decrease.

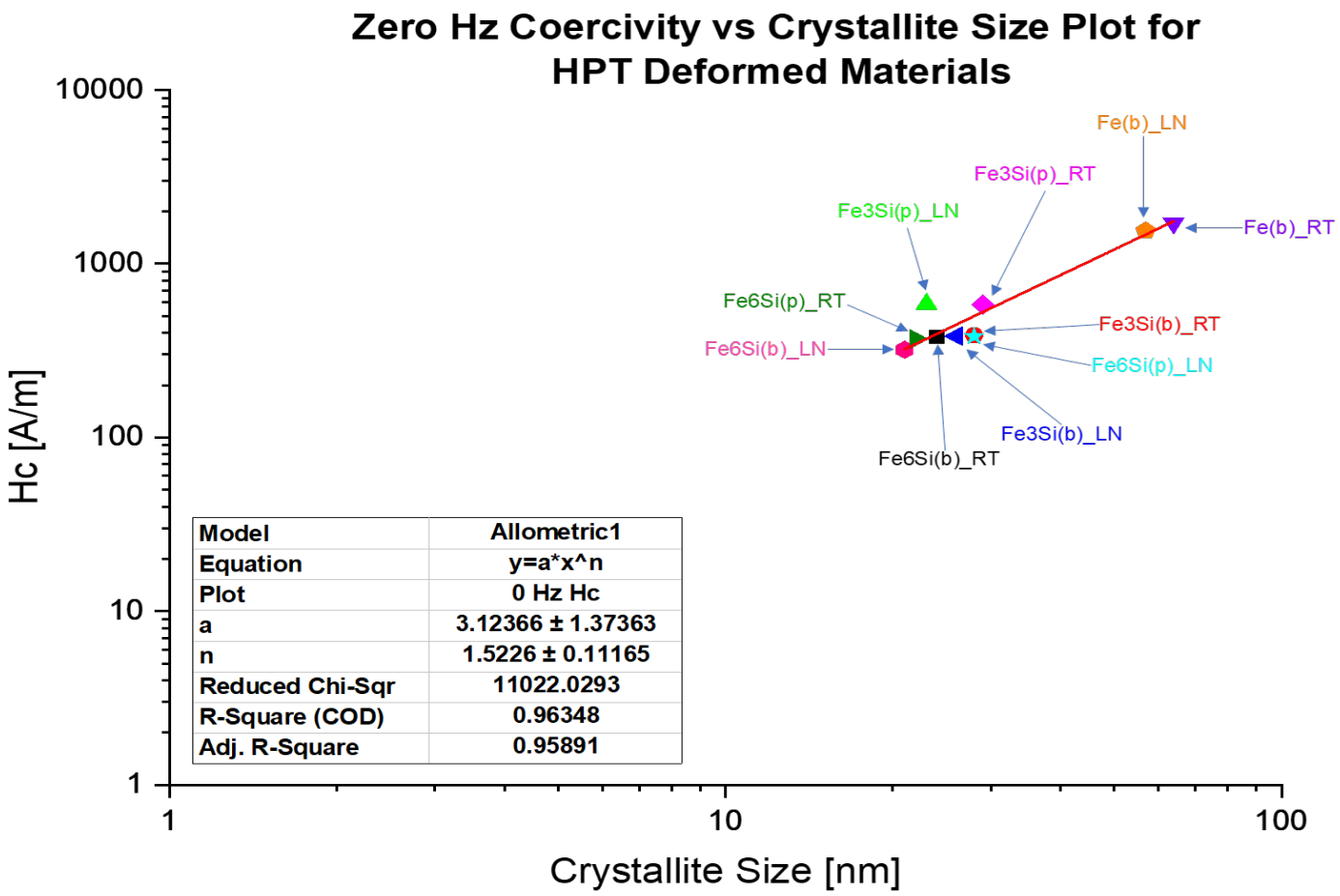

Figure 5.3: Zero Hz Coercivity vs Crystallite Size plot for all HPT-deformed samples showing a power law dependency of 1.5 with the crystallite size.

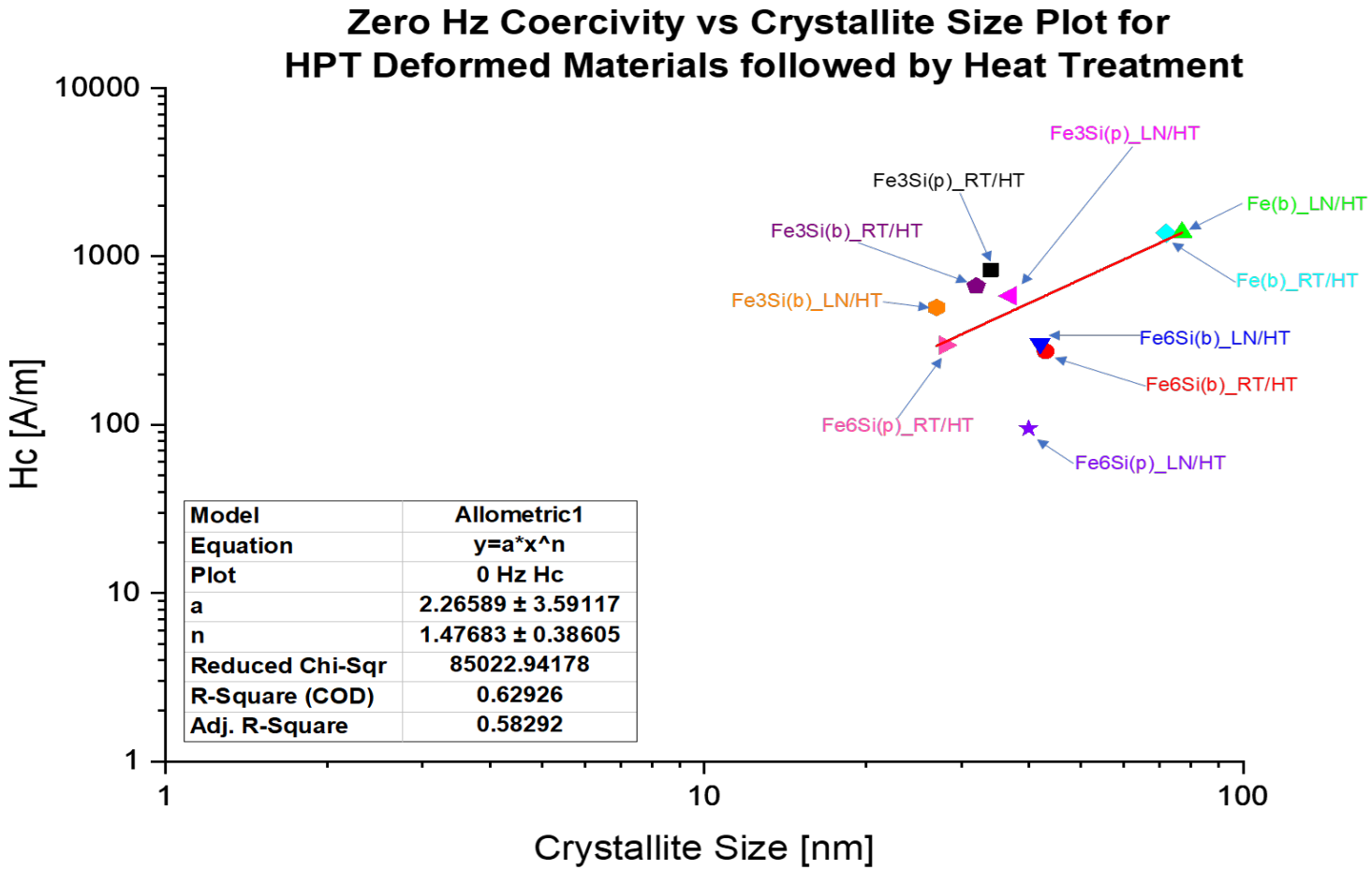

Figure 5.4: Zero Hz Coercivity vs Crystallite Size plot for all HPT-deformed samples followed by Heat Treatment showing a power law dependency of 1.47 with the crystallite size.

5.5 Amorphous and Nanocrystalline FINEMET Alloys

Amorphous and nanocrystalline FINEMET alloys were in the form of 20 μm thin foils. Amorphous FINEMET is more ductile than the nanocrystalline FINEMET which is as brittle as a thin sheet of glass. Both materials show microcracks after HPT deformation. Lowering the processing temperature and increasing the amount of deformation (i.e., higher number of rotations and higher pressure) seems to reduce these cracks to some extent in amorphous FINEMET. However, nanocrystalline FINEMET is far too brittle to be processed by HPT without producing cracks.

Additionally, no amorphous to nanocrystalline or nanocrystalline to amorphous transition was observed after HPT deformation. This is both confirmed by DSC and XRD graphs. It is possible that there may be some nanocrystallization on the surface of the amorphous samples after HPT deformation. However, the samples in this research were finely polished before any further testing. These samples were also about 0.5 mm thick and after grinding/polishing the final thickness is close to 0.3 mm. In unpublished results by another colleague some nanocrystallization was observed, however, those samples are 0.2 mm thick which means they have much higher deformation than the samples in this research.

Chapter 6: Summary, Conclusions, Future Work

Summary

Soft magnetic alloys such as Fe, Fe-3wt%Si, Fe-6.5wt%Si and VITROPERM (both amorphous and nanocrystalline) were deformed by high pressure torsion (HPT). The samples were deformed at room temperature and liquid nitrogen temperature. Extensive microstructural investigations have been done, in parallel to the measurements of soft magnetic properties such as coercivity H_c, losses P/f at 5-200 Hz, and the permeability μ. Emphasis in investigations and analyses was given to the measurements and analysis of static magnetic properties. For Fe-Si alloys the idea was to get a grain size where exchange interaction becomes operative, inducing a decrease of coercivity with decreasing grain size. The final goal was to achieve best possible soft magnetic properties from HPT-deformed samples. Internal stresses, e.g., produced by HPT are known to deteriorate soft magnetic properties, therefore, to reduce internal stresses without increasing the grain size a mild heat treatment was devised. Subgrain size and dislocation density were determined through X-ray Line Profile Analysis (XLPA) while magnetic properties were determined using a hysteresisgraph.

Conclusions

- The coercivity of Fe and Fe-Si alloys generally increased after HPT deformation due to internal stresses produced during the process.
- Heat treatment after HPT deformation shows a lowering of coercivity in 70% of all cases.
- The size of grains with high misorientations (larger than 2-3 degrees) is larger than about 70 nm where exchange coupling should not occur. However, the results show that coercivity is rather governed by the crystallite size (D), as well as the density (N) and arrangement of dislocations (M resp. α).
- The changes of quantities H_c and P/f were found to be in parallel, but there was no correlation of those to the changes in permeability (μ). There are clear correlations of them with the crystallite size (D), the dislocation density (N), and the arrangement

of dislocations (α): when D, N or α decreased, so did H_c and P/f. Because HPT-processing alone did not achieve decrease of D without increasing N, thermal treatments were applied which indeed could decrease N with only slight increase of D, and which indeed led to decrease of H_c and P/f. Also the arrangement of dislocations (α, M) led to the decrease of H_c and P/f at least as far as the other two quantities did not increase too much.

- The relative permeability decreases after HPT deformation except in the case of pure Iron samples. Heat treatment after HPT deformation generally improves relative permeability.
- Internal stress calculations on the basis of dislocation plasticity theory, using measured data of dislocation density and arrangement come close to the internal stresses derived from the measured magnetic data.
- Analysis of the coercivity measurements shows that they follow a $D^{1.5}$ – law with the crystallite (subgrain) size (D) in case of HPT-deformed materials, and a $D^{1.47}$ – relation in case of HPT+HT materials. This means that subgrains are a better representation of the structural elements compared to high misorientation grains what concerns the operation of exchange interaction mechanism because of two reasons: (i) the values of H_c increase with increasing grain size, (ii) the H_c/D dependence is closer to predictions of Herzer for small-angle misoriented grains (i.e., subgrains) that the exponent of D shrinks to a maximum value of 3, in contrast to being 6 for high-angle misoriented grains.
- Amorphous and nanocrystalline FINEMET samples show microcracking after HPT deformation. Lower processing temperature, higher pressure and a greater number of rotations improve the quality of the samples, however, a lot of microcracks still remain in the samples.
- No amorphous to nanocrystalline or nanocrystalline to amorphous transition was observed in FINEMET samples under the conditions used in this research.

Future Work

- As heat treatment at 200 ^{o}C seems to increase the grain/crystallite size slightly therefore a lower temperature down to 125 ^{o}C (representing the vacancy annealing = dislocation rearrangement temperature) should be tested to reduce the internal stresses only.
- Cyclic HPT deformation should be tried to see whether it reduces the crystallite size and/or the internal stresses without heat treatment.
- For VITROPERM samples a modification in HPT equipment that allows for slow increase and decrease of pressure may result in better quality samples.
- Magnetic characterization of VITROPERM samples still needs to be done.
- A higher pressure and/or higher number of rotations may induce crystallization in amorphous VITROPERM samples which would obviate the need for heat treatment to induce nanocrystallization.
- More checks of the H_c/D relation are recommended to further establish the exponent value 1.5 and find the reasons for the deviations.

References

1. Zehetbauer, M.J., et al., *The Role of Hydrostatic Pressure in Severe Plastic Deformation*, in *Nanomaterials by Severe Plastic Deformation*. 2003, Wiley-VCH Verlag GmbH & Co. p. 433-446.
2. Zehetbauer, M.J., et al., *The Role of Hydrostatic Pressure in Severe Plastic Deformation.* Advanced Engineering Materials, 2003. **5**(5): p. 330-337.
3. Valiev, R., et al., *Producing bulk ultrafine-grained materials by severe plastic deformation.* JOM, 2006. **58**(4): p. 33-39.
4. Zehetbauer, M.J. and Y.T. Zhu, *Bulk nanostructured materials*. 2009: John Wiley & Sons.
5. Zehetbauer, M., et al., *Bulk Nanostructured Functional Materials By Severe Plastic Deformation.* Advanced Engineering Materials, 2010. **12**(8): p. 692-700.
6. Estrin, Y. and A. Vinogradov, *Extreme grain refinement by severe plastic deformation: A wealth of challenging science.* Acta Materialia, 2013. **61**(3): p. 782-817.
7. Azushima, A., et al., *Severe plastic deformation (SPD) processes for metals.* CIRP Annals - Manufacturing Technology, 2008. **57**(2): p. 716-735.
8. Zhilyaev, A.P. and T.G. Langdon, *Using high-pressure torsion for metal processing: Fundamentals and applications.* Progress in Materials Science, 2008. **53**(6): p. 893-979.
9. Abrosimova, G.E., et al., *Nanocrystallization of an amorphous Fe80B20 alloy during severe plastic deformation.* Physics of the Solid State, 2007. **49**(6): p. 1034-1039.
10. Li, W., et al., *Nanocrystallization and magnetic properties of amorphous Nd9Fe85B6 subjected to high-pressure torsion deformation upon annealing.* Journal of Applied Physics, 2008. **104**(2): p. 023912.
11. Csach, K., J. Miskuf, and A. Jurikova, *Nanocrystallization of Finemet alloy after intensive plastic deformation.* Journal of Physics: Conference Series, 2010. **200**(8): p. 082002.
12. Beyerlein, I.J. and L.S. Tóth, *Texture evolution in equal-channel angular extrusion.* Progress in Materials Science, 2009. **54**(4): p. 427-510.
13. Edalati, K. and Z. Horita, *A review on high-pressure torsion (HPT) from 1935 to 1988.* Materials Science and Engineering: A, 2016. **652**: p. 325-352.
14. El-Garaihy, W.H., D.M. Fouad, and H.G. Salem, *Multi-channel Spiral Twist Extrusion (MCSTE): A Novel Severe Plastic Deformation Technique for Grain Refinement.* Metallurgical and Materials Transactions A, 2018. **49**(7): p. 2854-2864.
15. Weeber, A.W. and H. Bakker, *Amorphization by ball milling. A review.* Physica B: Condensed Matter, 1988. **153**(1): p. 93-135.
16. Langdon, T., *Seventy-five years of superplasticity: historic developments and new opportunities.* Journal of Materials Science, 2009. **44**(22): p. 5998-6010.
17. Kawasaki, M. and T. Langdon, *Review: achieving superplastic properties in ultrafine-grained materials at high temperatures.* Journal of Materials Science, 2015: p. 1-14.

18. Nieh, T.-G., J. Wadsworth, and O.D. Sherby, *Superplasticity in Metals and Ceramics*. 2005: Cambridge University Press, New York.
19. Padilla, H.A., II and B.L. Boyce, *A Review of Fatigue Behavior in Nanocrystalline Metals.* Experimental Mechanics, 2010. **50**(1): p. 5-23.
20. Furuta, T., et al., *Ultrahigh strength of nanocrystalline iron-based alloys produced by high-pressure torsion.* Journal of Materials Science, 2010. **45**(17): p. 4745-4753.
21. Gennadii, A.M., *Strength and plasticity of nanocrystalline materials and nanosized crystals.* Physics-Uspekhi, 2011. **54**(11): p. 1091.
22. Abramova, M., et al., *Thermal stability and extra-strength of an ultrafine grained stainless steel produced by high pressure torsion.* Reviews on Advanced Materials Science, 2015. **43**: p. 83-88.
23. Valiev, R.Z. and Y. Zhu, *Recent Findings in Superior Strength and Ductility of Ultrafine-Grained Materials.* Transactions of the Materials Research Society of Japan, 2015. **40**(4): p. 309-318.
24. Abrosimova, G. and A. Aronin, *The increase of strength properties at nanocrystal formation.* Materials Letters, 2017. **206**: p. 64-66.
25. Karavaeva, M., et al., *High-strength state of ultrafine-grained martensitic steel produced by high pressure torsion.* IOP Conference Series: Materials Science and Engineering, 2017. **179**(1): p. 012037.
26. Kawasaki, M., et al., *Strengthening of metals through severe plastic deformation.* Rev. Adv. Mater. Sci, 2017. **48**: p. 13-24.
27. Valiev, R.Z. and I.V. Alexandrov, *Development of severe plastic deformation techniques for the fabrication of bulk nanostructured materials.* Annales de Chimie Science des Matériaux, 2002. **27**(3): p. 3-14.
28. Glezer, A.M., A.A. Tomchuk, and T.V. Rassadina, *Effect of reversible torsion on the structure and mechanical properties of iron under severe plastic deformations in a Bridgman camera.* Doklady Physics, 2016. **61**(2): p. 61-63.
29. Alexandrov, I.V. and R.Z. Valiev, *Nanostructures from severe plastic deformation and mechanisms of large-strain work hardening.* Nanostructured Materials, 1999. **12**(5–8): p. 709-712.
30. Pippan, R., et al., *The limits of refinement by severe plastic deformation.* Advanced Engineering Materials, 2006. **8**(11): p. 1046-1056.
31. Wei, Q., et al., *Microstructure and mechanical properties of super-strong nanocrystalline tungsten processed by high-pressure torsion.* Acta Materialia, 2006. **54**(15): p. 4079-4089.
32. Lee, S., K. Edalati, and Z. Horita, *Microstructures and Mechanical Properties of Pure V and Mo Processed by High-Pressure Torsion.* Materials Transactions, 2010. **51**(6): p. 1072-1079.
33. Lee, S. and Z. Horita, *High-Pressure Torsion for Pure Chromium and Niobium.* Materials Transactions, 2012. **53**(1): p. 38-45.
34. Y. Cao, M.K., Y. B. Wang, S. N. Alhajeri, X. Z. Liao, W. L. Zheng, S. P. Ringer, Y. T. Zhu, T. G. Langdon, *Unusual macroscopic shearing patterns observed in metals processed by high-pressure torsion.* Journal of Materials Science, 2010. **45**(17): p. 4545-4553.
35. Edalati, K., et al., *Ultra-severe plastic deformation: Evolution of microstructure, phase transformation and hardness in immiscible magnesium-based systems.* Materials Science and Engineering: A, 2017. **701**: p. 158-166.

36. Scheriau, S., et al., *Deformation mechanisms of a modified 316L austenitic steel subjected to high pressure torsion.* Materials Science and Engineering: A, 2011. **528**(6): p. 2776-2786.
37. Companhoni, M., et al., *Analysis of microstructure and microhardness of Zr-2.5Nb processed by High-Pressure Torsion (HPT).* Journal of Materials Science, 2012. **47**(22): p. 7835-7840.
38. Ikoma, Y., et al., *Phase transformation and nanograin refinement of silicon by processing through high-pressure torsion.* Applied Physics Letters, 2012. **101**(12): p. 121908.
39. Gubicza, J., et al., *Microstructure, phase composition and hardness evolution in 316L stainless steel processed by high-pressure torsion.* Materials Science and Engineering: A, 2016. **657**: p. 215-223.
40. Feng, B., V.I. Levitas, and M. Kamrani, *Coupled strain-induced alpha to omega phase transformation and plastic flow in zirconium under high pressure torsion in a rotational diamond anvil cell.* Materials Science and Engineering: A, 2018. **731**: p. 623-633.
41. Edalati, K., et al., *Allotropic phase transformation of pure zirconium by high-pressure torsion.* Materials Science and Engineering: A, 2009. **523**(1-2): p. 277-281.
42. Vorhauer, A. and R. Pippan, *On the homogeneity of deformation by high pressure torsion.* Scripta Materialia, 2004. **51**(9): p. 921-925.
43. Sundeev, R.V., A.M. Glezer, and A.V. Shalimova, *Are the abilities of crystalline alloys to amorphization upon melt quenching and severe plastic deformation identical or different?* Materials Letters, 2016. **175**: p. 72-74.
44. Antoshina, I., et al., *Crystallization of metallic glasses after severe plastic deformation.* KnE Materials Science, 2017. **3**(3): p. 435-439.
45. Sundeev, R.V., et al., *Structural Aspects of Deformational Amorphization of Ti50Ni25Cu25 Crystalline Alloy under High Pressure Torsion.* Physics of the Solid State, 2018. **60**(6): p. 1168-1172.
46. Edalati, K. and Z. Horita, *High-pressure torsion of pure metals: Influence of atomic bond parameters and stacking fault energy on grain size and correlation with hardness.* Acta Materialia, 2011. **59**(17): p. 6831-6836.
47. Edalati, K., et al., *Significance of temperature increase in processing by high-pressure torsion.* Materials Science and Engineering: A, 2011. **528**(24): p. 7301-7305.
48. Zhu, Y.T., X.Z. Liao, and X.L. Wu, *Deformation twinning in nanocrystalline materials.* Progress in Materials Science, 2012. **57**(1): p. 1-62.
49. Straumal, B.B., et al., *Phase transitions induced by severe plastic deformation: steady-state and equifinality.* International Journal of Materials Research, 2015. **106**(7): p. 657-664.
50. Edalati, K., et al., *Effect of temperature rise on microstructural evolution during high-pressure torsion.* Materials Science and Engineering: A, 2018. **714**: p. 167-171.
51. Tomchuk, A.M.G.a.A.A., *The cause of high-angle boundaries formation at the severe plastic deformation of crystals: Deformation fragmentation or dynamic recrystallization.* Rev Adv Mater Sci, 2016. **45**: p. 9-15.

52. Callister, W.D., *Materials Science and Engineering - An Introduction*. 9 ed. 2013: John Wiley & Sons NY.
53. Groessinger, R., et al., *Frequency Dependence of the Coercivity of Soft Magnetic Materials.* Magnetics, IEEE Transactions on, 2012. **48**(4): p. 1473-1476.
54. Grössinger, R., N. Mehboob, and M. Zehetbauer, *Frequency behaviour of SPD treated soft magnetic materials.* IOP Conference Series: Materials Science and Engineering, 2014. **60**(1): p. 012019.
55. Herzer, G., *Modern soft magnets: Amorphous and nanocrystalline materials.* Acta Materialia, 2013. **61**(3): p. 718-734.
56. Vorhauer, A., et al., *Magnetic Properties and Microstructure of a FeCo Ferritic Steel after Severe Plastic Deformation.* Materials Science Forum, 2006. **503**: p. 299-304.
57. Leslie-Pelecky, D.L. and R.D. Rieke, *Magnetic Properties of Nanostructured Materials.* Chemistry of Materials, 1996. **8**(8): p. 1770-1783.
58. Bertotti, G., *Hysteresis in magnetism: for physicists, materials scientists, and engineers*. 1998: Academic press.
59. Livingston, J., *A review of coercivity mechanisms.* Journal of Applied Physics, 1981. **52**(3): p. 2544-2548.
60. Alben, R., J. Becker, and M. Chi, *Random anisotropy in amorphous ferromagnets.* Journal of applied physics, 1978. **49**(3): p. 1653-1658.
61. Sarkar, D., et al., *Crystal field in amorphous rare-earth-iron alloys.* Physical Review Letters, 1974. **32**(10): p. 542.
62. Herzer, G., *Grain structure and magnetism of nanocrystalline ferromagnets.* IEEE Transactions on Magnetics, 1989. **25**(5): p. 3327-3329.
63. Herzer, G., *Grain size dependence of coercivity and permeability in nanocrystalline ferromagnets.* Magnetics, IEEE Transactions on, 1990. **26**(5): p. 1397-1402.
64. Herzer, G., *The Random Anisotropy Model - A Critical Review and Update*, in *Properties and Applications of Nanocrystalline Alloys from Amorphous Precursors*. 2005, Springer, Dordrecht. p. 15-34.
65. Buschow, K.H.J. and F.R. Boer, *Physics of magnetism and magnetic materials*. 2003: Kluwer Academic/Plenum Publishers. New York, USA.
66. Suzuki, K., G. Herzer, and J. Cadogan, *The effect of coherent uniaxial anisotropies on the grain-size dependence of coercivity in nanocrystalline soft magnetic alloys.* Journal of Magnetism and Magnetic Materials, 1998. **177**: p. 949-950.
67. Suzuki, K., et al., *Local random magnetocrystalline and macroscopic induced anisotropies in magnetic nanostructures.* Journal of Non-Crystalline Solids, 2008. **354**(47-51): p. 5089-5092.
68. Yensen, T.D., *Magnetic and other properties of iron-silicon alloys, melted in vacuo.* University of Illinois. Engineering Experiment Station. Bulletin; no. 83, 1915.
69. Numakura, K.i., et al., *Magnetic and electric properties of iron-silicon alloys.* Science reports of the Research Institutes, Tohoku University. Ser. A, Physics, chemistry, 1972. **24**: p. 48-60.
70. Desai, P.D., *Thermodynamic properties of Iron and Silicon.* J. Phys. Chem. Ref. Data, 1986. **15**(3): p. 967-983.
71. Saito, A., T. Yamamoto, and H. Iwasaki, *Magnetization properties and domain structures of grain-oriented silicon steel sheets due to bending stress.* Magnetics, IEEE Transactions on, 2000. **36**(5): p. 3078-3080.

72. Fu, H., et al., *Improvement of magnetic properties of an Fe–6.5 wt.% Si alloy by directional solidification.* Materials Letters, 2011. **65**(9): p. 1416-1419.
73. Gonzalez, F. and Y. Houbaert, *A review of ordering phenomena in iron-silicon alloys.* Revista de Metalurgia, 2013. **49**(3): p. 178-199.
74. Chen, J., et al., *Influence of temperature on magnetic properties of silicon steel lamination.* AIP Advances, 2017. **7**(5): p. 056113.
75. Cui, S. and I.-H. Jung, *Critical reassessment of the Fe-Si system.* Calphad, 2017. **56**: p. 108-125.
76. Wang, S., et al., *Microstructure, mechanical and magnetic properties of melt extracted Fe-6.5 wt.%Si microwires.* Journal of Materials Processing Technology, 2017. **249**: p. 325-330.
77. Jayaraman, T.V., et al., *Investigation of structural and magnetic properties of rapidly-solidified iron-silicon alloys at ambient and elevated temperatures.* Journal of Alloys and Compounds, 2018. **741**: p. 409-419.
78. Carr, W.J. and R. Smoluchowski, *The Magnetostriction of Single Crystals of Iron-Silicon Alloys.* Physical Review, 1951. **83**(6): p. 1236-1243.
79. Hall, R.C., *Single Crystal Anisotropy and Magnetostriction Constants of Several Ferromagnetic Materials Including Alloys of NiFe, SiFe, AlFe, CoNi, and CoFe.* Journal of Applied Physics, 1959. **30**(6): p. 816-819.
80. Tatsumoto, E. and T. Okamoto, *Temperature Dependence of the Magnetostriction Constants in Iron and Silicon Iron.* Journal of the Physical Society of Japan, 1959. **14**(11): p. 1588-1594.
81. Ninomiya, H., et al., *Magnetostriction and applications of 6.5% Si steel sheet.* Journal of Applied Physics, 1991. **69**(8): p. 5358-5360.
82. Lei, Z., et al. *Study on magnetic properties and domain structures of Fe-(5, 6) wt% Si alloys prepared with high purity metallurgy*. in *Magnetics Conference (INTERMAG), 2015 IEEE*. 2015.
83. Tanner, L.E. and S.A. Kulin, *The effect of pressure on the α -> γ transformation in the iron-silicon system.* Acta Metallurgica, 1961. **9**(11): p. 1038-1040.
84. Zhang, J. and F. Guyot, *Experimental study of the bcc-fcc phase transformations in the Fe-rich system Fe-Si at high pressures.* Physics and Chemistry of Minerals, 1999. **26**(6): p. 419-424.
85. Lin, J., et al., *Phase Diagrams of Fe-Si Alloys under High Pressures.* 2001: p. 196-198.
86. Hirao, N., et al., *Equation of state of iron-silicon alloys to megabar pressure.* Physics and Chemistry of Minerals, 2004. **31**(6): p. 329-336.
87. Miyagi, L., et al., *In situ phase transformation and deformation of iron at high pressure and temperature.* Journal of Applied Physics, 2008. **104**(10): p. 103510.
88. Huang, E., W.A. Bassett, and P. Tao, *Study of Bcc-Hcp Iron Phase Transition by Synchrotron Radiation*, in *High-Pressure Research in Mineral Physics: A Volume in Honor of Syun-iti Akimoto*. 2013, American Geophysical Union. p. 165-172.
89. McGuire, C., et al., *Isothermal equation of state and phase stability of Fe5Si3 up to 96 GPa and 3000 K.* Journal of Geophysical Research: Solid Earth, 2017. **122**(6): p. 4328-4335.
90. Mehboob, N., *Hysteresis Properties of Soft Magnetic Materials*, PhD Thesis, *Faculty of Physics*. 2012, University of Vienna, Austria.

91. Scheriau, S., et al., *Magnetic characteristics of HPT deformed soft-magnetic materials.* Journal of Magnetism and Magnetic Materials, 2010. **322**(20): p. 2984-2988.
92. Okamoto, H.J., *Phase diagrams of binary iron alloys.* ASM International, 1993: p. 12-28.
93. Y. Yoshizawa, S.O., and K. Yamauchi, *New Fe-based soft magnetic alloys composed of ultrafine grain structure.* Journal of Applied Physics, 1988. **64**(10): p. 6044-6046.
94. Hono, K., et al., *The microstructure evolution of a Fe73.5Si13.5B9Nb3Cu1 nanocrystalline soft magnetic material.* Acta Metallurgica et Materialia, 1992. **40**(9): p. 2137-2147.
95. Hono, K., et al., *Microstructures of Fe73.5Si13.5B9Nb3Cu1 nanocrystalline soft magnetic material investigated by APFIM and HRTEM.* Surface Science, 1992. **266**(1): p. 385-390.
96. Hono, K., et al., *Atom probe study of the crystallization process of an Fe73.5Si13.5B9Nb3Cu1 amorphous alloy.* Applied Surface Science, 1993. **67**(1): p. 398-406.
97. Hono, K., et al., *Cu clustering and Si partitioning in the early crystallization stage of an Fe73.5Si13.5B9Nb3Cu1 amorphous alloy.* Acta Materialia, 1999. **47**(3): p. 997-1006.
98. Marin, P., M. Vazquez, and A. Hernando, *Magnetic hardening during the amorphous to nanocrystalline transformation in FeSiBCuNb alloys: theoretical considerations.* Journal of Magnetism and Magnetic Materials, 1999. **196-197**: p. 221-223.
99. Ramanujan, R.V. and Y.R. Zhang, *Quantitative transmission electron microscopy analysis of the nanocrystallization kinetics of soft magnetic alloys.* Physical Review B, 2006. **74**(22): p. 224408.
100. Zhang, Y.R. and R.V. Ramanujan, *Characterization of the effect of alloying additions on the crystallization of an amorphous Fe73.5Si13.5B9Nb3Cu1 alloy.* Intermetallics, 2006. **14**(6): p. 710-714.
101. Fujii, H., et al., *Nanocrystallization of Fe73.5Si13.5B9Nb3Cu1 soft-magnetic alloy from amorphous precursor in a magnetic field.* Journal of Materials Science, 2008. **43**(11): p. 3837-3847.
102. Chernenkov, Y.P., et al., *X-ray diffraction studies of the structure of nanocrystals in Fe73.5Si13.5B9Nb3Cu1 soft magnetic alloys before and after thermomechanical treatment.* Physics of the Solid State, 2010. **52**(3): p. 554-560.
103. Gheiratmand, T. and H.R.M. Hosseini, *Finemet nanocrystalline soft magnetic alloy: Investigation of glass forming ability, crystallization mechanism, production techniques, magnetic softness and the effect of replacing the main constituents by other elements.* Journal of Magnetism and Magnetic Materials, 2016. **408**: p. 177-192.
104. Hossain, E., et al., *Structural Properties and Crystallization Behavior of FINEMET Fe74Cu1. 5Nb2. 5Si12B10 Alloy Under Different Annealing Condition.* Dhaka University Journal of Science, 2016. **64**(1): p. 71-75.
105. Oshtrakh, M.I., et al., *Annealed FINEMET ribbons: Structure and magnetic anisotropy as revealed by the high velocity resolution Mössbauer spectroscopy.* Materials Chemistry and Physics, 2016. **180**: p. 66-74.

106. Wan, F., et al., *Development of FeSiBNbCu Nanocrystalline Soft Magnetic Alloys with High B s and Good Manufacturability.* Journal of Electronic Materials, 2016. **45**(10): p. 4913-4918.
107. Yousefi, M., K. Rahmani, and M.S. Amiri Kerahroodi, *Comparison of microstructure and magnetic properties of 3% Si-steel, amorphous and nanostructure Finemet.* Journal of Magnetism and Magnetic Materials, 2016. **420**: p. 204-209.
108. He, A., et al., *Dynamic magnetic characteristics and relaxation of Fe73.5Cu1Nb3Si15.5B7 nanocrystalline alloy under operating temperature and magnetizing frequency.* Journal of Magnetism and Magnetic Materials, 2017. **443**: p. 261-266.
109. Jha, R., et al., *Metastable Phase Diagram and Precipitation Kinetics of Magnetic Nanocrystals in FINEMET Alloys.* arXiv preprint arXiv:1709.08306, 2017.
110. Lekdim, A., L. Morel, and M.-A. Raulet, *Magnetic properties evolution of a high permeability nanocrystalline FeCuNbSiB during thermal ageing*.* Eur. Phys. J. Appl. Phys., 2017. **79**(2): p. 20601.
111. Boust, N., et al., *Modeling of hysteresis in Fe-Cu-Nb-Si-B cores with transverse K_u.* IEEE Transactions on Magnetics, 2017. **53**(11): p. 1-4.
112. Pan, H.L., et al., *Investigation of dipolar interaction in FINEMET ribbons through longitudinally driven magneto-impedance effect.* Journal of Magnetism and Magnetic Materials, 2017. **452**: p. 502-506.
113. Lashgari, H.R., et al., *Stress-relaxation heat treatment in FeSiBNb amorphous alloy: Thermal, microstructure, nanomechanical and magnetic texture measurements.* Journal of Magnetism and Magnetic Materials, 2018. **456**: p. 62-70.
114. Lekdim, A., L. Morel, and M.A. Raulet, *Effect of the remaining magnetization on the thermal ageing of high permeability nanocrystalline FeCuNbSiB alloys.* Journal of Magnetism and Magnetic Materials, 2018. **460**: p. 253-262.
115. Nutor, R.K., et al., *Transverse anisotropy field and lattice plane anisotropy of stress annealed Fe–Cu–Nb–Si–B ribbons.* Chinese Journal of Physics, 2018. **56**(1): p. 180-184.
116. Nutor, R.K., et al., *Structural anisotropy in FeCuNbSiB alloys: An in situ synchrotron XRD study.* Journal of Magnetism and Magnetic Materials, 2018. **454**: p. 51-56.
117. Varga, L.K. and J. Kovac, *Decomposing the permeability spectra of nanocrystalline finemet core.* AIP Advances, 2018. **8**(4): p. 047205.
118. Makino, A., et al., *New Excellent Soft Magnetic FeSiBPCu Nanocrystallized Alloys With High Bs of 1.9 T From Nanohetero-Amorphous Phase.* IEEE Transactions on Magnetics, 2009. **45**(10): p. 4302-4305.
119. Urata, A., et al., *Magnetic properties and structure of Fe83.3–85.8B7.0–4.5P9Cu0.7 nanocrystalline alloys.* Journal of Applied Physics, 2013. **113**(17): p. 17A311.
120. Lopatina, E., et al., *Surface crystallization and magnetic properties of Fe84.3Cu0.7Si4B8P3 soft magnetic ribbons.* Acta Materialia, 2015. **96**(0): p. 10-17.
121. Sato, K., et al., *Direct imaging of structural heterogeneity of the melt-spun Fe85.2Si2B8P4Cu0.8 alloy.* AIP Advances, 2015. **5**(6): p. 067166.
122. Wang, A., et al., *Crystallization Behavior of FeSiBPCu Nanocrystalline Soft-Magnetic Alloys with High Fe Content.* Science of Advanced Materials, 2015. **7**(12): p. 2721-2725.

123. Dan, Z., et al., *Effect of substitution of Cu by Au and Ag on nanocrystallization behavior of Fe83.3Si4B8P4Cu0.7 soft magnetic alloy.* Journal of Alloys and Compounds, 2016. **683**: p. 263-270.
124. Jafari, S., et al., *Atom probe analysis and magnetic properties of nanocrystalline Fe84.3Si4B8P3Cu0.7.* Journal of Alloys and Compounds, 2016. **674**: p. 136-144.
125. Wang, Y., et al., *Investigation on the crystallization mechanism difference between FINEMET® and NANOMET® type Fe-based soft magnetic amorphous alloys.* Journal of Applied Physics, 2016. **120**(14): p. 145102.
126. Gallagher, K.A., et al., *Distributed exchange interactions and temperature dependent magnetization in amorphous Fe 88−x Co x Zr 7 B 4 Cu 1 alloys.* Journal of Applied Physics, 1999. **85**(8): p. 5130-5132.
127. Shah, M., et al., *Thermal annealing induced modification of structural and soft magnetic properties of Fe33.8Co50.7Nb5B8.5P2 alloy.* Journal of Physics: Conference Series, 2016. **755**(1): p. 012035.
128. Fan, X., et al., *The effect of Ni addition on microstructure and soft magnetic properties of FeCoZrBCu nanocrystalline alloys.* AIP Advances, 2017. **7**(5): p. 056107.
129. Grabias, A., et al., *Mössbauer and magnetic studies of FeCoNiCuNbSiB nanocrystalline alloys.* Nukleonika, 2017. **62**(2): p. 79-84.
130. Herth, S., et al., *Diffusion and induced magnetic anisotropy in nanocrystalline Fe73.5Si13.5B9Nb3Cu1.* Philosophical Magazine Letters, 2004. **84**(8): p. 531-537.
131. Pozo López, G., et al., *Microstructure and soft magnetic properties of Finemet-type ribbons obtained by twin-roller melt-spinning.* Journal of Magnetism and Magnetic Materials, 2010. **322**(20): p. 3088-3093.
132. Clavaguera, N., et al., *Thermodynamic and kinetic factors controlling the formation of nanocrystalline FeCuNbSiB materials.* Nanostructured Materials, 1995. **6**(1): p. 453-456.
133. Yavari, A.R. and D. Negri, *Effect of concentration gradients on nanostructure development during primary crystallization of soft-magnetic iron-based amorphous alloys and its modelling.* Nanostructured Materials, 1997. **8**(8): p. 969-986.
134. Ayers, J.D., et al., *On the formation of nanocrystals in the soft magnetic alloy Fe73.5Nb3Cu1Si13.5B9.* Acta Materialia, 1998. **46**(6): p. 1861-1874.
135. Hono, K., D. Ping, and Y. Wu, *Microalloying effect on the microstructure and properties of nanocrystalline magnetic materials.* Materials Science, 2001. **22**(9): p. 35.
136. Blázquez, J., V. Franco, and A. Conde, *The influence of Cu addition on the crystallization and magnetic properties of FeCoNbB alloys.* Journal of Physics: Condensed Matter, 2002. **14**(45): p. 11717.
137. Hunziker, O., *Theory of plane front and dendritic growth in multicomponent alloys.* Acta Materialia, 2001. **49**(20): p. 4191-4203.
138. Shivaee, H., et al., *Effects of chemical composition on nanocrystallization kinetics, microstructure and magnetic properties of finemet-type amorphous alloys.* Metals and Materials International, 2013. **19**(4): p. 643-649.
139. Aronin, A., et al., *Structure and properties of nanocrystalline alloys prepared by high pressure torsion.* Reviews On Advanced Materials Science, 2010. **25**(1): p. 52-57.

140. Gavrilović, A., et al., *Phase transformations of Fe73.5Cu1Nb3Si15.5B7 amorphous alloy upon thermal treatment.* Journal of Alloys and Compounds, 2010. **504**(2): p. 462-467.
141. Han, Y., et al., *Improvement of magnetic properties, microstructure and magnetic structure of Fe73.5Cu1Nb3Si15.5B7 nanocrystalline alloys by two-step annealing process.* Journal of Materials Science: Materials in Electronics, 2015. **27**(4): p. 3736-3741.
142. Makino, A., *Nanocrystalline Soft Magnetic Fe-Si-B-P-Cu Alloys With High $ B $ of 1.8–1.9T Contributable to Energy Saving.* IEEE Transactions on Magnetics, 2012. **48**(4): p. 1331-1335.
143. Sharma, P., et al., *Competition driven nanocrystallization in high Bs and low coreloss Fe–Si–B–P–Cu soft magnetic alloys.* Scripta Materialia, 2015. **95**: p. 3-6.
144. Mushnikov, N.V., et al., *Magnetic properties and structure of nanocrystalline FINEMET alloys with various iron contents.* The Physics of Metals and Metallography, 2015. **116**(7): p. 663-670.
145. Jiang, D., et al., *Study on soft magnetic properties of Finemet-type nanocrystalline alloys with Mo substituting for Nb.* Physica Status Solidi (A), 2017. **214**(10): p. 1700074.
146. Wan, F., et al., *Surface crystallization and magnetic properties of FeCuSiBNbMo melt-spun nanocrystalline alloys.* Materials Research Bulletin, 2017. **96**: p. 275-280.
147. Xu, Y. and Z. Wang, *Mechanism of improved high-temperature magnetic softness for Co-contained Finemet alloy.* Magnetics, IEEE Transactions on, 2015. **51**(11): p. 1-4.
148. Kataev, V.A., et al., *Magnetic properties and induced anisotropy of nanocrystalline Fe72.5–x Ni x Cu1.1Nb1.9Mo1.5Si14.3B8.7 alloys.* Physics of Metals and Metallography, 2017. **118**(6): p. 558-563.
149. Han, Y., et al., *Improvement of magnetic properties for V-substituted Fe73.5Si13.5B9Cu1Nb3−xVx nanocrystalline alloys.* Journal of Materials Science: Materials in Electronics, 2017. **28**(14): p. 10555-10563.
150. Jia, Y., et al., *Effect of Ti on structure and soft magnetic properties of Si-rich Finemet-type nanocrystalline Fe73.5Cu1Nb3-xSi17.5B5Tix alloys.* Materials Research Bulletin, 2018. **106**: p. 296-300.
151. Pippan, R., et al., *Saturation of Fragmentation During Severe Plastic Deformation.* Annual Review of Materials Research, 2010. **40**(1): p. 319-343.
152. Oliver, W.C. and G.M. Pharr, *An improved technique for determining hardness and elastic modulus using load and displacement sensing indentation experiments.* Journal of Materials Research, 1992. **7**(6): p. 1564-1583.
153. Oliver, W.C. and G.M. Pharr, *Measurement of hardness and elastic modulus by instrumented indentation: Advances in understanding and refinements to methodology.* Journal of Materials Research, 2004. **19**(1): p. 3-20.
154. Panigrahi, A., *Mechanical properties and phase transformation of biocompatible nanostructured Ti-Nb alloys processed by severe plastic deformation*, PhD Thesis, *Faculty of Physics*. 2016: University of Vienna, Austria.
155. Ungár, T. and A. Borbély, *The effect of dislocation contrast on x-ray line broadening: A new approach to line profile analysis.* Applied Physics Letters, 1996. **69**(21): p. 3173-3175.

156. Jiang, H., M. Rühle, and E. Lavernia, *On the applicability of the x-ray diffraction line profile analysis in extracting grain size and microstrain in nanocrystalline materials.* Journal of Materials Research, 1999. **14**(2): p. 549-559.
157. Ungár, T., I. Alexandrov, and M. Zehetbauer, *Ultrafine-grained microstructures evolving during severe plastic deformation.* JOM, 2000. **52**(4): p. 34-36.
158. Kerber, M.S., E ; Zehetbauer, MJ, *Processing and evaluation of x-ray line profiles measured from nanostructured materials produced by severe plastic deformation.* Reviews On Advanced Materials Science, 2005. **10**(5): p. 427-433.
159. Ungár, T. and J. Gubicza, *Nanocrystalline materials studied by powder diffraction line profile analysis.* Zeitschrift für Kristallographie, 2007. **222**(3-4): p. 114-128.
160. Ribárik, G., T. Ungár, and J. Gubicza, *MWP-fit: a program for multiple whole-profile fitting of diffraction peak profiles by ab initio theoretical functions.* Journal of Applied Crystallography, 2001. **34**(5): p. 669-676.
161. Ungár, T., et al., *Crystallite size distribution and dislocation structure determined by diffraction profile analysis: principles and practical application to cubic and hexagonal crystals.* Journal of Applied Crystallography, 2001. **34**(3): p. 298-310.
162. Wilkens, M., *The determination of density and distribution of dislocations in deformed single crystals from broadened X-ray diffraction profiles.* J Physica status solidi, 1970. **2**(2): p. 359-370.
163. Ungár, T., et al., *The contrast factors of dislocations in cubic crystals: the dislocation model of strain anisotropy in practice.* Journal of Applied Crystallography, 1999. **32**(5): p. 992-1002.
164. Ribárik, G., J. Gubicza, and T. Ungár, *Correlation between strength and microstructure of ball-milled Al–Mg alloys determined by X-ray diffraction.* Materials Science and Engineering: A, 2004. **387**: p. 343-347.
165. Scardi, P. and M. Leoni, *Whole powder pattern modelling.* Acta Crystallographica Section A: Foundations of Crystallography, 2002. **58**(2): p. 190-200.
166. Watson, E.S. and M.J. O'neill, *Differential microcalorimeter*. 1966, Google Patents.
167. Gill, P., T.T. Moghadam, and B. Ranjbar, *Differential scanning calorimetry techniques: applications in biology and nanoscience.* Journal of Biomolecular Techniques: JBT, 2010. **21**(4): p. 167.
168. Cengeri, P., et al., *Strengthening during heat treatment of HPT processed copper and nickel.* Materials Science and Engineering: A, 2019. **742**: p. 124-131.
169. Horky, J., et al., *Exceptional Strengthening of Biodegradable Mg-Zn-Ca Alloys through High Pressure Torsion and Subsequent Heat Treatment.* Materials, 2019. **12**(15): p. 2460.
170. Ungar, T. and M.J. Zehetbauer, *Private communications, unpublished results.*
171. Kim, M.J. and W.F. Flanagan, *The effect of plastic deformation on the resistivity and hall effect of copper-palladium and gold-palladium alloys.* Acta Metallurgica, 1967. **15**(5): p. 735-745.
172. Jiles, D., *Introduction to magnetism and magnetic materials*. 2015: CRC press.
173. Courtney, T.H., *Mechanical behavior of materials*. 2005, Illinois: Waveland Press.
174. Ungar, T., *Determination of internal stresses, in: Multiscale phenomena in plasticity: from experiments to phenomenology*, ed. J. Lepinoux, et al. 2000: Springer NATO Science Series, p. 169